

Washington University in St. Louis

## Washington University Open Scholarship

---

Arts & Sciences Electronic Theses and  
Dissertations

Arts & Sciences

---

Winter 12-15-2018

# Tunable Electronic and Optical Properties of Low-Dimensional Materials

Shiyuan Gao

*Washington University in St. Louis*

Follow this and additional works at: [https://openscholarship.wustl.edu/art\\_sci\\_etds](https://openscholarship.wustl.edu/art_sci_etds)



Part of the [Materials Science and Engineering Commons](#), [Mechanics of Materials Commons](#), [Nanoscience and Nanotechnology Commons](#), and the [Physics Commons](#)

---

### Recommended Citation

Gao, Shiyuan, "Tunable Electronic and Optical Properties of Low-Dimensional Materials" (2018). *Arts & Sciences Electronic Theses and Dissertations*. 1723.  
[https://openscholarship.wustl.edu/art\\_sci\\_etds/1723](https://openscholarship.wustl.edu/art_sci_etds/1723)

This Dissertation is brought to you for free and open access by the Arts & Sciences at Washington University Open Scholarship. It has been accepted for inclusion in Arts & Sciences Electronic Theses and Dissertations by an authorized administrator of Washington University Open Scholarship. For more information, please contact [digital@wumail.wustl.edu](mailto:digital@wumail.wustl.edu).

WASHINGTON UNIVERSITY IN ST. LOUIS

Department of Physics

Dissertation Examination Committee:

Li Yang, Chair

Erik Henriksen

Rohan Mishra

Alexander Seidel

Zohar Zussinov

Tunable Electronic and Optical Properties of Low-Dimensional Materials

by

Shiyuan Gao

A dissertation presented to  
The Graduate School  
of Washington University in  
partial fulfillment of the  
requirements for the degree  
of Doctor of Philosophy

December 2018  
St. Louis, Missouri

© 2018, Shiyuan Gao

# Table of Contents

|   |    |
|---|----|
| Acknowledgments.....  | iv |
| Abstract of the Dissertation .....  | vi |
| Chapter 1: Introduction .....   | 1  |
| Chapter 2: Theoretical Background .....   | 7  |
| 2.1 Density Functional Theory.....  | 8  |
| 2.1.1 Hohenberg-Kohn Theorems and Kohn-Sham Equation .....  | 8  |
| 2.1.2 Plane-Wave Pseudopotential Method .....   | 10 |
| 2.2 Quasiparticle and GW Approximation.....   | 11 |
| 2.2.1 Theoretical Formalism .....   | 11 |
| 2.2.2 Practical Implementation .....  | 13 |
| 2.3 Exciton and Bethe-Salpeter Equation .....   | 15 |
| 2.3.1 Excitons in Bulk and Two Dimensions.....  | 15 |
| 2.3.2 Bethe-Salpeter Equation .....   | 16 |
| 2.3.3 Optical Property .....  | 17 |
| Chapter 3: Renormalization of the Quasiparticle Band Gap in Doped Two-Dimensional<br>Materials .....                  | 20 |
| 3.1 Introduction .....  | 20 |
| 3.2 Computational Details and Intrinsic Properties .....  | 22 |
| 3.3 GW Self-Energy and Effective Mass Model: h-BN and MoS <sub>2</sub> .....  | 24 |
| 3.4 Band Gap Renormalization of Monolayer Black Phosphorus .....  | 33 |
| 3.5 Band Gap Renormalization of ReSe <sub>2</sub> on Graphene .....   | 38 |
| 3.6 Summary .....   | 41 |
| Chapter 4: Dynamical Excitonic Effects in Doped Two-Dimensional Materials.....  | 42 |
| 4.1 Introduction .....  | 42 |
| 4.2 Dynamical Effects in Bethe-Salpeter Equation.....   | 44 |
| 4.3 Calculation Details and Comparison of Different Approximations.....   | 49 |
| 4.4 Excitonic Spectrum and Absorption Lineshape .....   | 55 |
| Chapter 5: Interlayer Coupling and Gate-Tunable Excitons in Transition Metal Dichalcogenide<br>Heterostructures ..... | 60 |
| 5.1 Introduction .....  | 60 |

|   |   |    |
|---|---|----|
| 5.2   | Interlayer Coupling at the Single-Particle Level..... | 61 |
| 5.3   | Interlayer Coupling at the Excitonic Level .....      | 64 |
| 5.4   | Tunable Excitonic Properties .....                    | 68 |
| Chapter 6: Edge-insensitive Magnetism and Half Metallicity in Graphene Nanoribbons .....                                  |   | 73 |
| 6.1   | Introduction .....                                    | 73 |
| 6.2   | Magnetism in Doped Graphene Nanoribbons .....         | 74 |
| 6.3   | Stoner Model of Iterant Magnetism .....               | 82 |
| Chapter 7: Half-Metallicity with Strong Magnetic Anisotropy in Doped One-Dimensional Helical Tellurium Atomic Chain ..... |   | 87 |
| 7.1   | Introduction .....                                    | 87 |
| 7.2   | Magnetism in Single Tellurium Chain .....             | 89 |
| 7.3   | Strong Magnetic Anisotropy .....                      | 94 |
| 7.4   | Discussion .....                                      | 96 |
| References .....  |   | 99 |

# Acknowledgments

I would first like to express my deep gratitude towards my advisor Prof. Li Yang. As I was going through my PhD and trying to learn to be a good researcher, he was giving me tremendous freedom and encouragement to let me pursue my own ideas, while correcting me when I had wandered off-track. He not only helped me grow more independent but also cared about my future. I could not have come to this place without his guidance and support.

I would like to give thanks to the members of my committee, Prof. Zohar Zussinov, Alexander Seidel, Erik Henriksen and Rohan Mishra for their time and support. I would also like to thank my collaborator Dr. Catalin Spataru at Sandia National Labs who had been really kind to me and offered me great support both in and outside of research, and Prof. Giovanni Vignale at University of Missouri, whose insight and appreciation of the beauty of physics has been truly inspiring for me. Meanwhile, I have also benefitted a lot from the great classes taught by, and discussions I had with Prof. Carl Bender, Zohar Zussinov, and Willem Dickhoff.

I would also like to thank my past and present group members, Yufeng Liang, Ryan Soklaski, Vy Tran, Ruixiang Fei, Wenshen Song, Xiaobo Lu, Linghan Zhu, Hongxia Zhong, Jahyun Koo, Yuanyuan Pan and Jizhang Wang for their friendship and support. It's been a pleasure working with you.

I owe a deep thank-you to my girlfriend Chunyu Song for her company and support during my PhD. She had made me a better person in so many ways.

Finally, I would like to thank my parents, who have in large part shaped who I am today. They both have what I believe to be the greatest asset a normal person can have – the combination a great sense of responsibility and an appreciation of beauty towards everyday life, nature and

human knowledge. They are also very supportive for letting me make my own decision along the course of my life. I feel truly lucky to be their son.

Shiyuan Gao

*Washington University in St. Louis*

*Dec 2018*

## ABSTRACT OF THE DISSERTATION

Tunable Electronic and Optical Properties of Low-Dimensional Materials

by

Shiyuan Gao

Doctor of Philosophy in Physics

Washington University in St. Louis, 2018

Professor Li Yang, Chair

Two-dimensional (2D) materials with single or a few atomic layers, such as graphene, hexagonal boron nitride (h-BN) and transition metal dichalcogenides (TMDCs), and the heterostructures or one-dimensional (1D) nanostructures they form, have attracted much attention recently as unique platforms for studying many condensed-matter phenomena and holds great potentials for nanoelectronics and optoelectronic applications. Apart from their unique intrinsic properties which has been intensively studied for over a decade by now, they also allow external control of many degrees of freedom, such as electrical gating, doping and layer stacking. In this thesis, I present a theoretical study of the electronic and optical properties of many different 2D materials and nanostructures using first-principles density functional theory and many-body perturbation theory. I will show what we learn from these theoretical calculations about the relation between the partially extended, partially confined structure and the tunability of their electronic and optical properties with free-carrier doping and electrical gating.

First, we investigate the effect of free-carrier doping on the quasiparticle and exciton properties of 2D material. On one hand, we discuss the origin of the doping-induced band gap renormalization in 2D materials and demonstrate the simplifications that can be made to the



theory to allow more efficient calculation. On the other hand, using MoS<sub>2</sub> as an example, we study the effect of dynamical screening on the electron-hole interaction and excitonic properties in doped 2D material using the Bethe-Salpeter Equation. Combining them, we show that the quasiparticle band gap of 2D material drops as a non-linear function of doping density by several hundred meV due to the free-carrier screening, but this is offset by the drop in the exciton binding energy and makes the exciton energy remain nearly constant.

Then, we switch gear to study the effect of electrical gating on excitons in bilayer TMDC heterostructures. We reveal the important role of interlayer coupling in deciding the band alignment and excitonic properties. We show that due to the interlayer coupling of valence states, the excitons are superpositions of intralayer and interlayer electron-hole pairs which can be described by a simple tight-binding model. As a result, their dipole oscillator strength and radiative lifetime can be tuned by over an order of magnitude with a practical external gate field of a few V/nm.

Finally, we study the effect of quantum confinement on the formation of magnetism in confined nanostructures. In two one-dimensional structures, graphene nanoribbon and tellurium chain, we find doped free-carriers can have half-metallic ferromagnetic ground state due to the Stoner mechanism. This comes from the quantum-confinement of the electronic state which enhances the density of state and Stoner parameter at the same time. For graphene nanoribbons, we find magnetism in general edge types with large spin polarization energy up to 17 meV/carrier. It can bypass the requirement of specific zigzag edge in previous proposals of graphene nanoribbon magnetism. For tellurium chain, we find magnetic ground state with a significant 6 meV/carrier spin-polarization energy. Due to the strong spin-orbit interaction of tellurium and its unique helical chain structure with chirality, the spins of the magnetic carriers are pinned along a

specific direction with an enhanced magnetic anisotropy energy that is larger than the spin-polarization energy, making it of broad interest for spintronics applications.

# **Chapter 1: Introduction**

Until very recently, almost all naturally occurring and man-made crystalline materials are bulky from a microscopic view, extending in all three spatial directions by thousands to millions of unit cells. This was changed by the discovery of single layer two-dimensional (2D) materials, starting with the isolation of graphene by Novoselov and Geim in 2004 [1] and followed by other materials such as hexagonal boron nitride (h-BN), transition metal dichalcogenide (TMDC) and black phosphorus (BP) [2-4]. These 2D materials have promising applications in many different areas including electronics, optoelectronics, photonics and sensing technologies [5-8]. For example, the TMDCs are promising for spintronics and valleytronics applications due to their valley selective optical transition and spin-orbit splitting [9, 10]. In addition, many phenomena central to modern condensed matter physics, such as strong correlation and topological physics, can be studied with these materials. For example, graphene with its massless Dirac dispersion has unconventional Landau levels and could become a quantum spin Hall insulator with spin-orbit coupling [11, 12]. More recently, 2D materials with 2D Ising magnetism [13], Heisenberg magnetism [14], itinerant magnetism [15], and charge-density waves [16, 17] have been discovered, which has greatly expanded our view of various electronic instabilities and associated phase transitions in 2D.

Apart from the intrinsic properties, these 2D materials and their derivative nanostructures are also unique in that they allow more degrees of freedom to be controlled externally, with for example electrical gating, doping, layer stacking and twisting [18, 19]. With a top and a bottom gate, the doping density and vertical electric field can be tuned independently and continuously in experiments. With the freedom to stack different layers of 2D materials together, unlimited

number of different composite materials can be made. And with an interlayer twist, a Moiré superlattice at a much larger length scale can be created on top of the host material. Many interesting physical systems can be realized by controlling these degrees of freedom. For example, exciton condensate is expected to occur in a gated heterostructure due to the strong excitonic effect in 2D materials [20, 21]. But perhaps the most striking example is the recent discovery of superconductivity and Mott insulating phase in magic-angle twisted bilayer graphene, which opens a new route for studying the long-standing puzzle of unconventional superconductivity [22, 23]. On the application side, these degrees of freedom allow the engineering and control of many material properties such as the electronic and optical band gap. Despite many research efforts into this direction, much more have remain unexplored.

In this regard, it is a huge endeavor, up to condensed matter physicist and material scientists, to understand the relation between the intrinsic atomic structure, tunable external environment and the properties of these low-dimensional materials. Many research efforts have been made but there are even more open questions remaining.

For example, a topic that will be discussed in this thesis is the quasiparticle band gap of 2D materials. It is known that for a given 2D material, the band gap usually increases dramatically as the number of layers decrease [24, 25], which come from a combination of the quantum confinement of the electronic state and the reduced dielectric screening due to the surrounding vacuum [26]. The dielectric screening in 2D material is particularly interesting: the dielectric function  $\epsilon(q)$  goes to 1 in the long wavelength limit ( $q \rightarrow 0$ ) but quickly approach a bulk value that is much larger when  $q$  becomes comparable to the inverse of the layer thickness [27]. This behavior lead to false convergence of many calculations before this is finally understood and resolved [28-31]. However, despite its common occurrence in experiments, less is known about

how the band gap would change with respect to the introduction of doping, which in itself also changes the dielectric screening of the system in a way that is completely different from bulk materials. This is one of the topics that will be addressed in chapter 3 and 4 of this thesis.

Overall, in this thesis, we theoretically investigate the change in the electronic and optical properties of low-dimensional materials in response to the doping and gating, using the tool of first-principles calculations. First-principles, or *ab initio*, calculations are theoretical calculations that use only the atomic structure as input and predicts material properties based only on fundamental laws of quantum mechanics, without any free parameters. Aided by the advancement in theoretical formalism, computer algorithms and modern computer hardware, these calculations can be performed at high accuracy for materials and serve as a bridge that connects simple physical concepts with experimentally relevant observables.

Because finding the state of electrons in a solid is a complicated quantum many-body problem, any realistic calculations must rely on some level of approximations. Here we use density functional theory (DFT) as a mean-field starting point and use many-body perturbation theory for the calculation of excited state properties. DFT is a powerful method that has been used all cross physics, chemistry and material science. It can accurately predict the ground state properties, such as total energy, lattice structure, electron density and the shape of the band structure of most materials. However, to get an accurate description of the excited state properties such as the quasiparticle band gap, we need to go one step further and use the GW approximation, which includes the non-local electron exchange and correlation effects. Finally, we use the Bethe-Salpeter Equation (BSE) to include the electron-hole correlation effect and study excitons – pairs of electron and hole bounded together by their mutual Coulomb

interaction. The excitonic effect is particularly strong in 2D materials due to reduced screening and dominates their optical properties.

This thesis is organized as follows. In Chapter 2, we go through the theoretical background and discuss the theories and computational methods behind these works. After that, we first study the effects of free-carrier doping on the quasiparticle and exciton properties of 2D materials in chapter 3 and 4. Chapter 3 focuses on the quasiparticle gap side of the story and deals with the GW approximation. We distill the dominant contribution in doping-induced band gap renormalization of 2D materials and discuss simplifications to the theoretical formalism that make use of the low-density limit to make the calculations more efficient. The simplified theoretical formalism is applied to different 2D materials, including one with in-plane anisotropy (black phosphorus) and one bilayer system with incommensurate lattice constant ( $\text{ReSe}_2 + \text{graphene}$ ). Chapter 4 focuses on the exciton side of the story and deals with the BSE. We discuss the breakdown of the commonly used static approximation in BSE, the way to include the dynamical effects and why the renormalization of band gap and exciton binding energy tends to cancel each other. We also discuss how the absorption spectrum and exciton states evolve upon increasing doping.

In chapter 5, we switch gear to study the effect of electrical gating on excitons in a bilayer TMDC heterostructure. It is commonly perceived that these bilayer heterostructure have “type II” band alignment, meaning the valence band maximum and conduction band minimum belong to different layers. Therefore, the lowest exciton state is seen as an “interlayer” state, whereas the “intralayer” states locate in higher energies. From the result of first-principle GW+BSE calculations with different gate field, we extract a simple tight-binding model and show that despite this common interpretation, each of the eigenstates are actually superpositions of

intralayer and interlayer electron-hole pairs and are continuously tunable by external electric field. This leads to anti-crossing behavior in their energy and give them tunable optical oscillator strength and radiative lifetime.

Then in chapter 6 and 7, we switch topic again to study magnetism in one-dimensional nanostructures. Although magnetism usually originates from transition-metal atoms with partially-filled d or f orbital, we find that these localized orbitals may be not be necessary in a doped narrow 1D nanostructure, due to the divergent van Hove singularity in the density of state and the confinement of the electronic wavefunction. Specifically, from DFT calculation, we find that the electronic ground state can be ferromagnetic for doped graphene nanoribbon and tellurium chain due to the Stoner mechanism. Chapter 6 deals with graphene nanoribbon, gives the theoretical explanation of this mechanism and show that it is insensitive to the specific edge structures, which often strongly affect the property of graphene nanoribbon. Chapter 7 deals with tellurium chain and discusses the implication of this magnetic ground state when combined with its unique chiral structure and strong spin-orbit coupling.





## Chapter 2: Theoretical Background

When we are interested in calculating the properties of a solid, the general problem we are facing is the motion of electrons and nuclei described by the following Hamiltonian:

$$\hat{H} = -\frac{\hbar^2}{2m_e} \sum_i \nabla_i^2 - \sum_{i,l} \frac{Z_l e^2}{|r_i - R_l|} + \frac{1}{2} \sum_{i \neq j} \frac{e^2}{|r_i - r_j|} - \sum_I \frac{\hbar^2}{2M_I} \nabla_I^2 + \frac{1}{2} \sum_{I \neq J} \frac{Z_I Z_J e^2}{|R_I - R_J|} \quad (2.1)$$

where  $r_i$  and  $R_I$  are the position of electrons and nuclei, respectively. Usually one can take advantage of the fact that the nuclei mass  $M_I$  is much larger than the electron mass  $m_e$  and make the adiabatic (Born-Oppenheimer) approximation to separate the electron's motion from that of nuclei's and treat the nuclei's motion classically. This keeps the first three terms in Eq. (2.1) and turns the Hamiltonian into that of  $N$  interacting electrons moving in the potential of the nuclei.

Trying to solve this problem exactly in general is hopeless, not only because  $N$  is usually a very large on the order of Avogadro number for a solid, but more importantly because the number of possible eigenstates as given by the dimension of the Hilbert space grows exponentially with  $N$ .

Trying to solve this problem of interacting electrons is one of the central topics of condensed matter physics. Within the numerous approaches [32], we will focus on density functional theory (DFT) and the many-body Green's function method. They are the state-of-the-art tools that have achieved excellent accuracy in the study of the ground and excited state properties, such as structure, ground state energy, band gap and exciton, of weakly-correlated materials [33]. The rest of this chapter will be a brief introduction of these methods, from theoretical formulation to practical implementations.

## 2.1 Density Functional Theory

### 2.1.1 Hohenberg-Kohn Theorems and Kohn-Sham Equation

The idea behind DFT originates from the two Hohenberg-Kohn Theorems published in 1964 [34]. They connect the ground-state properties of an  $N$ -electron system, which in principle need  $3N$  spatial coordinates to describe, to the electron density, which only need 3 spatial coordinates to describe.

Consider the problem of  $N$  interacting electrons moving in a large box in an arbitrary external potential  $v_{ext}(\mathbf{r})$ . Assuming the ground state is non-degenerate, then it is obvious that the ground-state electron density  $n(\mathbf{r})$  is uniquely determined by the potential  $v_{ext}(\mathbf{r})$ . The first Hohenberg-Kohn Theorem states that the converse is also true, i.e. one density  $n(\mathbf{r})$  can correspond to only one unique  $v_{ext}(\mathbf{r})$ . As a consequence, all ground-state properties, including the many-body wavefunction, can be given as universal functionals of  $n(\mathbf{r})$ , not explicitly depending on  $v_{ext}(\mathbf{r})$ . This inspired Hohenberg and Kohn to write the energy functional as follows:

$$E_{v,N}[n] = \int v_{ext}(\mathbf{r})n(\mathbf{r})d\mathbf{r} + F[n] \quad (2.2)$$

where  $F[n]$  is the kinetic and interaction energy functional. The second Hohenberg-Kohn Theorem states that for a given potential  $v_{ext}$  and total electron number  $N$ , the functional  $E_{v,N}[n]$  assumes minimum value when  $n$  is the actual ground-state density. This enables the calculation of ground-state energy by varying the electron density  $n$  instead of the  $N$ -electron wavefunction, provided that we have a good enough approximation of the functional  $F[n]$ .

There are many ways to obtain an approximate form of the functional  $F[n]$ , and the most popular one is the Kohn-Sham formalism originally published in 1965 [35]. It begins with further separating the electron kinetic energy and Hartree potential energy from Eq. (2.2):

$$E_{v,N}[n] = T[n] + \int v_{ext}(\mathbf{r})n(\mathbf{r})d\mathbf{r} + E_H[n] + E_{xc}[n] \quad (2.3)$$

where  $E_{xc}[n] \equiv F[n] - T[n] - E_H[n]$  is called the exchange-correlation functional. The variational stationary point  $\frac{\delta E_{v,N}[n]}{\delta n} = 0$ , subjected to the condition  $\int \delta n(\mathbf{r})d\mathbf{r} = 0$ , corresponds to the equation

$$\frac{\delta T[n]}{\delta n(\mathbf{r})} + v_{ext}(\mathbf{r}) + \int \frac{n(\mathbf{r}')}{|\mathbf{r}-\mathbf{r}'|} d\mathbf{r}' + \frac{\delta E_{xc}[n]}{\delta n(\mathbf{r})} = 0 \quad (2.4)$$

Kohn and Sham noticed that Eq. (2.4) yields the same density as an auxiliary non-interacting electron system with the following single-particle Schrödinger Equation:

$$\left[ -\frac{\hbar^2 \nabla^2}{2m_e} + v_{ext}(\mathbf{r}) + \int \frac{n(\mathbf{r}')}{|\mathbf{r}-\mathbf{r}'|} d\mathbf{r}' + v_{xc}(\mathbf{r}; [n]) \right] \psi_i(\mathbf{r}) = \varepsilon_i \psi_i(\mathbf{r}) \quad (2.5)$$

with the charge density given by  $n(\mathbf{r}) = \sum_i f_i |\psi_i(\mathbf{r})|^2$ , where  $v_{xc}(\mathbf{r}; [n]) \equiv \frac{\delta E_{xc}[n]}{\delta n(\mathbf{r})}$  and  $f_i$  denotes the occupation numbers of the states. This formalism reduces the N-electron problem into the problem of solving the single-particle Kohn-Sham Equation (2.5) self-consistently until the charge density  $n(\mathbf{r})$  converges. It has become the foundation of most of the modern DFT calculations [36].

Despite a lack of rigorous physical meaning, the eigenvalues and eigenfunctions of the Kohn-Sham Equation are widely used to describe realistic systems such as the single-particle band

structure of solids with great success. Particularly, the shape of the band structure of a solid given by Kohn-Sham DFT is quite often an accurate representation of the real one.

The exchange-correlation potential  $v_{xc}$  in the Kohn-Sham Equation is of course still unknown in general. In fact, the existence of an efficient algorithm to determine the universal functional in DFT would imply P=NP [37], which is believed to be highly unlikely. However, very simple approximations to  $v_{xc}$  can already lead to very accurate *ab initio* description of realistic systems. The simplest one is the local density approximation (LDA), which replaces  $E_{xc}[n]$  with that of homogeneous electron liquid. One can go a step further to the generalized gradient approximation (GGA), which includes the first-order gradient expansion around the homogeneous density, without much increase in the computational cost. Despite their simplicity, LDA and GGA are the most widely used exchange-correlation functionals of DFT, and they give accurate description of the ground state properties of solids such as lattice constant and bulk modulus within a few percent of the experimental value. There are many other functionals that go further in accuracy with the inclusion of more terms, at the expense of increased computational cost, forming the so-called “Jacob’s ladder” [38].

### **2.1.2 Plane-Wave Pseudopotential Method**

There are many different implementations of *ab initio* Kohn-Sham DFT into the calculation of real molecules and solids made of different elements. One important element is the choice of the basis set. One common choice is the plane-wave basis, which has a simple, natural definition and comes in hand with the extended Bloch states in crystals.

However, for heavy elements, the core electrons are highly localized in a small region near the atomic nucleus and play very little role in the chemical bonding between solids. To make matters

worse, the wavefunctions of both the valence and core electrons are very rapidly varying near the core region due to the orthogonality requirement of the wavefunctions, which requires very high energy components to be captured in a plane-wave basis. Therefore, instead of describing all electrons simultaneously, many implementations of DFT leaves out the core electrons and use pseudopotentials to reproduce the effects of core electrons to the valence electrons, keeping the behavior of valence electrons almost identical to the real atom when it is outside a small core radius. This plane-wave pseudopotential method is implemented in many popular *ab initio* DFT packages such as QuantumEspresso [39] and VASP [40], and it will be the primary method used in this thesis.

## 2.2 Quasiparticle and GW Approximation

### 2.2.1 Theoretical Formalism

In condensed matter physics, the concept of elementary excitation is used to describe the excited states of a quantum many-body system. Elementary excitations are emergent phenomena of a system such that it behaves like weakly interacting particles. For example, the electron/hole quasiparticle are excitations that behave like free electron/hole with the same elementary charge, but with their effective mass modified by the interaction. In this picture, the effect of the interactions of an electron with the cloud of surrounding medium (other electrons and lattice vibrations, etc.) is described by the electron's self-energy  $\Sigma$  [41]. Other examples of elementary excitations include plasmon, phonon, magnon and exciton.

Although DFT is in principle an exact method for studying the ground state of a quantum many-body system, it cannot provide accurate information about the excited state properties, including the various electronic elementary excitations. One famous example is the “band gap problem” of DFT, i.e. DFT consistently underestimates the quasiparticle band gap of materials, predicting

values that are of order  $\sim eV$  below the experimental value, and even falsely predict some narrow gap semiconductors such as germanium to be metal. The many-body perturbation theory is a way to go beyond DFT and study the excited state properties of materials.

The idea behind many-body perturbation theory is to start from the independent-particle problem and add the Coulomb interaction as a perturbation. In 1965, Hedin formulated a closed set of equations that effectively expands the self-energy and Green's function in terms of the screened Coulomb interaction [42]. To first order, it is equivalent to writing the polarizability within the random phase approximation (RPA):

$$\chi^{RPA} = \frac{\chi_0}{1 - v_c \chi_0} \quad (2.6)$$

where  $\chi_0$  is the non-interacting electron polarizability and  $v_c$  is the Coulomb interaction. It also writes the quasiparticle self-energy in terms of the product between the Green's function and the screened Coulomb interaction:

$$\Sigma = iGW \quad (2.7)$$

which is where the name "GW approximation" comes from. Finally, the Dyson's Equation  $G = G_0 + G_0 \Sigma G$  relates the interacting Green's function to the self-energy. Usually, the calculation stops at "G<sub>0</sub>W<sub>0</sub>" level, where both G and W in Eq. (2.7) are calculated from the non-interacting value. Partial or full self-consistency, in either G or W, and in either the eigenvalue or the full wavefunction, can be made. However, no consistent improvement over the G<sub>0</sub>W<sub>0</sub> is obtained with these self-consistent methods.

Here the screened Coulomb interaction  $W$  and the polarizability  $\chi^{RPA}$  is related by the dielectric function:

$$\epsilon^{RPA} = \frac{1}{1+v_c\chi^{RPA}} = 1 - v_c\chi_0 \quad (2.8)$$

$$W = [\epsilon^{RPA}]^{-1}v_c \quad (2.9)$$

Physically, the dielectric function describes the screening of the medium to a change in the potential:  $V_{sc}(\mathbf{r}, \omega) = \int d\mathbf{r}' \epsilon^{-1}(\mathbf{r}, \mathbf{r}', \omega) V_{ext}(\mathbf{r}', \omega)$ . In a periodic lattice,  $\epsilon$  is usually written as the Fourier transformed form  $\epsilon_{\mathbf{G}\mathbf{G}'}(\mathbf{q}, \omega)$ , where  $\mathbf{q}$  is a vector in the first Brillouin zone and  $\mathbf{G}, \mathbf{G}'$  are the reciprocal lattice vectors.  $\epsilon_{\mathbf{0}\mathbf{0}}^{-1}(\mathbf{q}, \omega)$  contains the macroscopic part of the dielectric screening, and  $\epsilon_{\mathbf{0}\mathbf{0}}^{-1}(\mathbf{0}, 0)$  corresponds to the dielectric constant of bulk materials.

### 2.2.2 Practical Implementation

In a practical calculation with the GW approximation in a periodic lattice, the non-interacting electrons described by the Kohn-Sham Equation is usually used as the starting point. First, the non-interacting polarizability  $\chi_{\mathbf{G}\mathbf{G}'}(\mathbf{q}, \omega)$  and the inverse dielectric function  $\epsilon_{\mathbf{G}\mathbf{G}'}^{-1}(\mathbf{q}, \omega)$  is calculated from the Kohn-Sham eigenvalues and eigenstates. They are calculated on a q-point grid in the Brillouin zone with a cutoff energy in the G-vectors. The calculation of  $\chi_{\mathbf{G}\mathbf{G}'}(\mathbf{q}, \omega)$  also involves a summation over all empty bands, which in practice requires a cutoff. The q-grid density and the cutoffs in G-vector and number of bands all needs to be converged numerically. The frequency-dependence of  $\chi_{\mathbf{G}\mathbf{G}'}(\mathbf{q}, \omega)$  and  $\epsilon_{\mathbf{G}\mathbf{G}'}^{-1}(\mathbf{q}, \omega)$  are usually not calculated explicitly but approximated with a plasmon-pole model [43].

Then, for each k-point and band that we are interested in, the quasiparticle self-energy is calculated, and the Dyson's Equation is solved. Usually, the Dyson's Equation is solved in the first-order approximation, where the quasiparticle is assumed to have a well-localized peak and

the wavefunction is the same as the Kohn-Sham wavefunction. Then only the quasiparticle energy is updated, according to the quasiparticle equation

$$\varepsilon_{nk} = \varepsilon_{nk}^{DFT} + \langle \psi_{nk}^{DFT} | \Sigma_{nk}(\varepsilon_{nk}) - v_{xc} | \psi_{nk}^{DFT} \rangle \quad (2.10)$$

where  $v_{xc}$  is the exchange-correlation contribution from DFT. The evaluation of the self-energy also involves a summation over the all empty bands, which also needs to be converged numerically.

The GW approximation is very successful in describing the band gap of materials, including bulk and the recently-emerging 2D materials. Figure 2.1 shows as an example the DFT and GW band structure of monolayer MoS<sub>2</sub>. As we can see, the GW approximation adds nearly 1eV to the band gap.

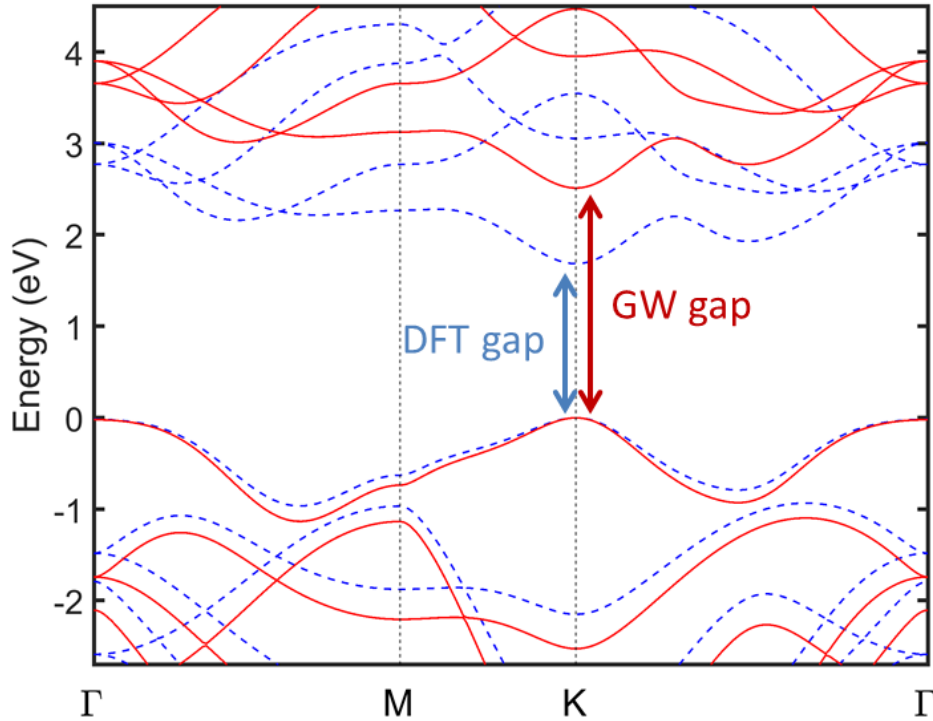


**Figure 2.1** The DFT (blue dashed line) and GW (red solid line) band structure of monolayer MoS<sub>2</sub>.



There are many computational packages development for solving the GW approximation, and the Bethe-Salpeter Equation that will be discussed in the next Section. In this thesis, the calculation will be conducted with the BerkeleyGW package [44], which is based on plane-wave pseudopotential DFT method.

## **2.3 Exciton and Bethe-Salpeter Equation**

### **2.3.1 Excitons in Bulk and Two Dimensions**

Exciton is a composite quasiparticle made of a quasi-electron and a quasi-hole. The electron and hole are bounded together with their mutual Coulomb attraction. Because they are charge-neutral, they can be created from an optical excitation, or recombine to release a photon. The exciton phenomenon and more generally speaking, the electron-hole (e-h) correlation, are therefore important to the understanding of the optical properties of solid.

Excitons in bulk materials are categorized into different types. The Wannier excitons are the ones with a weakly bounded e-h pair, in which their motion can be described macroscopically as free particles with an effective mass bounded by their Coulomb potential. The hydrogen model with a screened Coulomb potential is often used to describe this kind of exciton, and different energy levels in analogous with the 1s, 2s, 2p ... states of the hydrogen can be assigned to them. In a bulk crystal, their binding energy is usually on the order of tens of meV. The Frenkel excitons are the ones that are highly localized on a few atoms, which are usually more strongly bound with binding energy of 0.1-1 eV, and their properties are more specific to the local atomic structure. Charge-transfer excitons are also localized excitons, but with electron and hole occupying different atoms are forming a strong dipole.

In low-dimensional structures, the picture of excitons is changed. For example, in a single-layer 2D material like MoS<sub>2</sub>, the exciton is extended like a Wannier exciton in the in-plane direction but strongly confined like the Frenkel exciton in the off-plane direction. In a bilayer heterostructure, interlayer exciton with electron and hole in opposite layers can be formed (which is our subject of study in Chapter 5). In this case, the exciton looks like a Wannier exciton in the in-plane direction but a charge-transfer exciton in the off-plane direction. Even considering only the in-plane direction, the screening to the Coulomb potential in a 2D material is much weaker, leading to Wannier excitons of binding energy of hundreds of meV. The shape of the screened Coulomb potential also strongly deviates from that of the bare Coulomb potential, which leads to a completely different series of exciton levels.

### 2.3.2 Bethe-Salpeter Equation

From the point of view of many-body perturbation theory, the e-h correlation can be described by the Bethe-Salpeter Equation (BSE). Formally, it is given by a Dyson equation for the two-particle Green's function:

$$L(1,2,3,4) = L_0(1,2,3,4) + L_0(1,2,5,6)K(5,6,7,8)L(7,8,3,4) \quad (2.11)$$

Where  $L$  and  $L_0$  are the interacting and non-interacting two-particle Green's function, and the interaction kernel is  $K(5,6,7,8) = \delta(5,6)\delta(7,8)v_c(5,7) - \delta(5,7)\delta(6,8)W(5,6)$ . The two terms in the kernel is called the exchange and direct interaction, and the direct interaction is usually the dominant term that gives the excitonic effect, whereas the exchange term is responsible for the singlet-triplet splitting of excitons.

In practice, the BSE is often written in the basis of non-interacting e-h pairs as a two-particle Schrödinger Equation:

$$(\varepsilon_{ck} - \varepsilon_{vk})A_{vc\mathbf{k}}^S + \sum_{v'c'k'} K_{vc\mathbf{k},v'c'k'}(\Omega^S)A_{v'c'k'}^S = \Omega^S A_{vc\mathbf{k}}^S \quad (2.12)$$

where the Tamm-Dancoff approximation is made [45]. Usually in practice the static approximation to e-h interaction kernel is made (although we are going to relax this condition in Chapter 4), in which case the dominating direct interaction term looks like:

$$K_{vc,v'c',\mathbf{q}=\mathbf{k}-\mathbf{k}'}^d = -\sum_{\mathbf{G}\mathbf{G}'} M_{c'c}^*(\mathbf{k}, \mathbf{q}, \mathbf{G}) M_{v'v}(\mathbf{k}, \mathbf{q}, \mathbf{G}') \varepsilon_{\mathbf{G}\mathbf{G}'}^{-1}(\mathbf{q}) v(\mathbf{q} + \mathbf{G}') \quad (2.13)$$

The eigenstates of Eq. (2.12),

$$|S\rangle = \sum_v^{occ} \sum_c^{empty} \sum_{\mathbf{k}} A_{vc\mathbf{k}}^S |vc\mathbf{k}\rangle \quad (2.14)$$

describes correlated e-h pairs. When the energy of an eigenstate is below the e-h continuum, it is a bound exciton, and  $|S\rangle$  is the exciton wavefunction.

In practice, the BSE calculation is usually done on top of a GW calculation, where the band energies  $\varepsilon_{c\mathbf{k}}$ ,  $\varepsilon_{v\mathbf{k}}$  are the GW-corrected band energies. First, the e-h interaction kernel is calculated from Eq. (2.13) on the same q-point grid on which the dielectric function  $\varepsilon_{\mathbf{G}\mathbf{G}'}^{-1}(\mathbf{q})$  has been calculated. Then the BSE is solved by diagonalizing the matrix given by the left-band side of Eq. (2.12). Often for the description of the exciton wavefunction in BSE, a finer k-point grid is needed than the q-point grid in the kernel. The e-h interaction kernel on the finer grid is interpolated from the coarser grid. Finally, the absorption spectrum is calculated from the BSE eigenstates, as described below.

### 2.3.3 Optical Property

The optical absorption of a solid is given by the imaginary part of the macroscopic dielectric function,  $\varepsilon_2(\omega)$ . Without including e-h correlation, it is given by the summation of independent vertical transitions, derived from the Fermi's golden rule:

$$\epsilon_2(\omega) = \frac{16\pi^2 e^2}{\omega^2} \sum_{\nu c k} |\hat{\mathbf{e}} \cdot \langle \nu \mathbf{k} | \mathbf{v} | c \mathbf{k} \rangle|^2 \delta(\omega - \epsilon_{c k} + \epsilon_{\nu k}) \quad (2.15)$$

where  $\hat{\mathbf{e}} \cdot \langle \nu \mathbf{k} | \mathbf{v} | c \mathbf{k} \rangle$  is the velocity matrix element along the direction of the polarization of light  $\hat{\mathbf{e}}$ . When e-h correlation is considered, the summation goes through the correlated e-h pairs:

$$\epsilon_2(\omega) = \frac{16\pi^2 e^2}{\omega^2} \sum_S |\hat{\mathbf{e}} \cdot \langle 0 | \mathbf{v} | S \rangle|^2 \delta(\omega - \Omega^S) \quad (2.16)$$

In 2D materials, the dielectric function is not a well-defined physical quantity. Instead, one can use the absorbance  $A(\omega)$  to describe how much proportion of light is absorbed going through a single layer of material. In a simulation where the periodicity in the off-plane direction is  $d$ , the absorbance is related to the calculated dielectric function by  $A(\omega) = \omega \epsilon_2(\omega) d / c$ , where  $c$  is the speed of light. Figure 2.2 shows as an example the optical absorbance of monolayer MoS<sub>2</sub> calculated with BSE and using the GW band structure but without e-h correlation. Their large difference is the indication of the strong excitonic effect of MoS<sub>2</sub>.

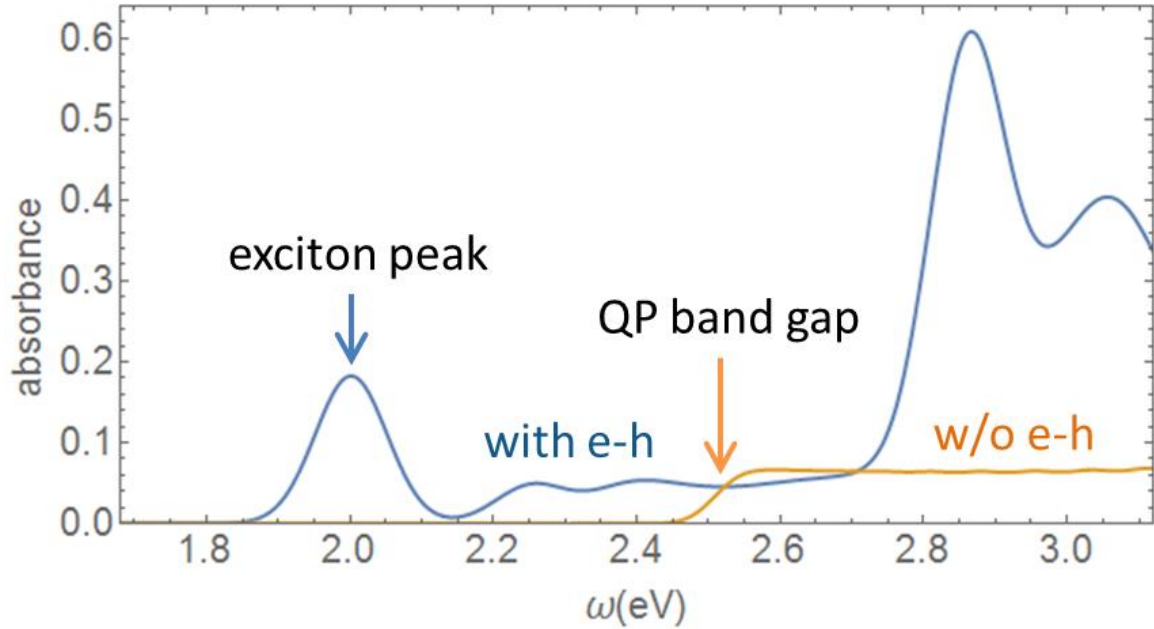


**Figure 2.2** The optical absorbance of monolayer MoS<sub>2</sub> with e-h correlation from BSE (blue line) and with no electron-hole correlation (yellow line).

The first-principles DFT and GW+BSE calculations are high-throughput calculations that usually require running on a supercomputer cluster with parallelization. The works presented in this thesis are calculated using the computational resources of Lonestar, Stampede and Stampede2 clusters at Texas Advanced Computing Center (TACC), provided by the Extreme Science and Engineering Discovery Environment (XSEDE).

# **Chapter 3: Renormalization of the Quasiparticle Band Gap in Doped Two-Dimensional Materials**

## **3.1 Introduction**

Almost all the applications of 2D materials are premised on a good understanding the electronic properties of the material, especially the quasiparticle band gap. The *ab initio* GW method has been the most successful first-principles approach of calculating the quasiparticle band structure of bulk crystals as well as molecules and low-dimensional structures [33, 43, 44, 46]. In particular, well-converged GW results in 2D crystals has been achieved recently as the accurate treatments to 2D screened Coulomb interaction were established [28-31]. However, much less is known about how doping, a common theme in the 2D semiconductors and its heterostructures [4, 47-49], can affect the electronic structure.

Doped free carriers have several effects that are particularly enhanced on the electronic structure of low-dimensional materials. First, the large density-of-states (DOS) from the van Hove singularity magnifies the contribution from electron occupation. Second, the screening from doped free carriers has a stronger effect on lower-dimension structures because of the weaker intrinsic dielectric screening. Third, free carriers in low-dimensional systems form a low-energy acoustic plasmon which can dynamically couple with quasiparticles. These effects result in an enhanced many-body renormalization of quasiparticles energy, as shown from previous theoretical GW calculations in both semiconducting carbon nanotubes [50, 51] and 2D transition metal dichalcogenides (TMDs) [52], and from experimental measurements [53-57]. However, a complete picture of the quasiparticle renormalization within a wide range of doping density is

not clear because of the limitation of k-point-grid-based first-principle method in resolving the low doping density, which is, however, the most essential for experiments and devices.

Moreover, previous works and methods cannot be directly applied to studying several newly emerged 2D materials such as black phosphorus (BP) whose electronic structure is significantly anisotropic.

In this chapter, we have developed an effective mass model and applied asymptotic analysis to resolve band gap renormalization, using the GW approximation and the framework of previous work [52]. The effective mass model supplements the *ab initio* calculation by bridging the gap around low doping density. It reveals that the change of the dielectric screening, which appears in term of the Coulomb-hole self-energy, is the dominating contributing factors to the band gap renormalization at low doping density. The change in electron occupation, which appears in term of the screened-exchange self-energy, is more important at high doping density. Additionally, we study band gap renormalization of doped monolayer BP, where we generalize our method to systems with strong anisotropy and show that the smaller DOS of BP near the band edge enhances the band gap renormalization at high doping density. Finally, we show that the effective mass model allows the calculation of band gap renormalization in lattice-mismatched bilayer system.

The rest of this Chapter is organized as follows: In Section 3.2 we lay down the theoretical framework of our approach, show the computational details, and discuss the materials' intrinsic properties. In Section 3.3 we construct our effective mass model of the GW self-energy and band gap renormalization of doped h-BN and MoS<sub>2</sub>. In Section 3.4, we discuss band gap renormalization of monolayer BP, where our model is generalized to anisotropic systems. In Section 3.5, we discuss band gap renormalization of ReSe<sub>2</sub> on a graphene substrate, where our

model is generalized to bilayer system without lattice matching. Finally, the main results will be summarized in Section 3.6.

## 3.2 Computational Details and Intrinsic Properties

In this chapter, we choose three prototypical monolayer 2D structures, including hexagonal BN (h-BN), 2H-phase MoS<sub>2</sub>, and BP, and one bilayer 2D heterostructure, ReSe<sub>2</sub> on top of graphene. They cover 2D materials from semiconductors to insulators and from isotropic ones to anisotropic ones. To study the effect of doping, we calculate the quasiparticle band structure of these materials from the first-principles DFT+GW method. The DFT calculation serves as a mean-field starting point for the GW calculation. It is performed using the plane-wave pseudopotential method implemented in Quantum Espresso [39]. The GGA-PBE exchange-correlation functional [58] is used along with a plane-wave cutoff of 90 Ry, 75 Ry, 35 Ry and 100 Ry for h-BN, MoS<sub>2</sub>, BP and ReSe<sub>2</sub>, respectively. Doping is introduced by changing the total electron number with a compensating jellium background. This resembles the gate-tunable electrostatic doping commonly seen in 2D materials. Our calculation shows that doping has very little effects on the DFT eigenvalues and wavefunctions. This is not surprising because DFT is known for its deficiency at capturing many-electron effects that are, however, crucial for our studied band gap renormalization.

Beyond DFT, we employ the GW approximation to study quasiparticle energies. The self-energy in a doped material is expanded into three terms:

$$\Sigma = iGW = i(G_{int}W_{int} + \delta GW_{int} + G_{int}\delta W + \delta G\delta W) \equiv \Sigma_{int} + \Sigma_1 + \Sigma_2 + \Sigma_3 \quad (3.1)$$

The first, ‘‘intrinsic’’ term ( $\Sigma_{int}$ ) indicates the self-energy contribution coming from the intrinsic (undoped) system. The second term ( $\Sigma_1$ ) is the self-energy correction due to the change of



electron (hole) occupation alone under the intrinsic screening. The third term ( $\Sigma_2$ ) is due to the change in screening, and the last term ( $\Sigma_3$ ) is related to both factors. The calculation details of these doping-related terms will be discussed in the next section. As we will see, the dielectric screening  $W = \epsilon^{-1}v$  and its change upon doping  $\delta W$  play a central role in this band gap renormalization.

The intrinsic term ( $\Sigma_{int}$ ) of the self-energy is calculated with the usual GW routine implemented in the BerkeleyGW package [44]. Truncated Coulomb interaction [59] is used along with sufficient vacuum to eliminate interactions between layers. The static dielectric function is calculated within the random phase approximation (RPA) with 8 Ry energy cutoff, 120 and 140 conduction bands, and  $24 \times 24 \times 1$  and  $28 \times 20 \times 1$  k-point grid respectively for h-BN and BP, which grants a converged band gap within 0.1 eV. For ReSe<sub>2</sub>, 10 Ry cutoff, 320 conduction bands and  $10 \times 10 \times 1$  k-point grid is used. For MoS<sub>2</sub>, 10 Ry cutoff, 256 conduction bands and  $24 \times 24 \times 1$  k-point grid is used. Although it has been shown that the true convergence of the band gap in MoS<sub>2</sub> would require a much larger number of bands and dielectric cutoff [30], as far as our main concern of band gap renormalization goes, this set of parameters is enough. This is because the doping effect is mainly concentrated on small  $q$  and head ( $G=G'=0$ ) part of the dielectric function  $\epsilon_{\mathbf{G}\mathbf{G}'}^{-1}(\mathbf{q}, \omega)$  [52]. The dynamical part of the dielectric function is then constructed from the generalized plasmon-pole (GPP) model.

Figure 3.1 shows the calculated static dielectric function  $\epsilon_{\mathbf{0}\mathbf{0}}^{-1}(\mathbf{q}, \omega = 0)$  of intrinsic h-BN, MoS<sub>2</sub> and BP. The dielectric function approaches 1 in the limit as  $q \rightarrow 0$ , following the formula  $\epsilon_{\mathbf{0}\mathbf{0}}^{-1}(\mathbf{q}) \approx 1/(1 + 2\pi\alpha_{2D}q)$ , where the 2D polarizability  $\alpha_{2D}$  captures the macroscopic dielectric screening behavior of 2D materials [27]. Due to this weaker screening, 2D semiconductors and

insulators have unusually large quasiparticle band gaps, exciton binding energies and band gap renormalizations compared with their bulk counterparts.

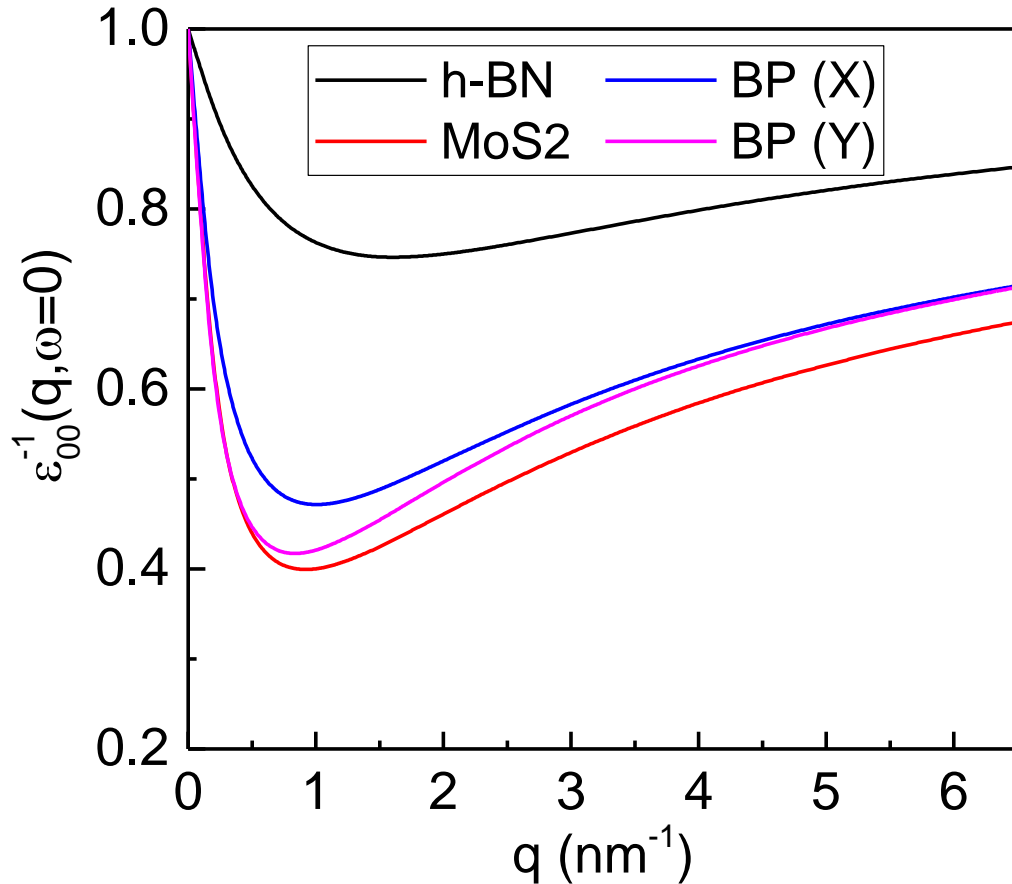


**Figure 3.1** Static dielectric function  $\epsilon_{00}^{-1}(\mathbf{q}, \omega = 0)$  of intrinsic h-BN, MoS<sub>2</sub> and BP with the same size of vacuum (20Å).

### 3.3 GW Self-Energy and Effective Mass Model: h-BN and MoS<sub>2</sub>

As we can see from Eq. (3.1), to determine the quasiparticle self-energy of the doped system, the primary goal is to find the change in the dielectric screening, given by the dielectric function  $\delta\epsilon_{\mathbf{G}\mathbf{G}'}^{-1}(\mathbf{q}, \omega)$  of a 2D crystal. To illustrate this process in detail, we use p-doped h-BN as an example. h-BN is a wide-gap 2D insulator which has been commonly used as substrate and

encapsulation for other 2D materials in Van der Waals heterostructures [60]. Its valence band maximum (VBM) is at the K point and conduction band minimum (CBM) at  $\Gamma$  point.

For a doped system, the change to the dielectric screening is concentrated on the head part of the dielectric function with small  $q$  and low frequency  $\omega$  and requires a smaller number of bands to converge [52]. For this purpose, within the first-principles approach, the static dielectric function  $\epsilon_{00}^{-1}(\mathbf{q}, \omega = 0)$  of the doped system is calculated on an  $120 \times 120 \times 1$  k-point grid, as shown by the dots in Fig. 3.2. For the frequency-dependent part, a simple plasmon-pole model

$\delta\epsilon_{00}^{-1}(\mathbf{q}, \omega) = \frac{\delta\epsilon_{00}^{-1}(\mathbf{q}, 0)\omega_d^2(\mathbf{q})}{\omega^2 - \omega_d^2(\mathbf{q})}$ , where  $\delta\epsilon_{00}^{-1}(\mathbf{q}, 0) = \epsilon_{00}^{-1}(\mathbf{q}, 0) - \epsilon_{int,00}^{-1}(\mathbf{q}, 0)$ , well describes the difference between the intrinsic and doped dielectric function, and the plasmon frequency  $\omega_d(\mathbf{q})$  is extracted from the *ab initio* calculation and shown in the inset of Fig. 3.2.

Following ref. [52], the GW self-energy of the doped system can be calculated according to Eq.

(3.1) term by term. The first correction term  $\Sigma_1$  is given by

$$\begin{aligned} \Sigma_1^{nk}(E) = & - \sum_{\mathbf{G}, \mathbf{G}'} \int \frac{d^2q}{(2\pi)^2} f_{n, \mathbf{k}-\mathbf{q}} M_{vn}^*(\mathbf{k}, -\mathbf{q}, -\mathbf{G}) M_{vn}(\mathbf{k}, -\mathbf{q}, -\mathbf{G}') \\ & \times \epsilon_{int, \mathbf{G}\mathbf{G}'}^{-1}(\mathbf{q}, E - \epsilon_{n, \mathbf{k}-\mathbf{q}}) v_{2D}(\mathbf{q} + \mathbf{G}') \end{aligned} \quad (3.2)$$

where  $v$  is the doped band index,  $f_{nk}$  is the electron occupation,  $\epsilon_{nk}$  is the mean-field (DFT) energy and  $M_{nn'}(\mathbf{k}, \mathbf{q}, \mathbf{G})$  is the plane-wave matrix element. This self-energy is calculated from first-principle by taking the difference of the total self-energy of the intrinsic system from that of a doped one, both of which are evaluated with the dielectric function of the intrinsic system. To capture the change in occupation, the intrinsic dielectric function is calculated on a relatively dense k-point grid of  $36 \times 36 \times 1$ .

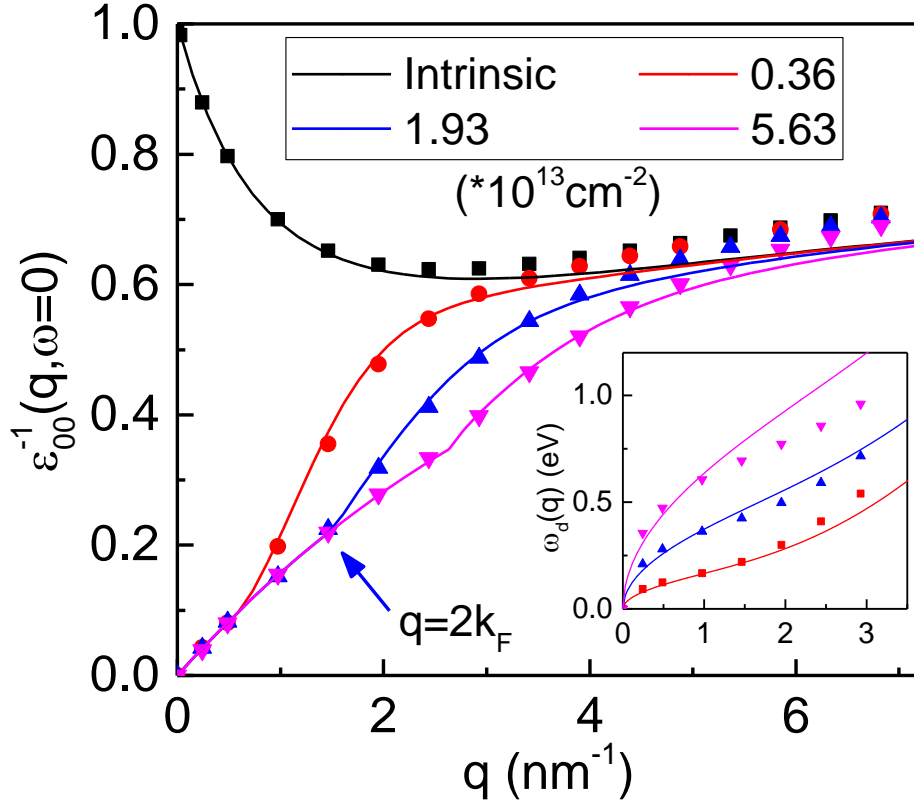


**Figure 3.2** Static dielectric function of p-doped h-BN. Dots are from the *ab initio* calculation and the solid lines come from the effective mass model. The inset shows the plasmon-pole frequency.

The other two terms  $\Sigma_2$  and  $\Sigma_3$  are expressed in summations that only involve intra-band transitions with small momentum as follow:

$$\Sigma_2^{nk}(E) = \pm \int \frac{d^2q}{(2\pi)^2} |M_{nn}(\mathbf{k}, -\mathbf{q}, \mathbf{0})|^2 \frac{\delta\epsilon_{00}^{-1}(q, 0)}{2 \left[ 1 \pm \frac{\epsilon_{n, \mathbf{k}-\mathbf{q}} - E}{\omega_d(q)} \right]} \nu_{2D}(q) \quad (3.3)$$

$$\Sigma_3^{nk}(E) = - \int \frac{d^2q}{(2\pi)^2} \delta f_{n, \mathbf{k}-\mathbf{q}} |M_{nn}(\mathbf{k}, -\mathbf{q}, \mathbf{0})|^2 \frac{\delta\epsilon_{00}^{-1}(q, 0)}{1 - \left[ \frac{\epsilon_{n, \mathbf{k}-\mathbf{q}} - E}{\omega_d(q)} \right]^2} \nu_{2D}(q) \quad (3.4)$$

The  $\pm$  in Eq. (3.3) is for conduction and valence states, respectively. Due to the interaction of the quasiparticle with the low-energy acoustic plasmon,  $\Sigma_2$  and  $\Sigma_3$  contains a resonance profile near the mean-field energy  $\epsilon_{nk}$ . To this end, we employ the “on-shell” approximation to  $\Sigma_2$  and  $\Sigma_3$  by

rigidly shifting the whole resonance profile along the energy axis such that the on-shell energy coincides with the QP solution [23]. The on-shell self-energy  $\Sigma_1$ ,  $\Sigma_2$  and  $\Sigma_3$  of the VBM and CBM at K for p-doped h-BN calculated from first-principles are shown by the dots on Fig. 3.3.

However, this first-principles approach suffers a drawback as the dense k-point sampling required to accurately capture the electron occupation and dielectric screening limits its resolution at smaller doping density ( $\sim 10^{12}/\text{cm}^{-2}$ ), which is, unfortunately, the most useful range for device applications. Therefore, we propose a first-principle-based effective mass model to solve this problem and gain insight for the band gap renormalization behavior at low doping density.

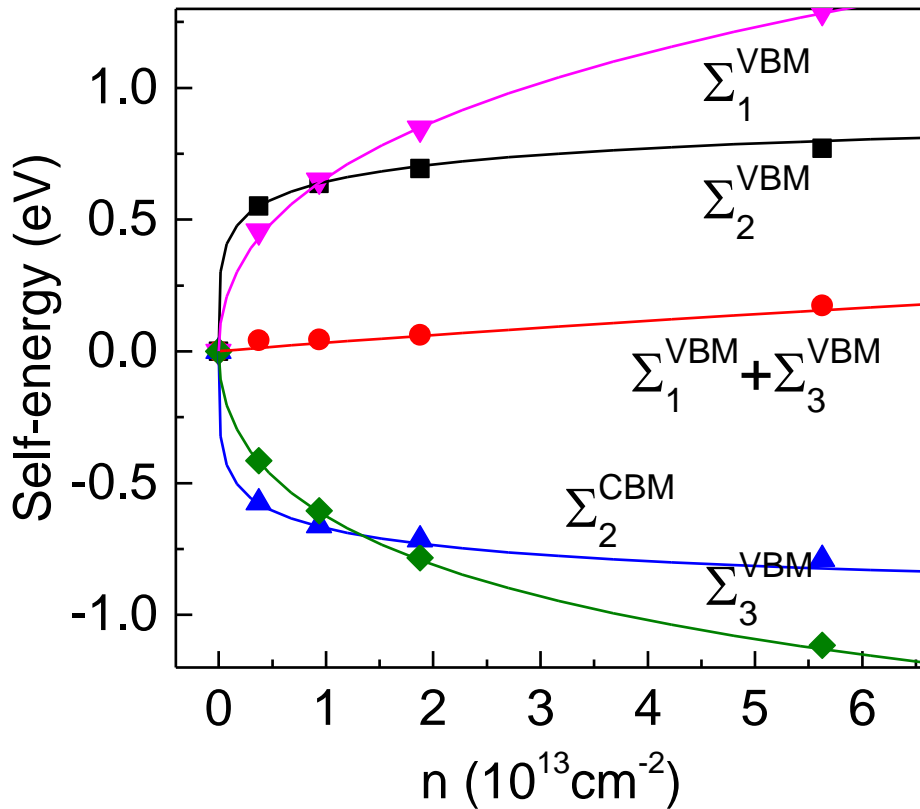


**Figure 3.3** On-shell self-energy of p-doped h-BN at VBM and CBM. Dots represent the *ab initio* result and the solid line is from the effective mass model.

To construct the effective mass approximation for the dielectric function, we decompose the static polarizability function  $\chi$  of the doped system as a sum of interband transitions and intraband transitions within the doped band. We assume the interband part remains the same as the polarizability of the intrinsic system, neglecting the small contributions from the virtual interband transitions near the VBM. The intraband part, within the effective mass approximation, is approximated by the non-interacting polarizability of the two-dimensional electron gas (2DEG), given by the Lindhard function [61]:

$$\chi^{2DEG}(\mathbf{q}, \omega = 0) = -\frac{N_s N_v m^*}{2\pi} [1 - \Theta(q - 2k_F) \sqrt{1 - \frac{4k_F^2}{q^2}}], \quad (3.5)$$

where  $N_s = N_v = 2$  is the spin and valley degeneracy,  $m^*$  is the effective mass of the 2DEG ( $m^* = 0.78$  for p-doped h-BN),  $k_F$  is the fermi wave vector and  $\Theta$  is the step function. The singularity of  $\chi^{2DEG}$  at  $q = 2k_F$  manifests itself as a kink in the dielectric function, as indicated by the arrow in Fig. 3.2.

Given the assumptions above, the static polarizability within the effective mass model is

$\chi_{\mathbf{G}\mathbf{G}'}(\mathbf{q}, 0) = \chi_{\mathbf{G}\mathbf{G}'}^{int}(\mathbf{q}, 0) + \frac{1}{L} \chi^{2DEG}(\mathbf{q}, 0)$  for all G-vectors with  $G_x = G_y = 0$ , where L is the cell periodicity in the z-direction. The RPA dielectric function is then determined by  $\epsilon_{\mathbf{G}\mathbf{G}'}(\mathbf{q}, 0) = \delta_{\mathbf{G}\mathbf{G}'} - \chi_{\mathbf{G}\mathbf{G}'}(\mathbf{q}, 0) v_{2D}(\mathbf{q} + \mathbf{G}')$ , where  $v_{2D}(\mathbf{q}) = \frac{4\pi}{q^2} [1 - e^{-\mathbf{q}_{xy}L/2} \cos(\frac{q_z L}{2})]$  is the 2D truncated Coulomb interaction. The input from *ab initio* calculations can be further reduced by observing that the behavior of the intrinsic polarizability  $\chi_{\mathbf{G}\mathbf{G}'}^{int}(\mathbf{q}, 0)$  as  $q \rightarrow 0$  is determined by the 2D polarizability:  $\chi_{\mathbf{G}\mathbf{G}'}^{int}(\mathbf{q}, 0) = \chi_{\mathbf{G}\mathbf{G}'}^{int}(0,0) - \frac{\alpha_{2D}}{L} q^2$ . In practice, we find that only including the  $G_z = 0, \pm 1$  elements of  $\chi_{\mathbf{G}\mathbf{G}'}^{int}(0,0)$  is sufficient to construct an effective mass model for  $\epsilon_{\mathbf{0}\mathbf{0}}^{-1}(\mathbf{q}, 0)$  that accurately reproduces the *ab initio* one, as shown by the lines in Fig. 3.2. Meanwhile, within the

effective mass approximation, the plasmon-pole frequency follows the 2DEG dispersion relation

$$\omega_d^{2DEG}(\mathbf{q}) = \sqrt{\frac{2\pi n q}{m} \left(1 + \frac{q}{2}\right)^2 \left(1 + \frac{q^3}{8\pi n} + \frac{q^4}{32\pi n}\right) / \left(1 + \frac{q}{4}\right)} \quad [62],$$

which also fits the *ab initio* values well, as shown by the inset of Fig. 3.2.

With the effective mass model, we calculate the asymptotic behavior of self-energy terms Eq. (3.2)-(3.4) in the low density limit. At low doping density, keeping only the leading contribution,  $\Sigma_1$  at the VBM reduces to

$$\Sigma_1^{VBM} \sim \int_{q < k_F} \frac{d^2 \mathbf{q}}{(2\pi)^2} \epsilon_{int,00}^{-1}(\mathbf{q}, 0) v_{2D}(\mathbf{q}). \quad (3.6)$$

Meanwhile, the on-shell self-energy  $\Sigma_2$  and  $\Sigma_3$  are reduced to the following as  $q \rightarrow 0$ :

$$\Sigma_2^{VBM} \sim -\frac{1}{2} \int \frac{d^2 \mathbf{q}}{(2\pi)^2} \frac{\delta \epsilon_{00}^{-1}(\mathbf{q}, 0)}{1 - \epsilon_q / \omega_d(\mathbf{q})} v_{2D}(\mathbf{q}), \quad (3.7)$$

$$\Sigma_3^{VBM} \sim \int_{q < k_F} \frac{d^2 \mathbf{q}}{(2\pi)^2} \delta \epsilon_{00}^{-1}(\mathbf{q}, 0) v_{2D}(\mathbf{q}), \quad (3.8)$$

where the term  $\epsilon_q / \omega_d(\mathbf{q})$  is dropped from Eq. (3.4) because as  $q \rightarrow 0$ ,  $\epsilon_q \propto q^2$  while  $\omega_d(\mathbf{q}) \propto \sqrt{q}$  so  $\epsilon_q / \omega_d(\mathbf{q}) \rightarrow 0$ . In the leading order, both  $\Sigma_1$  and  $\Sigma_3$  affect only the band which has been doped (and does not affect the self-energy at the CBM), while  $\Sigma_2$  affects all states at the same time.

Equations (3.6) and (3.8) share a similar form of an integral over the doped region. Equation (3.6) shows that  $\Sigma_1$  correspond to “bare” exchange energy of a 2DEG, where the bare interaction refers to the screened interaction of the intrinsic system without the additional screening from the 2DEG. Meanwhile, Eq. (3.8) suggests that  $\Sigma_3$  correspond to the difference between the “bare” exchange and the screened exchange energy of 2DEG. In fact,  $\Sigma_3$  cancels most part of  $\Sigma_1$ ,

because  $\epsilon_{int,00}^{-1}(\mathbf{q}, 0) \gg \epsilon_{00}^{-1}(\mathbf{q}, 0)$  for  $q < k_F$  and thus  $\Sigma_1 \gg \Sigma_1 + \Sigma_3$ . Their sum

$$\Sigma_1^{VBM} + \Sigma_3^{VBM} \sim \int_{q < k_F} \frac{d^2\mathbf{q}}{(2\pi)^2} \epsilon_{00}^{-1}(\mathbf{q}, 0) v_{2D}(\mathbf{q}) \quad (3.9)$$

is the actual screened exchange contribution to the self-energy. It grows linearly with the doping density because  $\epsilon_{00}^{-1}(\mathbf{q}, 0)$  is linear in  $q$  as  $q \rightarrow 0$ . Due to the 2DEG polarizability from Eq. (3.5), it is also proportional to inverse of the density-of-state effective mass  $1/N_s N_v m^*$ . The linear behavior from this asymptotic analysis, as shown by the red line from Fig. 3.3, accurately describes the *ab initio* results, and works well even up to relatively high doping density.

On the other hand,  $\Sigma_2$ , which corresponds to the Coulomb-hole part of the self-energy [42], has a very different asymptotic behavior at low doping density. The integral in Eq. (3.7) goes over the whole BZ. As the integrand, the change in dielectric function  $\delta\epsilon_{00}^{-1}(\mathbf{q}, 0)$ , given by the difference between the curves in Fig. 3.2, is rapidly increasing at low doping density but saturates at high doping density. This causes the term  $\Sigma_2$  to dominate the low-density part of the band gap renormalization and saturate at high density. The self-energy calculated from Eq. (3.7) is shown by the black and blue curves in Fig. 3.3 and they are also in good agreement with the *ab initio* results. To sum up, it is shown that the band gap renormalization is dominated by the nonlinear Coulomb-hole term ( $\Sigma_2$ ) in the low doping density region, while the linearly increasing screened exchange term ( $\Sigma_1 + \Sigma_3$ ) takes over in the high doping density region as the Coulomb-hole term saturates.

Finally, we show the quasiparticle band gap renormalization of p-doped h-BN in Fig. 3.4. Based on our calculated DFT and GW band structure shown in Fig. 3.4 (a), intrinsic h-BN has an indirect band gap of 6.4 eV with VBM at the K point and CBM at  $\Gamma$  point of the Brillouin zone.

The direct band gap at K is 7.3 eV. Fig. 3.4 (b) shows the renormalization of the direct band gap



at K. With hole doping, the band gap drops rapidly by about 1 eV with doping density around  $10^{12}$ - $10^{13}\text{cm}^{-2}$ . With further increase in doping density, the band gap renormalization saturates to a slower rate. The renormalizations of the VBM and CBM quasiparticle energy are shown in the inset of Fig. 3.4 (b). They are nearly symmetric because the dominating Coulomb-hole self-energy term given by Eq. (3.7), which is not sensitive to which band is occupied by doped carriers, makes almost equal but opposite contribution to valence and conduction band. The small asymmetry is from the fact that the screened exchange term affects the doped band, causing the VBM energy to have a larger shift than the CBM at large doping density.

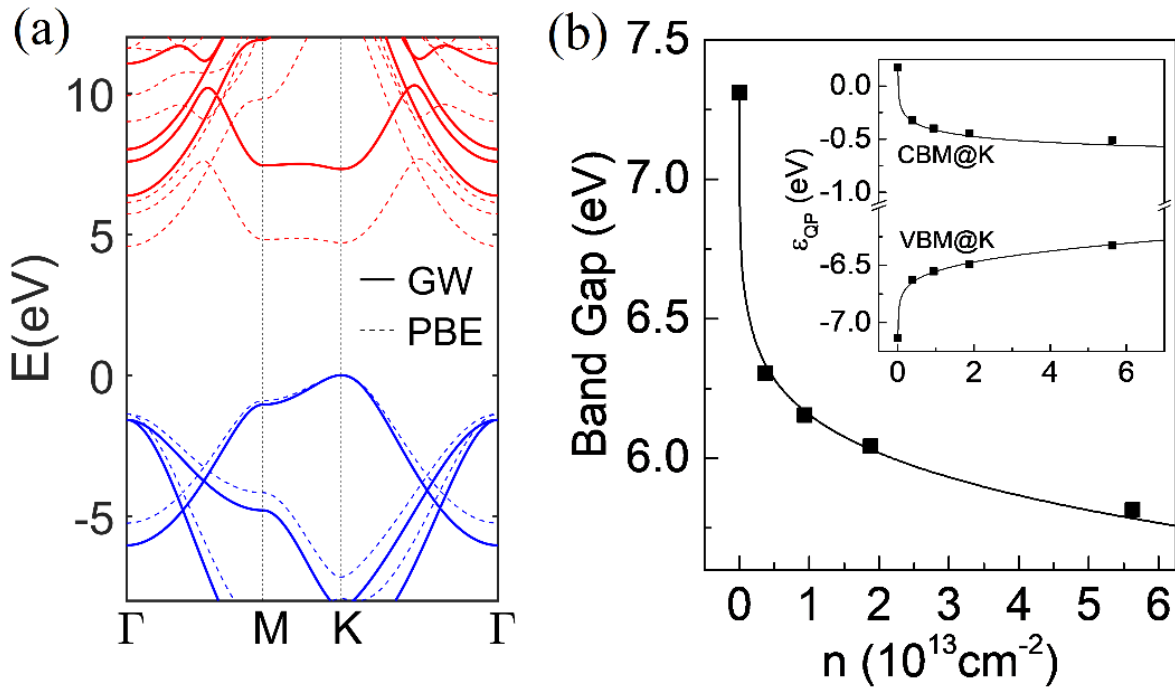


**Figure 3.4** (a) DFT and GW band structure of intrinsic  $h$ -BN. (b) Renormalization of the direct band gap at K for  $p$ -doped  $h$ -BN. Inset shows the quasiparticle energy. Dots represent the *ab initio* result and the solid line is from the effective mass model.

In Fig. 3.5, we show similar results for the  $n$ -doped  $\text{MoS}_2$ . Despite having a much smaller intrinsic band gap around 2.7 eV (without considering the spin-orbit coupling),  $\text{MoS}_2$  shares

similar honeycomb lattice structure and isotropic effective mass with h-BN. Therefore, MoS<sub>2</sub> shows a similar band gap renormalization behavior. A moderate doping density around  $10^{13} \text{ cm}^{-2}$  can induce a band gap reduction of 400 meV. The solid line is from our effective mass model. It perfectly captures the low-density results while slightly overestimates the reduction for high doping densities. This is not surprising because our effective mass model does not include the band structure effects and the off-diagonal elements of the dielectric function, which would gradually gain importance at higher doping density.

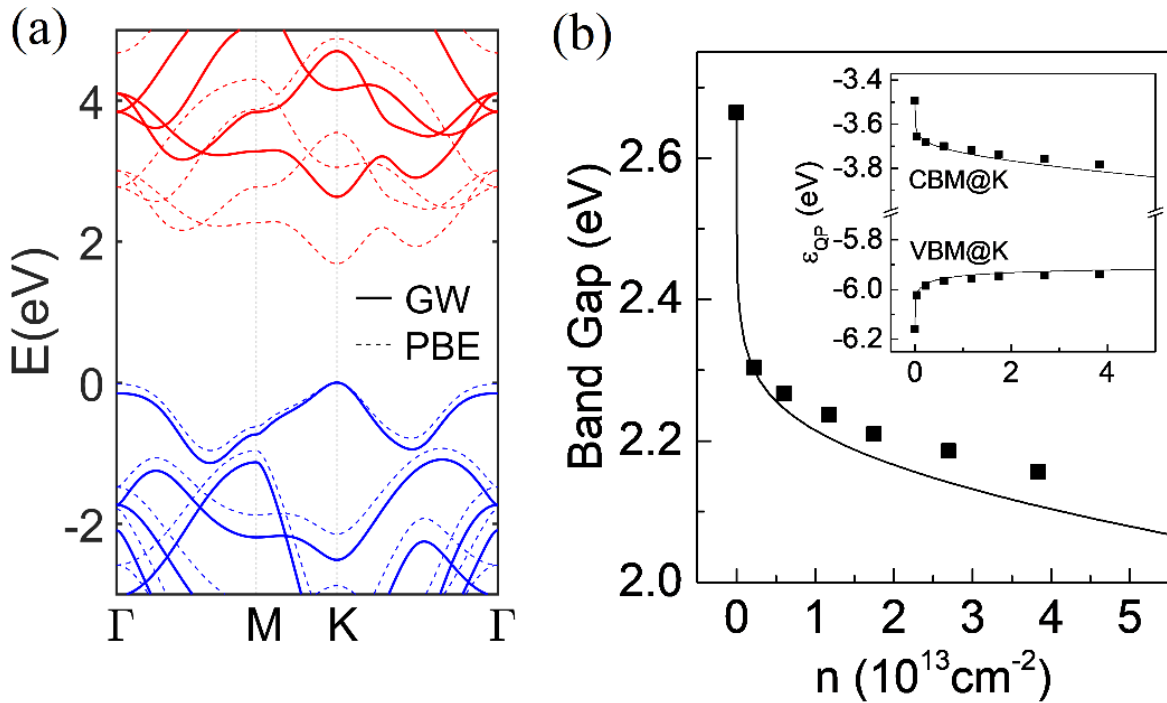


**Figure 3.5** (a) DFT and GW band structure of intrinsic MoS<sub>2</sub>. (b) Quasiparticle band gap renormalization of  $n$ -doped MoS<sub>2</sub>. Dots represent the *ab initio* result and the solid line is from the effective mass model.

### 3.4 Band Gap Renormalization of Monolayer Black Phosphorus

BP is a layered semiconductor that has attracted great interest recently [4, 63, 64]. It has a direct band gap that is tunable with the number of layers, ranging from 0.3 eV in bulk to 2.0 eV in a monolayer [25]. Adatoms and doping have been found to strongly affect the band gap of thin-film BP [65]. It also shows strong in-plane anisotropy, which results in unusual behaviors of anisotropic exciton and thermal and electrical transport [66, 67]. The band structure of monolayer BP is shown in Fig. 3.7 (a). The most special character is that, near the band edge at  $\Gamma$  point, BP has a parabolic band dispersion with large effective mass in the x (zigzag)-direction and an almost linear band dispersion with very small effective mass in the y (armchair)-direction. Consequently, the screening in intrinsic and doped BP are also anisotropic. Therefore, we must modify the above isotropic effective mass model to calculate the band gap renormalization in doped monolayer BP.

The static dielectric function  $\epsilon_{00}^{-1}(\mathbf{q}, \omega = 0)$  of intrinsic and doped BP is calculated on a  $112 \times 80 \times 1$  k-point grid and their values along the x- and y-directions are shown in Fig. 3.6 (a), respectively. It is clear that the dielectric screening of both the intrinsic and doped system are anisotropic. Notably the kink at  $q = 2k_F$  due to the singularity in the 2DEG polarizability is still present in the dielectric function of doped BP, although  $k_F$  takes different values in x and y directions. Before the kink  $\epsilon^{-1}$  is isotropic and corresponds to a constant polarizability of the 2DEG despite its anisotropic effective mass, while after the kink  $\epsilon^{-1}$  turns up and merges into the intrinsic dielectric function. It should be noted that although the effective mass along x- and y-directions differ by about a factor of 7, the difference of the intrinsic and doped dielectric function is only weakly dependent on the direction of  $\mathbf{q}$ .

Contrast to the static case, the band anisotropy has a much greater impact on the frequency-dependent part of the dielectric function. The polar plot in Fig. 3.6 (b) shows the loss function  $Im[\epsilon_{00}^{-1}(\mathbf{q}, \omega)]$  as a function of  $\omega$  and the direction of  $\mathbf{q}$ . The darker region in the plot corresponds to a peak in the loss function corresponding to the plasmon excitation, showing that the plasmon is highly anisotropic in BP. We find that the angular-dependent plasmon frequency can be well fitted by the relation  $\omega_d(\mathbf{q}) \propto \sqrt{\frac{\cos^2 \theta}{m_x} + \frac{\sin^2 \theta}{m_y}}$ , where  $m_x = 1.22m_0$  and  $m_y = 0.16m_0$  are the electron effective masses in the two directions and  $\theta$  is the direction of  $\mathbf{q}$ . Apart from this anisotropy, the plasmon frequency follows the characteristic of 2DEG and is proportional to  $\sqrt{q}$  and  $\sqrt{n}$  for small  $q$  and low doping density  $n$ . The screening properties of BP obtained with our ab initio calculation agree well with a previous study using the effective Hamiltonian approach [68].

The quasiparticle self-energy of the doped BP is expanded similarly into  $\Sigma_1$ ,  $\Sigma_2$  and  $\Sigma_3$  following Eq. (3.1). Each term is calculated according to Eq. (3.2)-(3.4) with the difference that the integral over  $q$  now needs to be done in 2D instead of 1D. The ab initio static dielectric function  $\epsilon_{00}^{-1}(\mathbf{q}, \omega = 0)$  and the plasmon frequency  $\omega_d(\mathbf{q})$  on the 2D grid is used as input for the integrals. We find these two-dimensional integrals can be further simplified by modelling the angular dependence of  $\epsilon_{00}^{-1}(\mathbf{q}, \omega = 0)$  and  $\omega_d(\mathbf{q})$ . By assuming  $\delta\epsilon_{00}^{-1}(\mathbf{q}, \omega = 0)$  to be the average of x- and y-direction and isotropic, as well as using the angular dependence of  $\omega_d(\mathbf{q})$  shown above, we can further reduce the  $q$ -points needed to for the ab initio calculation to only along the line  $\Gamma$ -X and  $\Gamma$ -Y. This yields similar result to the full 2D integration with a difference in the on-shell self-energy at VBM and CBM of less than 10 meV.

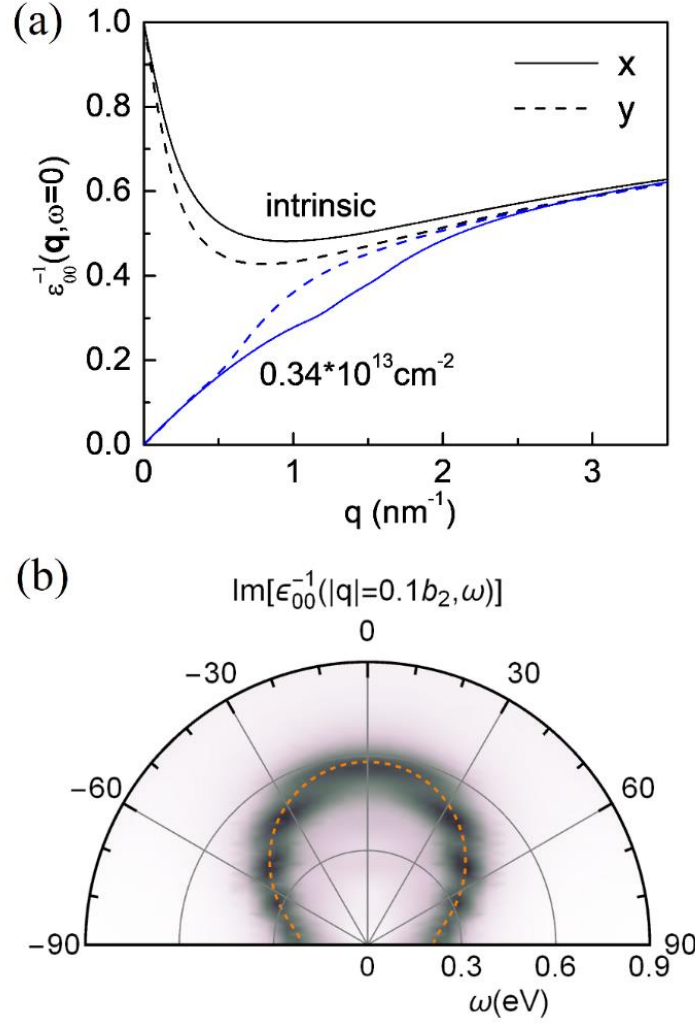


**Figure 3.6** (a) First-principles static dielectric function of  $n$ -doped BP in different direction. (b) Polar plot of the loss function in  $n$ -doped BP. The dashed line is a fit to the plasmon frequency with the anisotropic effective mass.

The resulting quasiparticle band gap renormalization of  $n$ -doped BP is shown in Fig. 3.7 (b). The quasiparticle band gap drops rapidly from 1.95eV to around 1.58eV with light doping up to density  $n = 2 \times 10^{12} \text{cm}^{-2}$ . However, there is a notable difference from h-BN and MoS<sub>2</sub> that the band gap renormalization of BP is less saturated at high doping density. As the inset in Fig. 3.7 (b) shows, this is due to a continued decrease of the CBM quasiparticle energy at large doping density, while the VBM quasiparticle energy has already saturated to nearly constant. The on-

shell self-energy values at VBM and CBM, shown in Fig. 3.7 (c) and (d), reveal the reason behind this unusual behavior. Same as h-BN and MoS<sub>2</sub>, the Coulomb-hole term  $\Sigma_2$ , as shown by the red curves, is dominant at low doping density but saturates at higher doping density. However, the screened-exchange term  $\Sigma_1+\Sigma_3$  as shown by the magenta curve in Fig. 3.7 (d), which controls the CBM self-energy renormalization at high density, is notably larger than that in h-BN and MoS<sub>2</sub>. As we have discussed in the asymptotic analysis, the screened-exchange self-energy is inversely proportional to the density-of-state effective mass. Due to the lack of valley degeneracy and highly anisotropic, quasi-1D band dispersion, electrons in BP has a small DOS effective mass  $\sqrt{m_x m_y} \approx 0.44$ , which is about 2 times smaller than MoS<sub>2</sub> and 3 times smaller than h-BN. The calculated slope of the screened-exchange self-energy versus doping density is indeed 3 times larger for BP than h-BN, which confirms that the smaller DOS of BP is the root cause of its large, unsaturated band gap renormalization.

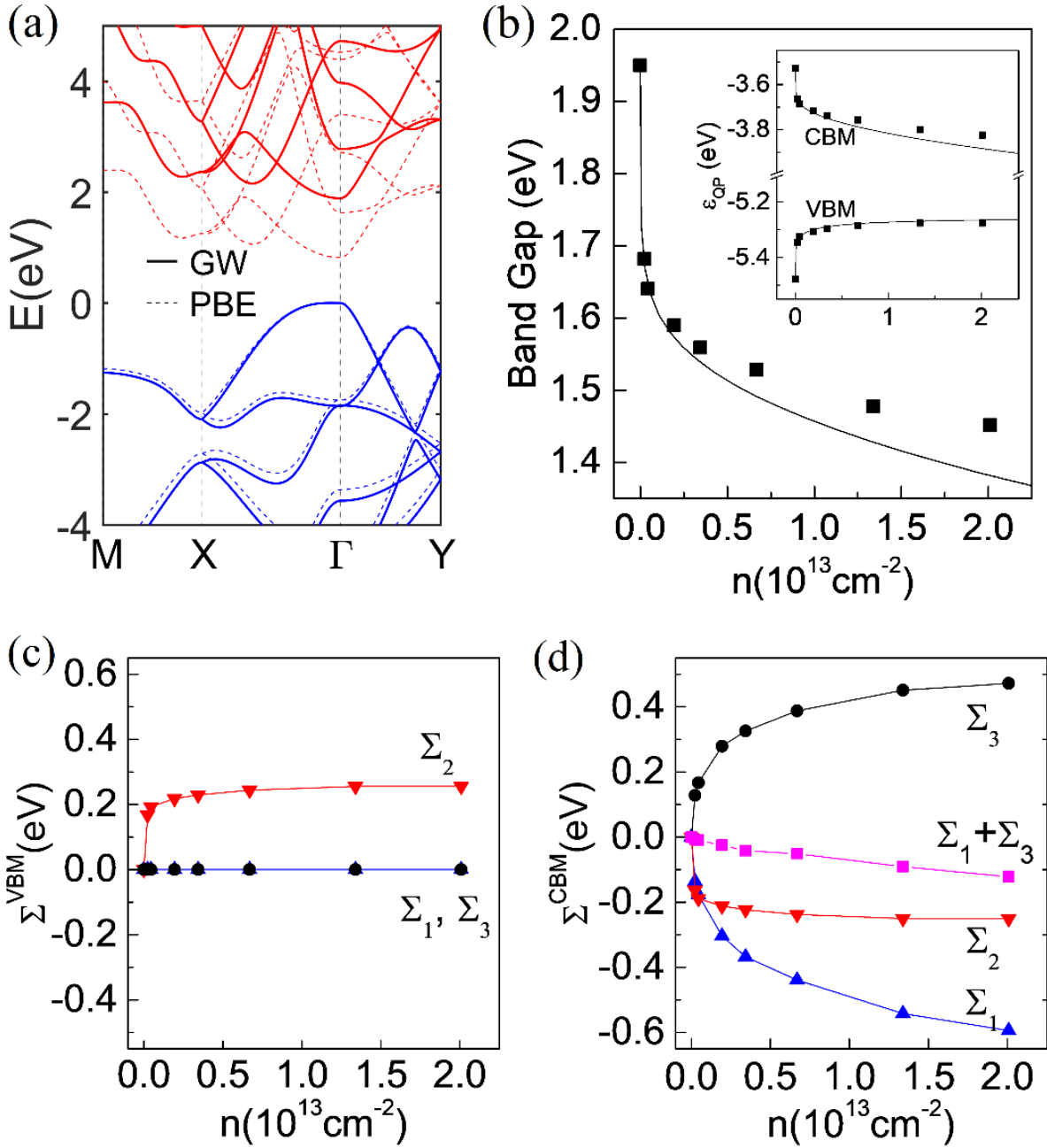


**Figure 3.7** (a) DFT and GW band structure of intrinsic BP. (b) Quasiparticle band gap renormalization of  $n$ -doped BP. Dots represent the *ab initio* result and the solid lines are from the effective mass model. (c) (d) The on-shell self-energy  $\Sigma_1$ ,  $\Sigma_2$  and  $\Sigma_3$  at the VBM and CBM as a function of doping density.

### 3.5 Band Gap Renormalization of ReSe<sub>2</sub> on Graphene

Direct *ab initio* calculation on multiple layers of different 2D materials can be difficult in general due to the existence of lattice mismatch, which leads to very large unit cell or no unit cell at all. However, most experimental studies of 2D material involve some substrate that are adjacent to the monolayer, which can strongly modify the dielectric screening properties of the material and lead to different band gap renormalization behavior. The effective mass model of band gap renormalization we have developed neglects the details of the crystal structure and only uses the physical quantities that are macroscopic in the in-plane direction. Therefore, it can be generalized to deal with such cases. Here we demonstrate such a calculation, dealing with the band gap renormalization of monolayer 1T-ReSe<sub>2</sub> placed on top of a single layer of graphene substrate. ReSe<sub>2</sub> is a newly-discovered 2D TMDC with direct band gap and in-plane anisotropic electronic and optical properties [69-71].

We start with the case of free-standing monolayer ReSe<sub>2</sub>, which have a calculated intrinsic direct band gap of 2.17 eV at the  $\Gamma$  point within  $G_0W_0$  approximation. Following the procedure in Section 3.3, the change in the quasiparticle self-energy at the band edge is calculated with effective-mass model. We use an electron effective mass of  $0.96m_0$  and hole effective mass of  $1.24m_0$  (where  $m_0$  is the bare electron mass), obtained by fitting the first-principle DFT band structure, and a 2D polarizability  $\alpha_{2D} = 6.9 \text{ \AA}$ , obtained by fitting the dielectric function at small q-vector according to  $\epsilon_{00}^{-1}(\mathbf{q}, \omega = 0) \approx 1/(1 + 2\pi\alpha_{2D}q)$ . As shown in Figure 3.8 (a), a substantial band gap renormalization is observed, which starts off rapidly at low doping density where the dominant contribution comes from the Coulomb-hole self-energy, and gradually transforms into a linear trend where the dominant contribution comes from the screened-exchange self-energy. Within a



doping density of  $10^{12} \text{ cm}^{-2}$ , the quasiparticle band gap of a freestanding monolayer is reduced by 320 meV, which is significantly larger than the experimental measurements [72].

This overestimated band gap renormalization may be from the graphene substrate, which introduces extra dielectric screening that shall significantly reduce the self-energy correction and quasiparticle band gap. A direct GW calculation combining ReSe<sub>2</sub> and graphene is a formidable if not impossible task due to lattice mismatch. However, the lattice mismatch problem can be bypassed here for the calculation of doping effect, by taking advantage of the fact that the band gap renormalization is mainly decided by dielectric screening of the long-wave and low-frequency limit. To this end, for monolayer ReSe<sub>2</sub> on graphene substrate, we compute the non-interacting static polarizability of the whole system at small  $\mathbf{q}$  and zero in-plane G-vector by summing the polarizability of individual ReSe<sub>2</sub> and graphene layers:

$$\chi_{G_z G'_z}(\mathbf{q}, \omega = 0) = \chi_{G_z G'_z}^{Re}(\mathbf{q}, 0) + \chi_{G_z G'_z}^{gra}(\mathbf{q}, 0) \quad (3.10)$$

For each layer, the asymptotic behavior of the polarizability at low doping density and small q-vector is used:

$$\chi_{G_z G'_z}^{Re}(\mathbf{q}, 0) = \left(\frac{2\pi}{L}\right)^2 f_{Re}^*(G_z) f_{Re}(G_z - G'_z) G_z G'_z + \frac{1}{L} (-\alpha_{2D} q^2 + \chi^{2DEG}(q, \omega = 0; n_{Re})) f_{Re}(G_z - G'_z) \quad (3.11)$$

$$\chi_{G_z G'_z}^{gra}(\mathbf{q}, 0) = \left(\frac{2\pi}{L}\right)^2 f_{gra}^*(G_z) f_{gra}(G_z - G'_z) G_z G'_z + \frac{1}{L} \chi^{gra}(q, \omega = 0; n_{gra}) f_{gra}(G_z - G'_z) \quad (3.12)$$

Where L is the simulation cell periodicity in the z direction,  $\chi^{2DEG}$  is the Lindhard function of 2DEG and  $\chi^{gra}$  is the polarizability function of graphene [73]. The form factor  $f(G_z)$  describes the distribution of the corresponding wavefunction in the x direction, and it is assumed to have the

form of the Fourier transform of step function:  $f(G_z) = \frac{L}{\pi d} \sin\left(\frac{\pi d G_z}{L}\right) e^{\frac{2\pi i z_0}{L}}$ , where  $d$  is the step width that correspond to an effective layer thickness (obtained by fitting the first-principles  $\chi_{G_z G_z'}(q \rightarrow 0, \omega = 0)$  of individual monolayers) and  $z_0$  is a vertical displacement (which is used to apply a 6.8 Å separation between the layers). This setup allows the calculation of band gap renormalization of ReSe<sub>2</sub>-graphene system as a function the doping density in the graphene and ReSe<sub>2</sub> layer independently. The results with graphene substrate included are presented in Figure 3.8(b), where the doping density of graphene is set to different values. With the inclusion of graphene substrate, the quasiparticle band gap of ReSe<sub>2</sub> monolayer is only reduced by 130 meV within a doping density of 10<sup>12</sup> cm<sup>-2</sup> in ReSe<sub>2</sub>. Furthermore, we find that when any appreciable free-carrier is present in ReSe<sub>2</sub>, the band gap of ReSe<sub>2</sub> becomes insensitive to the charge density in graphene. Although when the ReSe<sub>2</sub> layer remains intrinsic, doping in graphene can renormalize the band gap of ReSe<sub>2</sub> by 50-100 meV.

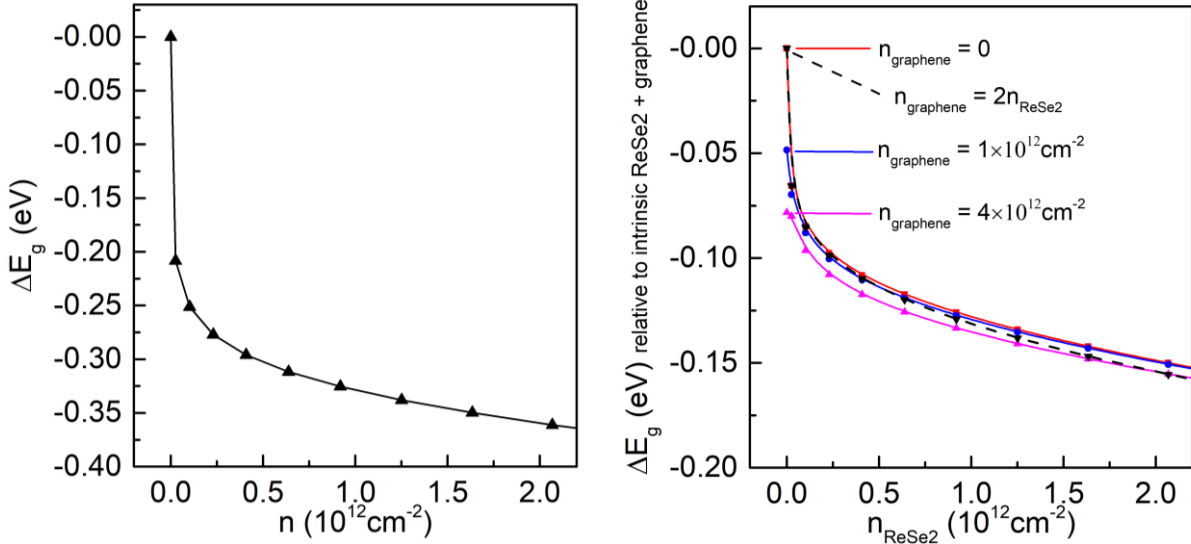


**Figure 3.8** (a) Quasiparticle band gap renormalization of  $n$ -doped free-standing ReSe<sub>2</sub>. (b) Quasiparticle band gap renormalization of  $n$ -doped ReSe<sub>2</sub> on top of graphene substrate. The x-axis is the electron density in ReSe<sub>2</sub> and the different curves correspond to different values of electron density in graphene.

### 3.6 Summary

In summary, we have discussed the band gap renormalization in doped 2D materials within the GW approximation for three prototypical materials. We have combined *ab initio* results and effective mass model to determine the dielectric screening, quasiparticle self-energy and band gap renormalization at arbitrary doping density. With asymptotic analysis, we have shown that the main contribution to the band gap renormalization can be separated into two terms. One is the Coulomb-hole term coming from the change of the dielectric screening, which is highly nonlinear and dominant at low doping density. The other is the screened-exchange term coming from the change in electron occupation, which is linear and more important at high doping density. There were demonstrated in two prototype materials: h-BN and MoS<sub>2</sub>. We have also studied the anisotropic dielectric screening of BP. We find BP has a larger band gap renormalization at high doping density, which we attribute to the smaller density-of-state of BP near the band edge. Finally, using ReSe<sub>2</sub>/graphene heterobilayer as a prototype, we extended this approach to describe the screening effect of a bilayer system with two different materials with lattice mismatch, which would not be possible without the effective mass model.

# **Chapter 4: Dynamical Excitonic Effects in Doped Two-Dimensional Materials**

## **4.1 Introduction**

One of the most prominent features of two-dimensional (2D) materials is the enhanced many-body interactions due to quantum confinement and the reduced electronic screening. This is evident from the significant shift of optical absorption spectra of semi-metallic graphene [74, 75] and the huge exciton binding energies in monolayer transitional metal dichalcogenides (TMDCs) and black phosphorus in an order of a few hundred meV [25, 76-81]. Meanwhile, doping is critical to the proper functioning of electronic and photonic devices. It is widely observed in 2D materials by either inevitable defects or intended electrostatic [9, 82-86] and chemical [48, 49, 87] processes. The doped free carriers make the structure more metallic and impact a wide range of many-body interactions, including quasiparticles (QP), excitons, and higher-order excitations such as trions and biexcitons [47, 83-85]. In particular, the enhanced van Hove singularity (vHS) in reduced-dimensional structures can boost doping effects, evidenced by the huge renormalization of excitonic effects in doped carbon nanotubes [50, 51].

Recent experimental measurements have raised more questions about excitonic effects in doped 2D materials, e.g. settling the discrepancies in excited-state properties as measured under various doping conditions [76, 49]. Unfortunately, limited progress has been made towards this goal. Effective Hamiltonian theories developed for quantum wells can only qualitatively explain the trend of the spectral evolution [88-90], and models of effective static electron-hole (e-h) potential could reproduce the binding energy of small carrier complexes [91-93] but not their doping dependence. The *ab initio* GW+BSE approach [33, 43, 45] has been very successful in predicting

the QP band gaps and optical properties of intrinsic (undoped) 2D materials [25, 79, 80], but it remains elusive how this framework can be extended to excitonic properties in doped 2D materials. It motivates us to further develop this approach to describe the full evolution of optical properties of 2D semiconductors from intrinsic to heavily-doped cases.

In this chapter, we have developed a generalized plasmon-pole (GPP) model for capturing the essential dynamical screening, making it possible to efficiently calculate the excitonic properties (energies and oscillator strength) in doped 2D systems. With this methodological advancement, we focus on monolayer MoS<sub>2</sub>, a prototypical 2D semiconductor of broad interest, on which spectrum resolution of a few meV have been achieved experimentally recently [94]. We reveal the importance of including dynamical effects for describing the effective screened interaction within the e-h pairs in the presence of extra charge carriers. The calculation shows good agreement with experiments in the evolution of the bright exciton energy according to the doping density, while it also raises questions of interpretations of the observed exciton energy spectrum.

Doping can impact excitonic effects and optical spectra through several mechanisms, as shown in the schematic diagram in Figure 4.1. First, within the single-particle picture, the Pauli blocking effect (Burstein-Moss shift [95, 96]) of doped carriers raises the e-h continuum energy ( $E_{\text{cont}}$ ) relative to the band gap linearly, due to the constant 2D density of states. More importantly, reduced-dimensional systems are susceptible to the changes of electronic screening, which can result in large renormalization in the excited state properties [97-99]. On one hand, screening from the doped free carriers can induce a large nonlinear QP band gap renormalization (BGR) due to the carrier plasmon [52], and result in negative electronic compressibility [53, 100, 101]. On the other hand, screening results in the reduction of exciton binding energy, which is the center of our discussion. Interestingly, experimental measurements show that the energy of

the neutral exciton stays nearly constant in various doping conditions, with a small and linear blue shift roughly following the Fermi energy [47, 83-86], suggesting a nearly exact cancellation between the change in QP band gap and exciton binding energy. As we will see, this cancellation cannot be trivially reproduced from the widely used static BSE; dynamical corrections, arising from the strong correlation effects of doped carriers, need to be treated carefully.

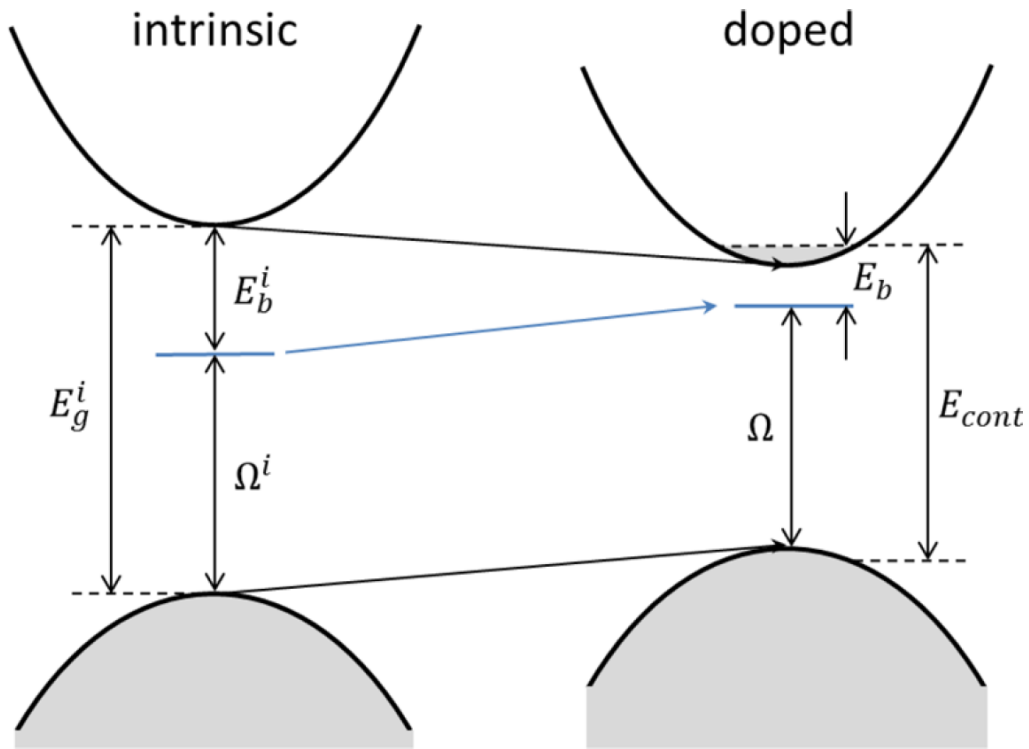


**Figure 4.1** Schematic diagram showing the doping effects, including a reduction of QP band gap  $E_g$ , a reduction of exciton binding energy  $E_b$ , and a rise of e-h continuum energy  $E_{cont}$  relative to the band gap due to Pauli blocking. Changes in the exciton energy  $\Omega$  is a combination of these effects.

## 4.2 Dynamical Effects in Bethe-Salpeter Equation

The widely used GW+BSE approach starts with the  $G_0W_0$  approximation to the QP self-energy,

where the (inverse) dielectric function  $\epsilon_{GG'}^{-1}(\mathbf{q}, \omega)$  and the screened Coulomb interaction

$W_{GG'}^{-1}(\mathbf{q}, \omega) = \epsilon_{GG'}^{-1}(\mathbf{q}, \omega)v(\mathbf{q} + \mathbf{G}')$  is constructed from the random-phase approximation

(RPA). Beyond single-particle excitation, for studying excitonic effects, the BSE can be formulated as a generalized eigenvalue problem:

$$(E_{ck} - E_{vk})A_{vck}^S + \sum_{v'c'k'} K_{vck,v'c'k'}(\Omega^S)A_{v'c'k'}^S = \Omega^S A_{vck}^S \quad (4.1)$$

where the correlate e-h excitation  $S$  of energy  $\Omega^S$  is expanded on the basis of e-h pairs  $|S\rangle = \sum A_{vck}^S |vck\rangle$ , and  $v$  and  $c$  stand for the valence and conduction band index, respectively. Here we have restricted our discussion within the e-h excitations under the Tamm-Dancoff approximation [45].

The e-h interaction kernel  $K$  is dominated by the attractive direct term

$$K_{vck,v'c'k'}^d(\Omega^S) = -\sum_{\mathbf{G}\mathbf{G}'} M_{c'c}^*(\mathbf{k}, \mathbf{q}, \mathbf{G}) M_{v'v}(\mathbf{k}, \mathbf{q}, \mathbf{G}') \tilde{\epsilon}_{\mathbf{G}\mathbf{G}';cvc'v'k}^{-1}(\mathbf{q}, \Omega^S) v(\mathbf{q} + \mathbf{G}') \quad (4.2)$$

Where  $\mathbf{q} = \mathbf{k}' - \mathbf{k}$  and  $M_{n'n}(\mathbf{k}, \mathbf{q}, \mathbf{G})$  is the plane-wave matrix element containing the band structure information [44]. The dynamical effects are incorporated into the effective dielectric function, which is given by (neglecting finite lifetime effects) [50, 51, 102, 103]:

$$\tilde{\epsilon}_{\mathbf{G}\mathbf{G}';cvc'v'k}^{-1}(\mathbf{q}, \Omega^S) = \epsilon_{\mathbf{G}\mathbf{G}'}^{-1}(\mathbf{q}, 0) - \frac{1}{\pi} P \int_0^\infty d\omega \operatorname{Im} \epsilon_{\mathbf{G}\mathbf{G}'}^{-1}(\mathbf{q}, \omega) \left[ \frac{2}{\omega} + \frac{1}{\Omega^S - \omega - (E_{c\mathbf{k}+\mathbf{q}} - E_{v'\mathbf{k}})} + \frac{1}{\Omega^S - \omega - (E_{c'\mathbf{k}} - E_{v\mathbf{k}+\mathbf{q}})} \right] \quad (4.3)$$

The static approximation for BSE, which neglects the last term in this equation, is commonly used for intrinsic semiconductors and typically reproduces the excitonic properties accurately because the differences  $\Omega^S - (E_c - E_v)$  can be neglected in comparison to the characteristic energy of the loss function  $\epsilon_{\mathbf{G}\mathbf{G}'}^{-1}(\mathbf{q}, \omega)$  (the plasmon energy) [45].

However, the approach described above cannot fully capture the excitonic effects when doping is introduced, due to the following reasons. First, the acoustic carrier plasmon in the 2D electron gas (2DEG), which falls on a similar energy-scale as that of the exciton binding energy, dynamically couples with QP and e-h excitations [104-106]. This corresponds to a characteristic dynamical screening time similar as the e-h scattering time, which invalidates the static screening approximation. Second, beyond excitons, the success in describing the trion binding energy in doped monolayer TMDCs by an effective pairwise interaction of intrinsic systems [91, 92] irrespective of the doping density, contradicts the simple picture of static free-carrier screening. It has been suggested that dynamical correlations of excitons could explain this puzzle [107, 108]. Third, the correlation effects naturally grow stronger in the low doping limit as the interaction energy of electrons dominates over the kinetic energy [61], making vertex corrections beyond RPA more important in the screening process. To date, the importance of dynamical effects has been noted in bulk noble metals [109] and doped semiconducting carbon nanotubes [50, 51], but has never been studied in 2D materials.

The BSE is hardly solvable with the dynamical effects in the form of Eq. (4.3), but it can be greatly simplified if we make a plasmon-pole approximation (PPA) to the dielectric function.

Assuming there is only a single plasmon-pole

$$\epsilon_{GG'}^{-1}(\mathbf{q}, \omega) = \delta_{GG'} + \frac{A_{GG'}(\mathbf{q})}{\pi} \times \left[ \frac{1}{\omega - \tilde{\omega}_{GG'}(\mathbf{q}) + i0^+} - \frac{1}{\omega + \tilde{\omega}_{GG'}(\mathbf{q}) + i0^+} \right] \quad (4.4)$$

Eq. (4.3) can be simplified into

$$\tilde{\epsilon}_{GG'}^{-1}(\mathbf{q}, E_{\text{int}}^S) = \epsilon_{GG'}^{-1}(\mathbf{q}, 0) - \frac{2}{\pi} A_{GG'}(\mathbf{q}) \frac{E_{\text{int}}^S}{\tilde{\omega}_{GG'}(\mathbf{q})(\tilde{\omega}_{GG'}(\mathbf{q}) + E_{\text{int}}^S)} \quad (4.5)$$



where  $\tilde{\omega}_{GG'}(\mathbf{q})$  and  $A_{GG'}(\mathbf{q})$  are the frequency and amplitude of the pole, respectively. Here we have also approximated the terms on the denominator of Eq. (4.3) by  $(E_{ck+q} - E_{v'k}) - \Omega^S \approx (E_{c'k} - E_{vk+q}) - \Omega^S \approx E_{int}^S$ , where  $E_{int}^S = \sum (E_{ck} - E_{vk}) |A_{vck}|^2 - \Omega^S$  is the average e-h interaction energy, which approximately equals to the binding energy  $E_b^S = E_{cont} - \Omega^S$  for tightly bound states. It becomes clear from Eq. (4.5) that the dynamical effect serves as a positive correction to the static dielectric function (with  $A_{GG'}(\mathbf{q})$  being negative by the way it is defined) and weakens the screening to the e-h interaction compared with the static approximation. The BSE can now be solved self-consistently as a generalized eigenvalue problem with only a few self-consistent steps additional to the regular problem, if we are interested in a few optically active excitonic states which typically dominate the optical spectra.

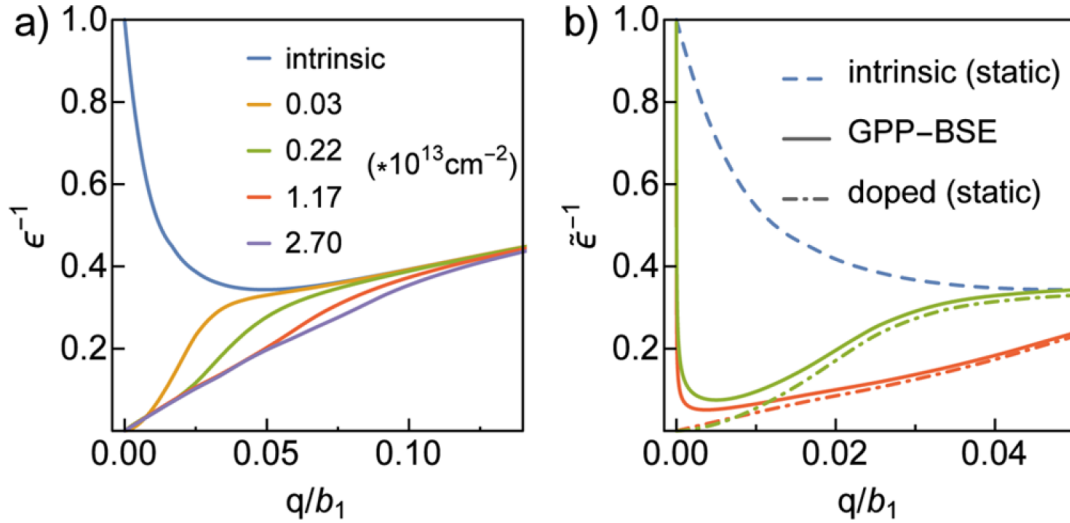


**Figure 4.2** (a) The RPA static dielectric function at different doping densities. (b) The effective dielectric function  $\tilde{\epsilon}_{00}^{-1}(\mathbf{q}, E_b)$  from GPP-BSE for the primary excitonic state compared with intrinsic and doped static dielectric functions  $\epsilon_{00}^{-1}(\mathbf{q}, 0)$ . Doping densities of  $0.03 \times 10^{13} \text{ cm}^{-2}$  (green) and  $0.60 \times 10^{13} \text{ cm}^{-2}$  (red) are shown.

Due to the elusive nature of vertex corrections beyond RPA, we employ the single-pole Hybertsen-Louie GPP approximation [43] to the dielectric function in calculating e-h

interactions, which preserves the generalized f-sum rule, an exact constraint to the dielectric function to all orders in the diagrammatic expansion, thus including correlation effects beyond RPA [110]. We will call this approximation the GPP-BSE approximation, as opposed to the commonly used static BSE (S-BSE) approximation.

With the GPP-BSE approximation, the head part of the effective dielectric function is simplified to be

$$\tilde{\epsilon}_{00}^{-1}(\mathbf{q}, E_{\text{int}}^S) = \epsilon_{00}^{-1}(\mathbf{q}, 0) + \frac{E_{\text{int}}^S [1 - \epsilon_{00}^{-1}(\mathbf{q}, 0)]^{3/2}}{\omega_p(q) + E_{\text{int}}^S \sqrt{1 - \epsilon_{00}^{-1}(\mathbf{q}, 0)}} \quad (4.6)$$

where  $\omega_p(q) \approx \sqrt{2\pi n_{2D} q}$  is the 2D plasma frequency and  $n_{2D}$  is the total (intrinsic + doped) 2D charge density. Contributions from the parts with nonzero G-vector are small enough to be neglected [52]. The static dielectric function  $\epsilon_{00}^{-1}(\mathbf{q}, 0)$  of the intrinsic system, shown in Fig. 4.2(a) for monolayer MoS<sub>2</sub>, approaches 1 as  $q \rightarrow 0$ , signifying the vanishing long-range screening effects in 2D systems, whereas it drops to 0 in the doped system, signifying the metallic screening. After including dynamical effects, however, the effective dielectric function of the doped system, shown in Fig. 4.2(b), diverts from its static value and rises sharply to 1 as  $q \rightarrow 0$ . It results from the 2D plasmon dispersion where plasmon energy vanishes as  $q \rightarrow 0$ , which delineates the frequency-range within which the doped carriers can respond. The consequence is a reduced effective screening as the carriers are unable to catch up with the dynamics of the e-h pair.

### 4.3 Calculation Details and Comparison of Different Approximations

The calculation is conducted on n-doped monolayer MoS<sub>2</sub> as a prototypical example, with the procedure described as follows. The DFT calculations were conducted using a plane-wave basis with a 70 Ry energy cutoff with norm-conserving pseudopotentials including the semi-core states of Mo, and GGA-PBE [58] type of exchange-correlation functional, using the QuantumESPRESSO package [39]. Rigid-band doping is used to mimic electrostatic doping.

The QP band gap is determined using the G<sub>0</sub>W<sub>0</sub> approximation with the same GPP approximation to the frequency-dependence of the dielectric function. The dielectric matrix is calculated on a 36×36×1 k-grid with a summation of N<sub>c</sub>=256 empty bands and a cutoff of 10 Ry. The same number of bands are used in the summation of the self-energy with the static remainder approximation to accelerate convergence [111]. A truncation to the Coulomb interaction [59] is applied to eliminate interactions between periodic images. For the doped system, k-grid up to 48×48×1 for the dielectric matrix is used to calculate BGR. The BSE is solved on a finer 120×120×1 k-grid in order to capture the phase-space blocking effect. To construct the e-h interaction kernel, the head part of the dielectric matrix  $\epsilon_{00}^{-1}(\mathbf{q}, 0)$  with small q is calculated directly on this finer k-grid to capture its rapid variation near q=0 [28], and interpolated from a 24×24×1 coarse grid elsewhere. A spin-orbit splitting of  $\Delta_{SO}=160$  meV, which is not affected by the GW corrections [112], has been included as a rigid shift to the exciton energy. The BerkeleyGW [44] package is used for these calculations.

For the GPP-BSE calculation, which is not part of the BerkeleyGW package, the head part of the dielectric function is read out from the program, modified according to Eq. (4.6) into  $\tilde{\epsilon}_{00}^{-1}(\mathbf{q}, E^{in})$  with a series of different input values  $E^{in}$ , and then put back in to solve for the BSE matrix. The

e-h interaction energy  $E_{int}^S$  of each low-lying exciton eigenstates S is then calculated and plotted against  $E^{in}$  to find the solution that satisfy the self-consistency condition  $E_{int}^S = E^{in}$ , as illustrated in Figure 4.3. Note that the self-consistency condition breaks the orthogonality between different eigenstates. However, the low-lying exciton eigenstates (1s, 2s, etc.) are well separated from each other in energy and thus well-defined solutions still exist.

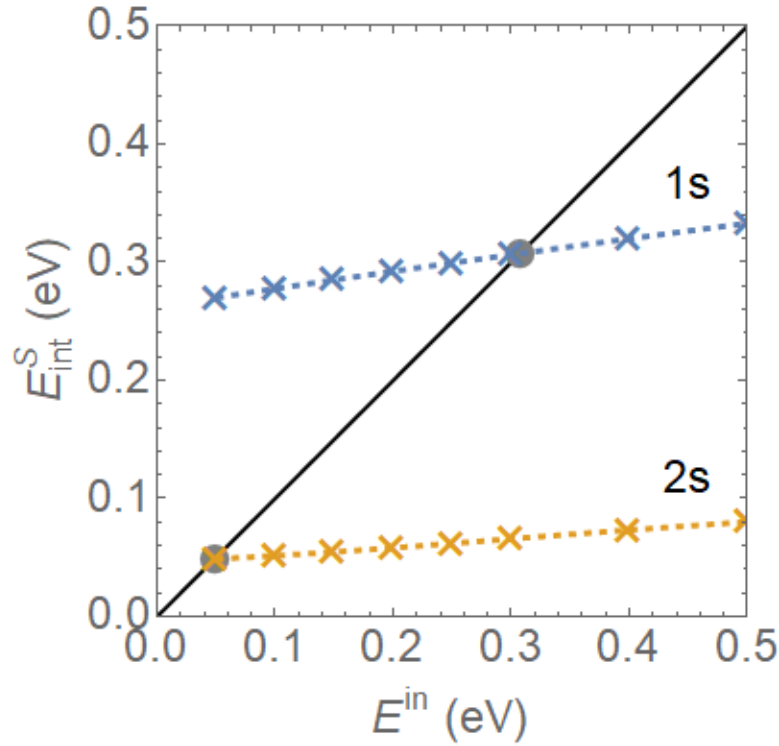


**Figure 4.3** The self-consistent solution of BSE using the effective dielectric function Eq. (4.6)

for the 1s and 2s exciton states at doping density  $0.3 \times 10^{12} \text{cm}^{-2}$ .

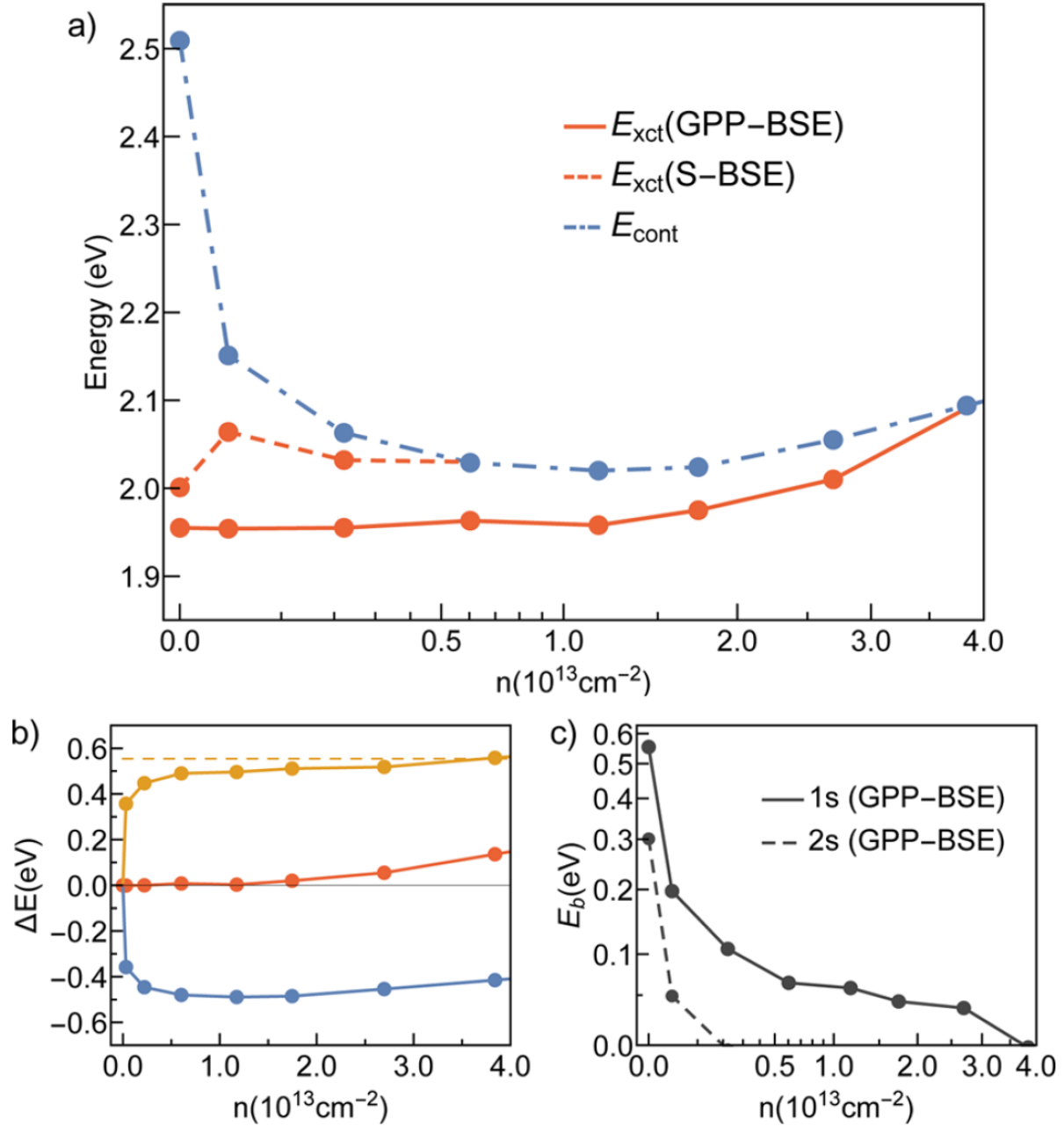


**Figure 4.4** (a) The energy of the band continuum edge and exciton as a function of the doping density from S-BSE and GPP-BSE. (b) Cancellation between BGR ( $\Delta E_{\text{cont}}$ , lower curve) and exciton binding energy reduction ( $-\Delta E_b$ , upper curve) that determines the change in exciton energy in GPP-BSE. Dashed line corresponds to the complete vanishing of exciton binding energy. (c) Binding energy of the 1s and 2s excitonic states as a function of the doping density from GPP-BSE.

Figure 4.4 summarizes the resulting energy of the primary exciton state of n-doped monolayer MoS<sub>2</sub> versus the doping density  $n$ , calculated from the GPP-BSE and S-BSE approximation. Fig. 4.4(a) shows the evolution of e-h continuum and exciton energy. The most striking feature is that the exciton energy within the GPP-BSE approximation is nearly flat at low doping densities and slightly increases at higher doping densities. This nearly fixed exciton energy at the low doping density comes from an almost exact cancellation between the nonlinear BGR and exciton binding energy reduction, as shown in Fig. 4.4(b). For higher doping densities, the reduction of the exciton binding energy is nearly saturated while the e-h continuum energy still increases linearly due to Pauli blocking. Thus, the exciton energy also increases linearly.

In comparison, the exciton energy calculated from S-BSE shows a wiggling blueshift at low doping densities, as shown in Fig. 4.4(a). This difference shows that the overestimation of screening from the static e-h interaction kernel, as seen by comparing the static versus effective dielectric function in Fig. 4.2(b), is indeed important in doped systems.

It is worth noting that dynamical effects also reduce the exciton binding energy of intrinsic monolayer MoS<sub>2</sub> by 40 meV, which quantifies the margin of error expected from the common static approximation in intrinsic 2D semiconductors. It also needs to be noted that the electron-phonon interaction is neglected in our calculation, which may introduce an extra variation of optical properties [113]. However, phonon modes will not be abruptly changed by doping in MoS<sub>2</sub> [114]. Accordingly, we expect the electron-phonon coupling does not significantly change our results.

The cancellation between quasiparticle band gap and exciton binding energy at the low energy limit can be understood theoretically as the following. If static approximation is used in both GW

and BSE, the dominant term in GW approximation, following the discussion in Chapter 3, would be the static Coulomb-hole self-energy (i.e. Eq. (3.7) with the plasmon frequency  $\omega_d(\mathbf{q}) \rightarrow \infty$ ):

$$|\Delta\Sigma_{\text{static}}^{CH}| \sim \frac{1}{2} \int \frac{d^2\mathbf{q}}{(2\pi)^2} |\delta\epsilon_{\mathbf{00}}^{-1}(\mathbf{q}, 0)| v(\mathbf{q}) \quad (4.7)$$

which take equal but opposite value for VBM and CBM. The reduction in the band gap in static approximation is therefore just  $2|\Delta\Sigma_{\text{static}}^{CH}|$ . Meanwhile, the correction to the exciton energy under first-order perturbation is

$$\Delta\Omega^S \sim \sum_{\mathbf{k}, \mathbf{q}} A_{\mathbf{k}+\mathbf{q}}^* A_{\mathbf{k}} \langle \mathbf{k} | \delta\epsilon_{\mathbf{00}}^{-1}(\mathbf{q}, 0) v(\mathbf{q}) | \mathbf{k} + \mathbf{q} \rangle \quad (4.8)$$

which, in the low-density limit where  $k_F$  is much smaller than the extension of exciton wavefunction in k-space, reduces to  $\Delta\Omega^S \sim - \int \frac{d^2\mathbf{q}}{(2\pi)^2} |\delta\epsilon_{\mathbf{00}}^{-1}(\mathbf{q}, 0)| v(\mathbf{q})$ , exactly cancelling the band gap renormalization.

However, the static approximation grossly overestimates the GW correction to the band gap, and the inclusion of dynamical effect within GPP, which produces much more accurate band gap value, effectively adds a quasiparticle renormalization factor  $Z \equiv 1/(1 - \frac{\partial\Sigma(E)}{\partial E})$  to the static self-energy:  $\Delta E^{QP} \approx Z \cdot \Delta\Sigma_{\text{static}}$ . For example, for the VBM and CBM of MoS<sub>2</sub>,  $Z \approx 0.8$ . Therefore, using S-BSE with a GW band gap obtained from the GPP model (or any model that includes dynamical effect, including what we used in Chapter 3) causes red shift in the exciton energy. By including the dynamical effects under the same level of approximation (GPP), we effectively reduce  $\Delta\Omega^S$  by a fraction that is close to  $Z$ , thereby recovering the cancellation between the two and at the same time producing a much more accurate band gap value compared with the static approximation.

It is important to point out that a tentative alternative form of PPA may be the low-energy acoustic plasmon of the doped carrier that matches the full-frequency RPA. The effective dielectric function within such PPA takes the following form [50, 51]:

$$\tilde{\epsilon}_{00}^{-1}(\mathbf{q}, E_{int}^S) \approx \epsilon_{00}^{-1}(\mathbf{q}, 0) + \frac{E_{int}^S}{E_{int}^S + \omega_{ap}(q)} [\epsilon_{i,00}^{-1}(\mathbf{q}, 0) - \epsilon_{00}^{-1}(\mathbf{q}, 0)] \quad (4.7)$$

where  $\omega_{ap}(q)$  the frequency of the low-energy acoustic plasmon of the doped carriers obtained within RPA, and  $\epsilon_{i,00}^{-1}(\mathbf{q}, 0)$  is the static dielectric function of the intrinsic system. Figure 4.5 shows the exciton energies obtained from this approximation. The exciton effectively feels almost no screening from the doped carrier and the binding energy only slowly and linearly decrease upon doping, because the energy of this plasmon  $\omega_{ap}(q)$  is well below the e-h interaction energy for small  $q$ . The band gap, on the other hand, still drops rapidly as doping is first introduced [52], so the combined effect leads to a quick drop of exciton energy of around 300 meV at light doping, until BGR saturates and binding energy reduction and Pauli-blocking effect takes over as doping density increases. This rapid variation of exciton energy with doping contradicts the basic experimental observations, and we believe the discrepancy originates from vertex corrections which are generally more important at lower free carrier density. The GPP-BSE approximation, on the other hand, approximately take into account these vertex corrections, and cures the large discrepancy produced by RPA dynamical screening. Note that the GPP approximations here is validated *a posteriori* through comparison with experiment, and its disagreement with the full-frequency RPA in both GW [115] and BSE should not be regarded as a drawback of GPP, but rather an indication of the importance of vertex corrections.



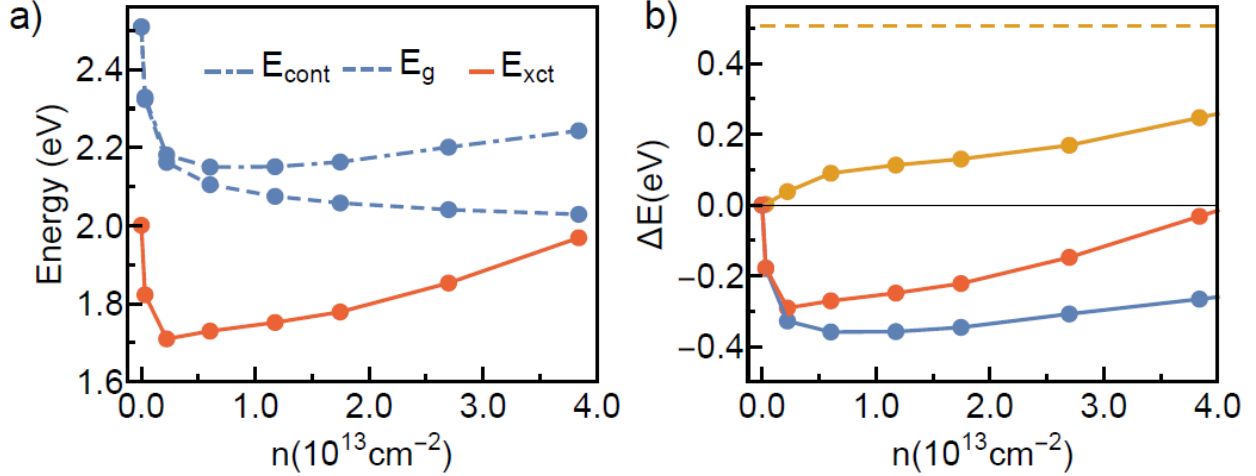


**Figure 4.5** Same as Figure 4.3(a)(b) but using the low energy acoustic plasmon from RPA as pole.

## 4.4 Excitonic Spectrum and Absorption Lineshape

Excitonic effects are also generally more robust when dynamical effects are included. For example, as marked in Fig. 4.4(a), in S-BSE the exciton merges into the e-h continuum and dissociates before the doping density reaches  $0.6 \times 10^{13} \text{ cm}^{-2}$ , while in the GPP-BSE it survives until the doping density reaches  $4 \times 10^{13} \text{ cm}^{-2}$ . Considering the screening from the dielectric environment that could further reduce exciton binding [98, 99], such a density ( $4 \times 10^{13} \text{ cm}^{-2}$ ) is expected to be the upper limit for exciton dissociation in experiments.

Interestingly, the exciton energy spectrum does not scale linearly with the doping density. The 2s exciton state is far more sensitive to the doping level, as shown in comparison to the 1s state in Fig. 4.4(c). It quickly vanishes when the doping density reaches around  $10^{12} \text{ cm}^{-2}$ , leaving the 1s state as the only bound excitonic state. This is because a weaker bound state has slower dynamics and thus allows more time for the carrier screening to catch up, and consequently feels a stronger effective screening, as given by Eq. (4.6). As a result, we find the higher quantum-number excitonic states are more unstable against doping than the primary 1s state. This is

different from a recently reported experimental finding in  $\text{WS}_2$  [86], in which the higher excitonic states would survive large doping densities. We speculate from their extremely small amplitude that the experimental 2s and 3s states may be pinned to defects, although more works are needed to settle this discrepancy definitively.

In Fig. 4.6, the change of exciton energy and oscillator strength relative to the intrinsic system in our calculation are directly compared to experiments on doped monolayer  $\text{MoS}_2$  and  $\text{WS}_2$ . The GPP-BSE approximation achieves remarkable agreement with experiment in exciton energy within our numerical accuracy, while the e-h binding energy have changed a few hundred meV. It also reproduces the oscillator strength of exciton better than the S-BSE approach, although there's a small disagreement at large doping density, which may emerge from the many-body effects beyond GPP such as the coupling with trions.

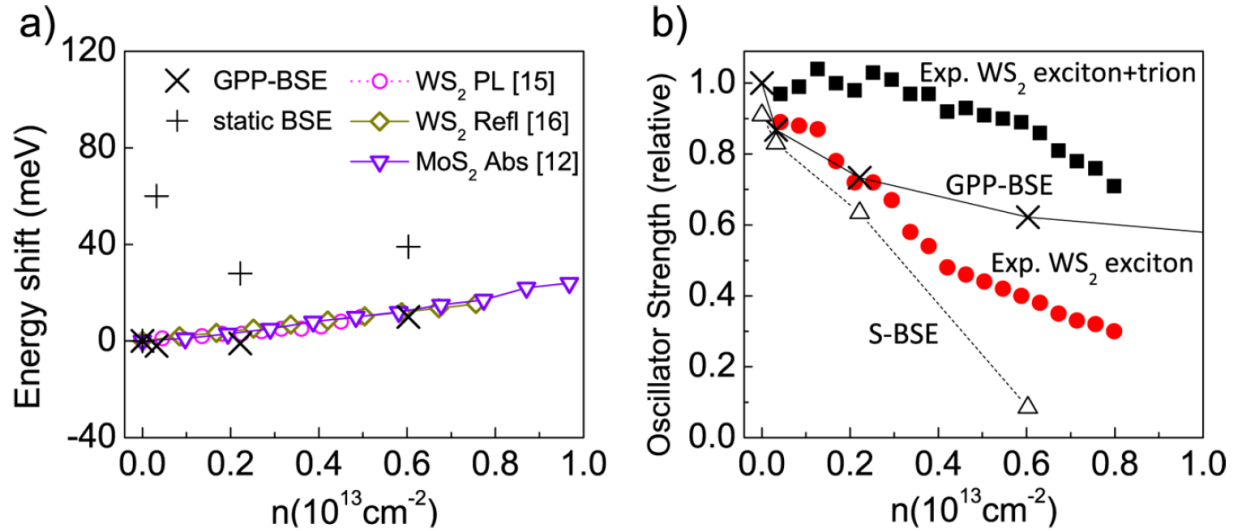


**Figure 4.6** (a) Exciton energy shift from different approximation compared with experiments [47, 83, 86].  
(b) Exciton oscillator strength change from different approximations compared with  $\text{WS}_2$  reflectance contrast spectra experiment [86].

As experimentally observed in the optical spectra of quasi-2D semiconducting quantum wells [116-119] and monolayer TMDCs [47, 83-86], when the doping density increases, spectrum weights are first transferred from exciton to trion, and then the exciton and trion peak in the spectrum merge into an asymmetric line shape called the Fermi-edge singularity (FES). This transition from discrete bound states to FES has been studied in model systems for quantum wells [88-90, 120]. As is shown in Fig. 4.7, the spectra obtained from the GPP-BSE approximation are in stark contrast with the ones obtained from the S-BSE. Apart from the aforementioned exciton energy levels, the spectra differ markedly in their absorption edges as they evolve from discrete symmetric excitonic peaks to continuous asymmetric FES. At high doping densities, the S-BSE predicts a complete absence of excitonic effects, as its absorption line merges with the single-particle prediction. However, in the GPP-BSE a broad FES is retained at higher doping densities, because the important dynamical many-electron response is rectified by our effective dielectric model. Fig. 4.7 also shows how the real-space exciton wavefunction evolves with doping. As the doping density increases, apart from a slightly wider spread due to weaker binding, an Airy-type pattern also emerges due to the Pauli blocking in  $k$ -space.

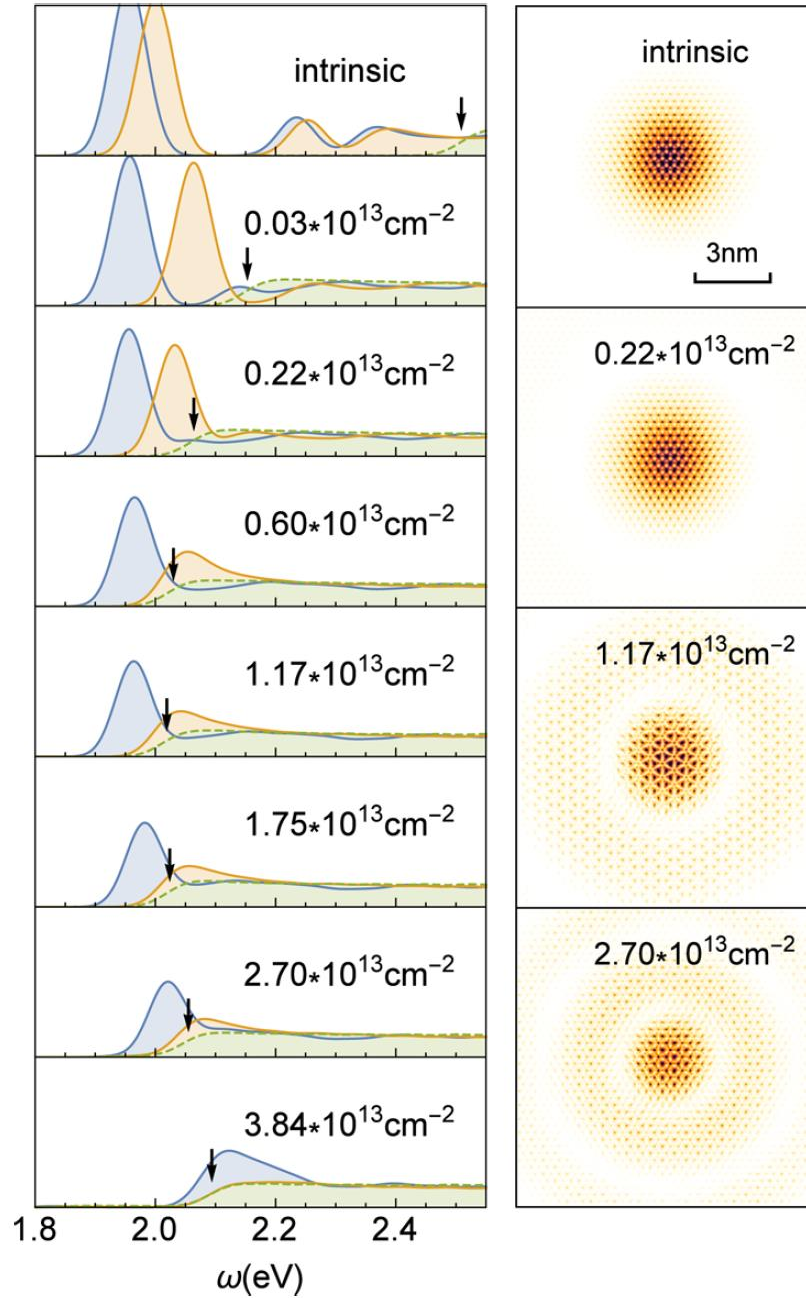


**Figure 4.7** (left) The evolution of absorption line shape with doping calculated from S-BSE (yellow) and GPP-BSE (blue). The dashed line represents the absorption calculated without e-h interaction. The arrows donate the e-h continuum energies. A 0.03 eV Gaussian broadening is applied to the spectrum. (right) Modulus squared real-space wave function of the primary exciton state from solving GPP-BSE. It is plotted as a function of electron position with the hole fixed at the center and is integrated out along the off-plane z-direction.

Finally, we have to address that, in the GPP-BSE approximation, the dynamical effects are treated equally in GW and BSE, which also improves the cancellation between QP self-energy and excitonic correction [109, 121]. It should be noted that the GPP-BSE is only a crude approximation to the complicated dynamical response of the many-body system, where more higher-order vertex corrections come into play at lower doping densities, as the dimensionless Wigner-Seitz radius  $r_s$  increases with decreasing density. On the other hand, as the doping density increases, the effects of vertex corrections are lessened, and RPA becomes a better approximation, and consistently the difference between GPP-BSE and S-BSE becomes smaller. Graphene, on the other hand, has a constant  $r_s$  due to its linear dispersion [73], which suggests that the vertex corrections to its dielectric response are small for all doping density. And indeed, static BSE has been able to capture the optical response of doped graphene [122, 123].

In conclusion, we have shown that the inclusion of dynamical excitonic effects and beyond-RPA screening in BSE is crucial for correctly studying the optical properties of doped 2D semiconductors. We have developed the sum-rule-preserving GPP-BSE approximation to these effects, which produces good agreement with experiments. Our result, in particular the evolution of exciton binding energy, is important for interpreting experimental measurements and quantitatively understanding and predicting the doping effects in 2D semiconductors. Moreover, our method paves the way of understanding electronic structures of doped 2D devices and further studies on charged excitations, such as trions, in doped materials.

# **Chapter 5: Interlayer Coupling and Gate-Tunable Excitons in Transition Metal Dichalcogenide Heterostructures**

## **5.1 Introduction**

Two-dimensional (2D) transition metal dichalcogenides (TMDC) and its heterostructures have attracted a lot of attentions recently as a promising candidate for photonics, optoelectronics, and valleytronics devices [8, 10]. With the type II band alignment, TMDC bilayer heterostructures possess ultrafast charge transfer and long-lived interlayer exciton as its lowest-energy optical excitation, which is desirable for light harvesting applications [124-126], as well as realizing high-temperature excitonic superfluidity [20]. In particular, because the interlayer charge transfer and exciton photoemission in these structures depends critically on the interlayer coupling [127-130] and the widely-used gate field can efficiently tune the band offset and interlayer interactions, the range of tunable optoelectronic properties of these heterostructures may be substantially enhanced over that of semiconductor quantum wells [131].

The first-principle DFT + GW/BSE method has been very successful in studying and predicting excited-state properties of 2D structures. However, previous calculations have only studied the band structure and excitonic properties of intrinsic TMDC heterostructures [132-134]. In these calculations, the role of interlayer coupling is not yet well addressed. Particularly, how the external gate field impacts the interlayer coupling and interlayer excitations is largely unknown. In this sense, it is essential to have a reliable study that can capture this interlayer coupling and excitons and how those electron-hole pairs and optical response are tuned by the external gate field.

In this chapter, we study gated MoS<sub>2</sub>/WS<sub>2</sub> and MoSe<sub>2</sub>/WSe<sub>2</sub> heterostructures with first-principles DFT + GW/BSE calculations. We first study the band structure and interlayer coupling at the DFT level. Then we construct a simple model that accounts for the interlayer coupling and provides accurate results for the low-energy excitation spectrum both at the single-particle level and including electron-hole interactions. The model is benchmarked against the first-principles results without spin-orbit coupling (SOC) first, and then SOC is added as a perturbation. This approach allows us to predict the energy, dipole strength, and radiative lifetime of the excitons under arbitrary external field, with input parameters obtained from the first-principle results. As we will show, apart from the obvious linear response of the band alignment to the external field, the interlayer coupling between the valence bands of the bilayer leads to anti-crossing behavior of the lowest energy excitons, changing its nature continuously from interlayer to intralayer. Our result reveals the nature of the excitons in TMDC heterostructures and explains their gate tunability, which will help to interpret and predict experimental optical measurement.

## **5.2 Interlayer Coupling at the Single-Particle Level**

In the following, we use MoS<sub>2</sub>/WS<sub>2</sub> as the primary example. Figure 5.1 shows a simple schematic picture of the band alignment MoS<sub>2</sub>/WS<sub>2</sub> bilayer heterostructure based on our calculation. The conduction band minimum (CBM) and valence band maximum (VBM) belongs to MoS<sub>2</sub> and WS<sub>2</sub> respectively, forming a type II band alignment. SOC further splits the spin-up and spin-down bands. Finally, due to the band alignment, the lowest optical transition (exciton) is interlayer, while the intralayer transitions lays higher up in energy. To further quantify this picture, we turn to the first-principles calculation, beginning with the DFT picture.

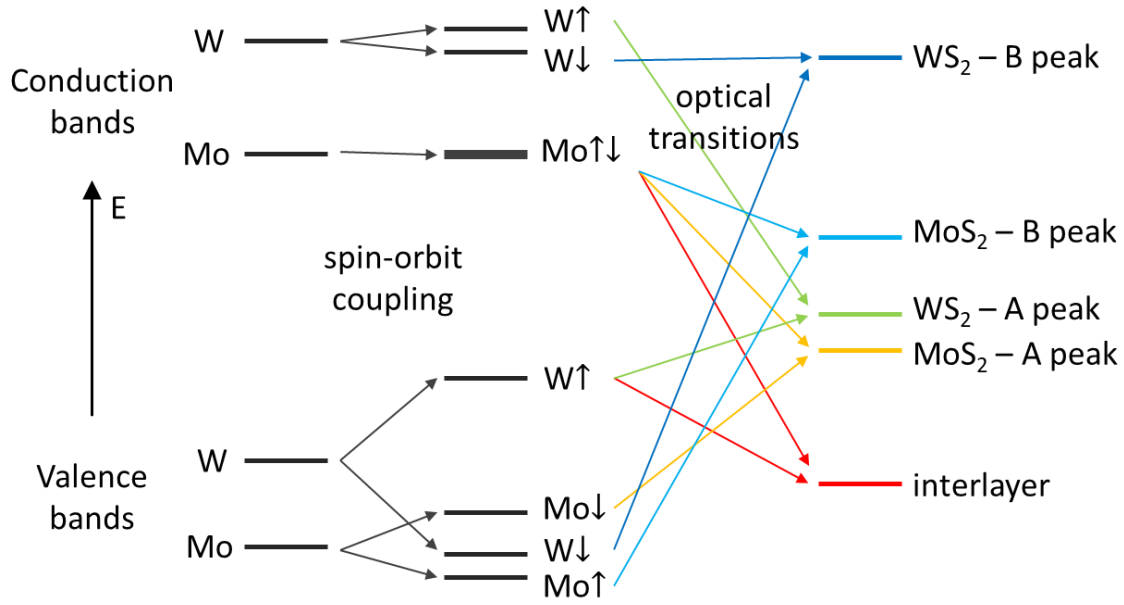


**Figure 5.1** Schematic energy level diagram of MoS<sub>2</sub>/WS<sub>2</sub> heterostructure showing its relative band alignment and related optical transitions without the interlayer coupling (not to scale).

The DFT calculation is done with plane-wave pseudopotential method implemented in Quantum Espresso [39], using the PBE exchange-correlation functional [58] and including the semi-core states of Mo and W. The plane-wave cutoff is chosen to be 75 Ry to ensure the converged results. The structure is relaxed with the van der Waals (vdW) DFT-D2 functional [135, 136]. A vacuum of at least 15 Å is added in the vertical direction to avoid spurious interactions between adjacent slabs. We adopt the stable AB-stacking configuration between the two layers, which can be achieved experimentally by epitaxial growth [137]. The interlayer coupling strength may change with a different stacking configuration or twisting angle [138], but the physical picture and the model we are about to present remains the same. The relaxed lattice constant and interlayer distance (vertical distance from Mo to W) is 3.18 Å and 6.21 Å for MoS<sub>2</sub>/WS<sub>2</sub>, and 3.32 Å and 6.54 Å for MoSe<sub>2</sub>/WSe<sub>2</sub>, which agrees with previous calculations [139, 140]. (The lattice mismatch between the two layers is less than 0.5 %, which will not significantly affect the



calculated results.) A saw-tooth like potential in the vertical direction is used to simulate the external gating field along with the dipole correction. The positive direction of the external field is defined as pointing from the MoS<sub>2</sub> layer towards the WS<sub>2</sub> layer (see Figure 5.2(b)). While a gate field usually leads to charging of the material, electrostatic doping effects [50-52, 141] can be avoided in experimental set-ups where the sample is not directly contacted by metal electrodes.

Figure 5.2(a) shows the DFT band structure of MoS<sub>2</sub>/WS<sub>2</sub> without external field, with the color indicating the projection of the wavefunction onto either layer. To simplify the problem, SOC is not included here for the sake of argument, but will be included later in the final result. As expected, the DFT result confirms the Type II band alignment, where the VBM at the K point is in the WS<sub>2</sub> layer and the CBM is at the  $\Gamma$  point in the MoS<sub>2</sub> layer. However, the projection of the electronic wavefunction shows that the VBM wavefunction is not 100% WS<sub>2</sub>, but rather have a layer projection of 90% WS<sub>2</sub> and 10% MoS<sub>2</sub>, indicating the presence of interlayer coupling. This is more evident by looking at how the VBM and CBM energy changes in response to a vertical electric field, as indicated by dots in Figure 5.2(c). Because of the interlayer coupling, the two bands at VBM shows anti-crossing behavior as the electric field reverses their order. In contrast to this, due to the lack of interlayer interaction, the two bands at CBM pass through each other.

This coupling behavior can be described by a simple model of a  $2 \times 2$  matrix  $\begin{pmatrix} \varepsilon_{Mo} & t \\ t & \varepsilon_W \end{pmatrix}$ , where  $\varepsilon_{Mo}$  and  $\varepsilon_W$  are the energy of the VBM of each layer alone. Under external electric field  $E$ , the relative band alignment of the two layers responds as  $\varepsilon_{Mo}(E) - \varepsilon_W(E) = \varepsilon_{Mo}(0) - \varepsilon_W(0) - eEd/\epsilon$ , where  $d$  is the interlayer separation and the parameter  $\epsilon$  reflects the material's screening response to the vertical electric field. For the MoS<sub>2</sub>/WS<sub>2</sub> bilayer we find  $\epsilon = 6.5$  by fitting the

VBM energy, in close agreement with the fully *ab initio* calculated vertical dielectric constant MoS<sub>2</sub> (6.3) and WS<sub>2</sub> (6) [142]. The same value for  $\epsilon$  also describes the response of CBM energy to the electric field, where the coupling is negligible. With a value of  $t = 45 \text{ meV}$  for the parameter describing the interlayer coupling strength at the VBM, this simple model perfectly describes the first-principles result as demonstrated in Fig. 5.2(c).

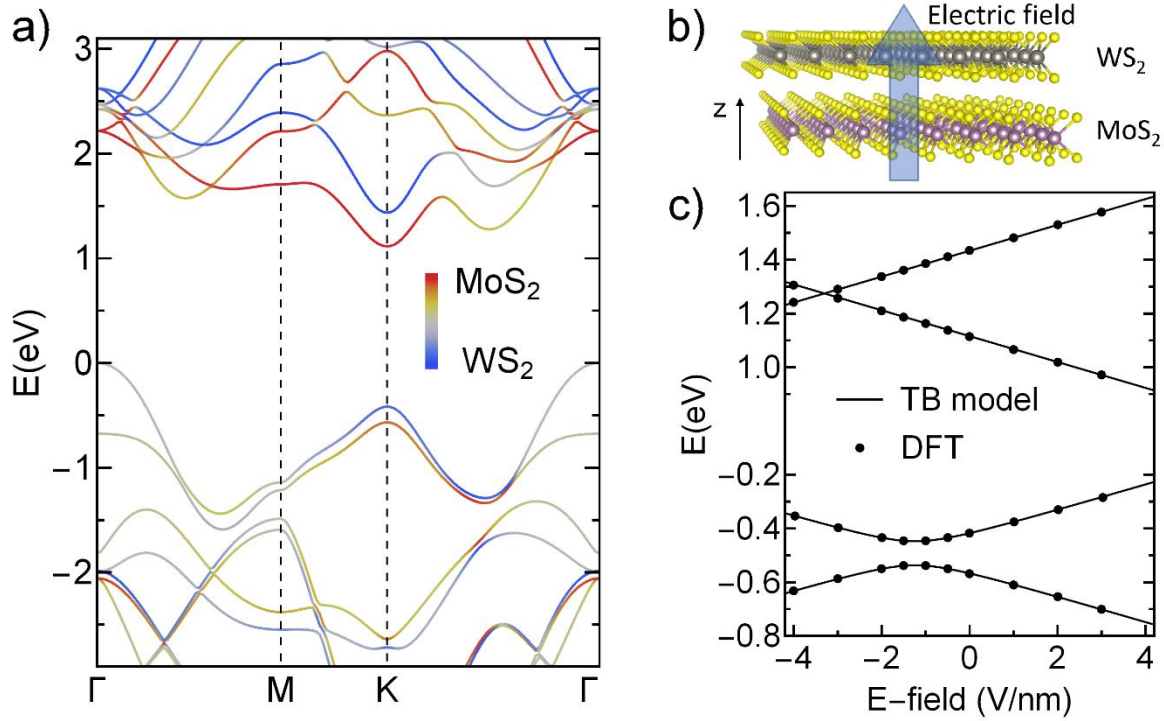


**Figure 5.2** (a) DFT band structure of MoS<sub>2</sub>/WS<sub>2</sub> heterostructure without SOC, with the color indicating the projection of the wavefunction onto each layer. (b) Schematic plot showing an external electric field applied to the heterostructure. (c) The energy of the top two valence bands and bottom two conduction bands at K point as a function of the external electric field, without including SOC.

### 5.3 Interlayer Coupling at the Excitonic Level

In addition to the single-particle level, the interlayer coupling also plays a critical role in determining the properties of the heterostructure at the excitonic level. In order to show that, a

many-body GW+BSE calculation is performed, which is proven to be reliable in calculating excited-state properties of monolayer TMDCs [80, 143]. The dielectric function is evaluated with an  $18 \times 18 \times 1$  k-point grid, 10 Ry energy cutoff and 400 conduction bands in the summation. The quasiparticle band gap is then determined from a single-shot  $G_0W_0$  calculation. The excitonic effects are included by solving the BSE on a finer k-point grid of  $90 \times 90 \times 1$ . A slab Coulomb truncation is implemented to avoid interactions between periodic images [59]. These calculations are done with the BerkeleyGW package [44].

For  $\text{MoS}_2/\text{WS}_2$ , the GW correction increases the direct band gap at K from 1.62 eV to 2.42 eV. A scissor operator is used to fit the GW correction to the first two valence and conduction bands near the K point, which introduces no more than 0.01 eV error compared with the full GW result. Our further calculations show that the GW correction is insensitive to the external electric field.

At the BSE level, we determine the energy and dipole oscillator strength of the interlayer exciton, as shown by the dots in Figure 5.3. In the following, we reveal the key role played by the coupling between the valence bands in explaining these results. Focusing on the lowest-energy interlayer and intralayer excitons, i.e. the so-called “1s” exciton, the BSE can be written in the basis of individual (uncoupled) layers as

$$(\varepsilon_c - \varepsilon_v)A_{vc}^S + \sum_{v'c'} \langle vc|K|v'c' \rangle A_{v'c'} = \Omega^S A_{vc}^S, \quad (5.1)$$

where  $|S\rangle = \sum_{vc} A_{vc}^S |vc\rangle$  is the exciton eigenstate,  $v$  and  $c$  are the layer index of the valence and conduction band,  $\varepsilon_v$  and  $\varepsilon_c$  are the bare band edge energies of each layer (without including the interlayer coupling),  $\Omega^S$  is the exciton energy, and  $K$  is the electron-hole interaction kernel. We have absorbed the k-point indices and focus on the effect of interlayer coupling. The non-zero

matrix elements of the kernel  $K$  are the binding energies of the exciton between two individual layers (MoS<sub>2</sub> intralayer, WS<sub>2</sub> intralayer, and interlayer exciton, respectively):

$$\langle v_{Mo}c_{Mo} | K | v_{Mo}c_{Mo} \rangle = -\varepsilon_{B,Mo},$$

$$\langle v_Wc_W | K | v_Wc_W \rangle = -\varepsilon_{B,W},$$

$$\langle v_Wc_{Mo} | K | v_Wc_{Mo} \rangle = \langle v_{Mo}c_W | K | v_{Mo}c_W \rangle = -\varepsilon_{B,inter},$$

which are treated as parameters in the model and are extracted from the *ab initio* calculation. It's worth noting that the intralayer exciton binding energy here should be differentiated from that of an isolated monolayer, because although it assumes no interlayer hopping, it does reflect the impact of dielectric screening from the other layer.

Combining the above assumptions, the BSE Hamiltonian can be written in the bare electron-hole basis as a 4-by-4 matrix:

$$\begin{pmatrix} \varepsilon_{c_{Mo}} - \varepsilon_{v_W} - \varepsilon_{B,inter} & & & t \\ & t & & \\ & & \varepsilon_{c_{Mo}} - \varepsilon_{v_{Mo}} - \varepsilon_{B,Mo} & \\ & & & \varepsilon_{c_W} - \varepsilon_{v_W} - \varepsilon_{B,W} \\ & & & & t \\ & & & & & \varepsilon_{c_W} - \varepsilon_{v_{Mo}} - \varepsilon_{B,inter} \end{pmatrix} \begin{pmatrix} (\leftrightarrow v_Wc_{Mo}) \\ (\leftrightarrow v_{Mo}c_{Mo}) \\ (\leftrightarrow v_Wc_W) \\ (\leftrightarrow v_{Mo}c_W) \end{pmatrix}$$

The eigenvalues and eigenvectors of this matrix describe the energy and layer composition of the exciton eigenstates. The off-diagonal interlayer coupling  $t$  is responsible for mixing the intralayer and interlayer exciton. This simple model can reproduce the exciton energy and dipole strength from the *ab initio* calculation very well, as shown in Figure 5.3, thus validating the assumptions made above. The parameters used in this model for MoS<sub>2</sub>/WS<sub>2</sub> and MoSe<sub>2</sub>/WSe<sub>2</sub> heterostructures are summarized in Table I.

| Heterostructure                     | $\epsilon$ | $t$    | $\epsilon_{B,Mo}$ | $\epsilon_{B,W}$ | $\epsilon_{B,inter}$ |
|-------------------------------------|------------|--------|-------------------|------------------|----------------------|
| MoS <sub>2</sub> /WS <sub>2</sub>   | 6.5        | 45 meV | 0.6 eV            | 0.57 eV          | 0.51 eV              |
| MoSe <sub>2</sub> /WSe <sub>2</sub> | 7.4        | 49 meV | 0.56 eV           | 0.53 eV          | 0.49 eV              |

**Table 5.1** Key parameters in the model for MoS<sub>2</sub>/WS<sub>2</sub> and MoSe<sub>2</sub>/WSe<sub>2</sub> heterostructure.

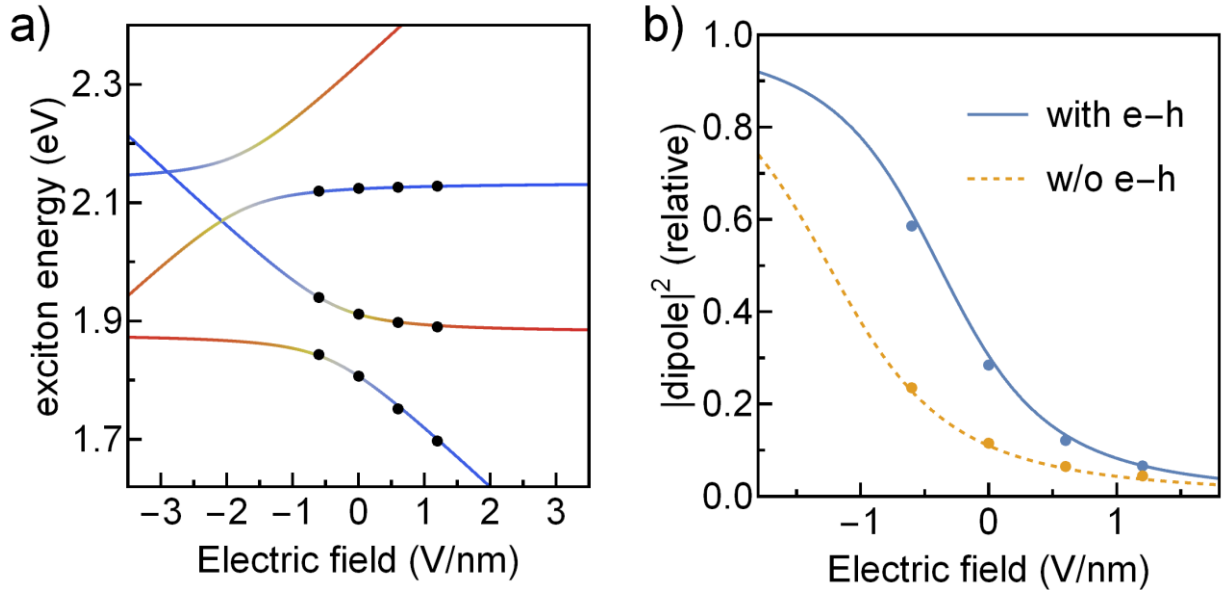


**Figure 5.3** (a) Energy of the exciton eigenstates in MoS<sub>2</sub>/WS<sub>2</sub> heterostructure as a function of the external electric field. Dots indicate the first-principles result and the line comes from the model. Color of the line indicate the character of the hole in the exciton. Red means the hole is in MoS<sub>2</sub> and blue is in WS<sub>2</sub>. (b) Squared transition dipole of the lowest energy exciton as a function of the external electric field, relative to the squared transition dipole of the lowest energy exciton in single layer MoS<sub>2</sub> (for which we find a value –in atomic units- of 0.02 per unit area). Dash line shows similar result without considering electron-hole interaction. The results are obtained in the absence of spin-orbit coupling.

Without interlayer coupling, the interlayer exciton energy would change linearly with the electric field  $E$  via the (quantum-confined) Stark effect [131, 144], while its oscillator strength would be independent of  $E$ . However, as shown in Figure 5.3(a), due to the interlayer coupling, the interlayer and MoS<sub>2</sub> intralayer exciton states mix leading to an anti-crossing behavior. The

electric field can gradually tune the nature of the lowest-energy exciton of the heterostructure from primarily interlayer to primarily intralayer. During this process, the overlap of the electron and hole wavefunction gradually increase, resulting in a gradually enhanced exciton oscillator strength, as shown in Figure 5.3(b). This model demonstrates how the interlayer coupling enables the tuning of excitonic properties with external electric field.

## 5.4 Tunable Excitonic Properties

Having benchmarked our model against first principles calculations in the absence of SOC, we now proceed to add this additional effect which splits the spin-up and spin-down bands and changes the exciton energy, as shown in the schematic plot Fig. 5.1. Because spin along the vertical direction is a good quantum number near the K point [145], we can include SOC as a perturbation. We take the spin-orbit correction to be the band energy difference between a noncollinear spin-orbit DFT calculation and a spin-unpolarized DFT calculation without interlayer coupling:  $\Delta\varepsilon_{nk\sigma}^{SO} = \varepsilon_{nk\sigma}^{SO} - \varepsilon_{nk}$ . The spin-orbit correction to the GW quasiparticle energies is assumed to be the same as the spin-orbit correction to the DFT energies [30]. The spin-orbit splitting at the VBM is around 160 meV for MoS<sub>2</sub> and 440 meV for WS<sub>2</sub>, while at the CBM it is only 3 meV for MoS<sub>2</sub> and 40 meV for WS<sub>2</sub>. The interlayer interaction couples the like-spin bands the same way as discussed before. Therefore, the band anti-crossing like the one in Fig. 5.2(c) is still present, but only with valence bands of like-spin, as shown in Fig. 5.4.

SOC affects the excitonic properties via the spin-orbit splitting of the band edge energies that enter the diagonal of the aforementioned BSE Hamiltonian. We neglect the k-point dependence of the spin-orbit splitting since the exciton is centered closely around the K point. We've neglected the impact of SOC on the exchange part of the electron-hole interaction, which is below 20 meV, much smaller than the SOC splitting. Then the full exciton eigenstate is solved

with the interlayer coupling following the same procedure. Finally, the imaginary part of the dielectric function is calculated using formula  $\epsilon_2(\omega) = \frac{16\pi^2 e^2}{\omega^2} \sum_{S\sigma} |\mathbf{e} \cdot \langle 0|\mathbf{v}|S\sigma\rangle|^2 \delta(\omega - \Omega_{\sigma}^S)$ , where  $\mathbf{e}$  is the polarization of the incident light,  $\mathbf{v}$  is the velocity operator and  $|S\sigma\rangle$  is the exciton eigenstate with spin  $\sigma$ . Higher excitonic states in the series such as the 2s state are not included.

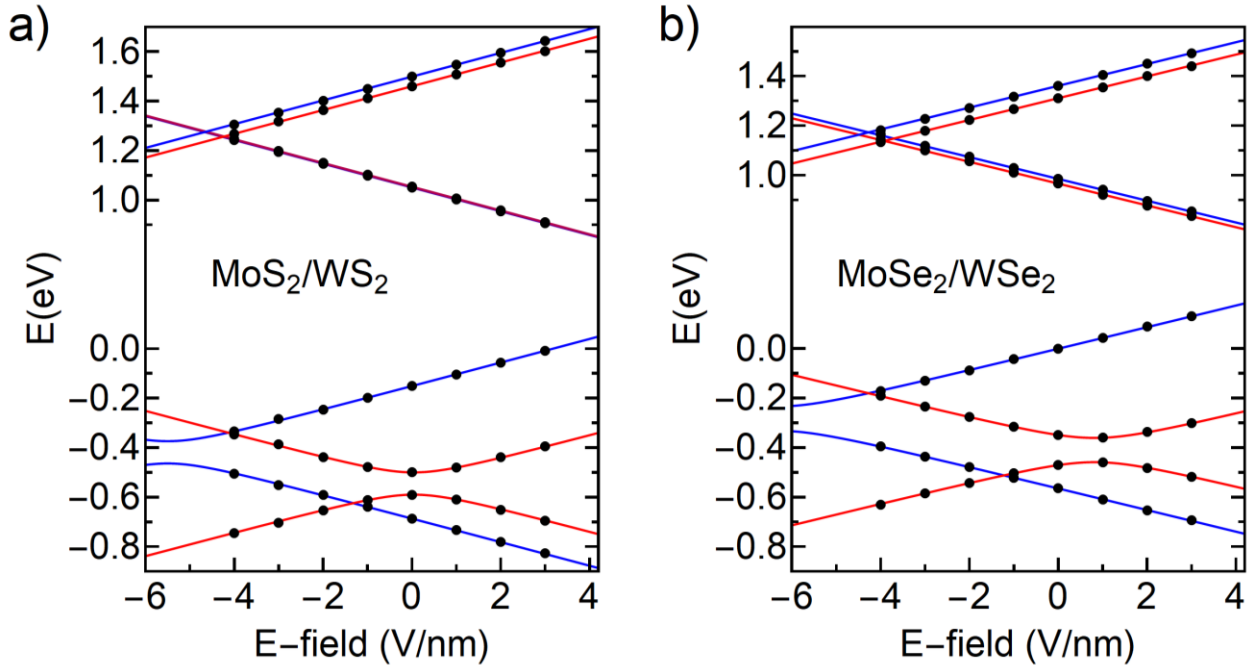


**Figure 5.4** The energy of the top valence bands and bottom conduction bands at K point versus the external electric field for (a) MoS<sub>2</sub>/WS<sub>2</sub> and (b) MoSe<sub>2</sub>/WSe<sub>2</sub> heterostructure including the spin-orbit coupling. The dotted are the DFT-calculated results and the lines are from our interlayer coupling model.

The blue and red lines represent spin-up and spin-down bands, respectively.

The calculated exciton energies together with the simulated absorption spectrum  $\epsilon_2(\omega)$  at different electric fields are shown in Figure 5.5(a) and 5.5(b) for MoS<sub>2</sub>/WS<sub>2</sub> and MoSe<sub>2</sub>/WSe<sub>2</sub>, respectively. After including SOC, the spin-up bands (associated exciton states indicated by blue dashed lines) of WX<sub>2</sub> and the spin-down bands (associated exciton states indicated by red dashed lines) of MoX<sub>2</sub> (X=S, Se) have the higher energy at the K point. The top valence band, mainly

from  $WX_2$  and responsible for the lowest energy interlayer exciton, moves further apart from the like-spin band from  $MoX_2$ . Therefore, for the lowest energy exciton, the impact of the interlayer coupling is weaker at zero field with the inclusion of SOC and the anti-crossing behavior is apparent only for  $|E| > 5\text{V/nm}$  for  $MoS_2/WS_2$ , resulting in a more linear Stark shift and a smaller oscillator strength of lowest exciton at low field. On the other hand, the anti-crossing behavior is seen in the higher-lying exciton states at relatively low electric field values as shown in Fig. 5.4(a), which provides an easy way to experimentally determine the strength of the interlayer coupling by optical absorption measurements.

The  $MoSe_2/WSe_2$  bilayer heterostructure shares a very similar band alignment (see Fig. 5.4(b)) and interlayer coupling with  $MoS_2/WS_2$  (see Table I). Therefore, as shown in Fig. 5.5(b), the dependence of exciton energy and optical absorption on the electric field in  $MoSe_2/WSe_2$ , including the anti-crossing behavior, is very similar to that of  $MoS_2/WS_2$ , with only quantitative difference. Specifically, the exciton energies are about 0.2 eV lower in  $MoSe_2/WSe_2$ . Moreover, due to slightly different band energy and SOC, the anti-crossing point for the lowest exciton is moved to an even higher electric field around 6V/nm.

Although the anti-crossing behavior in energy is inaccessible at low electric field for the lowest exciton, the impact of the interlayer coupling can still be seen from the tunability of the radiative lifetime. The radiative lifetime of the lowest exciton is an important parameter for photoluminescence and electron-hole separation process. For 2D materials, the intrinsic radiative lifetime of exciton at zero temperature is directly related to the dipole strength by  $\tau_S^{-1} = \frac{8\pi e^2 \Omega_S \mu_S^2}{\hbar^2 c A_{uc}}$ , where  $\Omega_S$  is the energy of the exciton state S,  $\mu_S^2$  is the modulus square dipole strength of the exciton divided by the number of k-points, and  $A_{uc}$  is the area of the unit cell. Then the



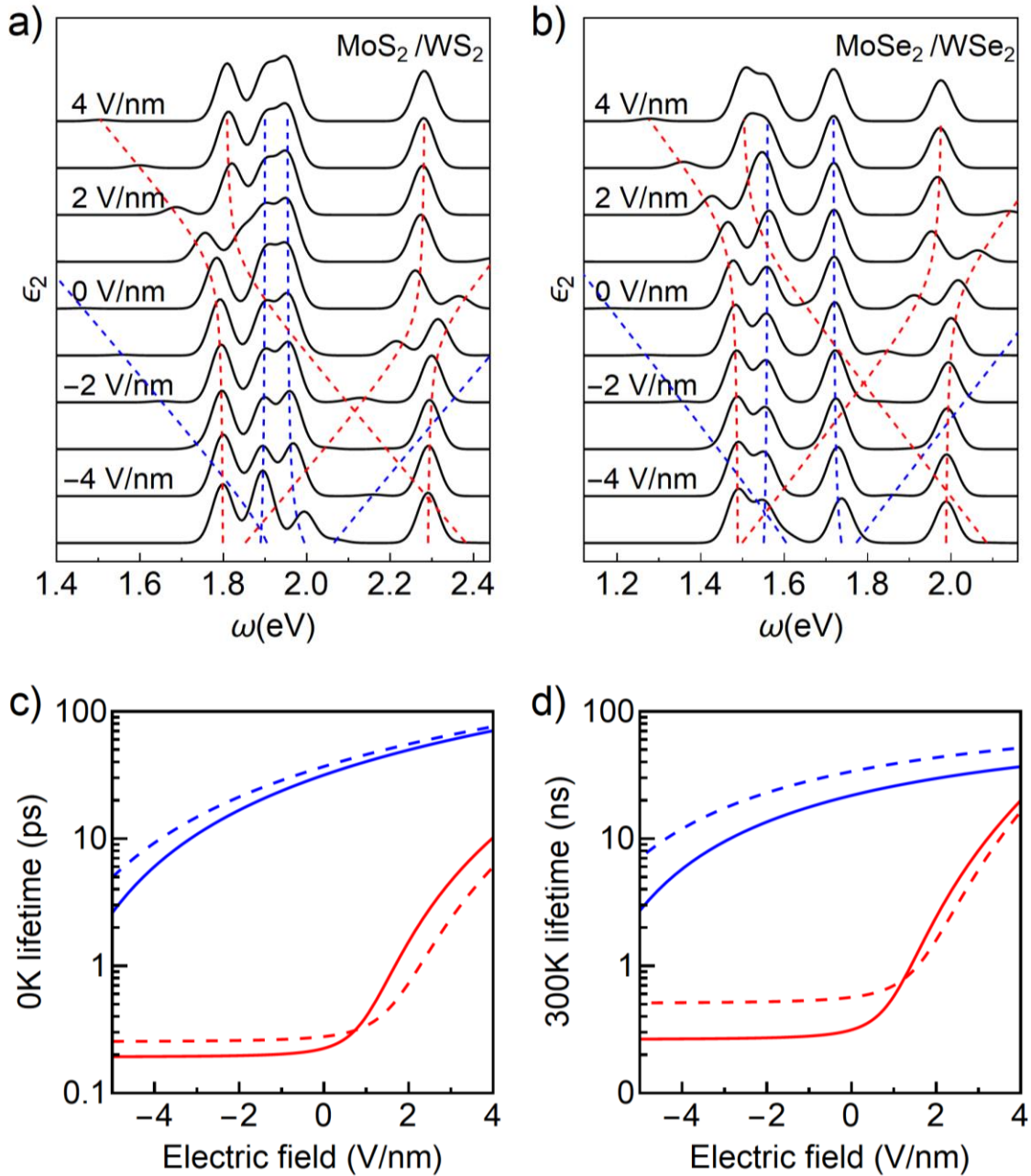


**Figure 5.5** (a, b) Imaginary part of dielectric function  $\epsilon_2$  for (a) MoS<sub>2</sub>/WS<sub>2</sub> and (b) MoSe<sub>2</sub>/WSe<sub>2</sub> heterostructure calculated from the model including spin-orbit coupling for different electric field values. Blue and red dashed line indicate the energy of the exciton with electron spin up and down, respectively. (c, d) Radiative lifetime of the lowest two exciton branches, for MoS<sub>2</sub>/WS<sub>2</sub> (solid line) and MoSe<sub>2</sub>/WSe<sub>2</sub> (dash line) heterostructure, with blue and red corresponding to their electron spin up and down, at (c) 0K and (d) 300K as a function of the external electric field.

exciton lifetime at finite temperature can be obtained by thermally averaging the exciton lifetime assuming a parabolic dispersion [133, 146]. Figure 5.4(c) and 5.4(d) shows the 0K and 300K radiative lifetime of the two lowest exciton branches. The lifetime value at zero electric field is in good agreement with a previous calculation [133]. Because of the electric field tuning of the exciton oscillator strength, the lifetime of the lowest exciton increases by two orders of magnitude as the electric field increase from -6V/nm to 4V/nm. This shows that the lifetime of lowest (interlayer) exciton in these heterostructures can be widely tuned by the external gate field. Recently, an experiment [147] in MoSe<sub>2</sub>/WSe<sub>2</sub> heterostructure have observed such gate-tuning of exciton radiative lifetime by an order of magnitude.

It is worth noting that the same physical picture can also lead to gate-tunable excitons in bilayer homojunctions. Indeed, recent experimental works have reported the observation of gate-tunable exciton energy and lifetime in bilayer WSe<sub>2</sub> [148, 149].

In conclusion, we have studied the band alignment and excitonic properties of MoS<sub>2</sub>/WS<sub>2</sub> and MoSe<sub>2</sub>/WSe<sub>2</sub> bilayer heterostructures from first principles DFT and GW+BSE calculation. We have shown that interlayer coupling is the key to understanding their properties, allowing the nature of the lowest-energy exciton to be tuned gradually from interlayer to intralayer by an external gate field. This is accurately captured by our simple model which accounts for the interlayer coupling in the presence of electron-hole interactions, which predicts an anti-crossing behavior of the exciton energy, as well as widely tunable dipole oscillator strength and radiative lifetime of the lowest-energy excitons by an order of magnitude with an external gate field of a few V/nm. Our result provides a quantitative physical picture of excitons in bilayer vdW heterostructures which would benefit future investigations of the gate-tunable excited-state properties in 2D heterostructures.

# **Chapter 6: Edge-insensitive Magnetism and Half Metallicity in Graphene Nanoribbons**

## **6.1 Introduction**

Ever since its first isolation in 2004 [1], graphene along with its derivative structures has been a long-standing focal point for nanoelectronics research [150, 151]. Particularly, they have many desired properties for spintronics and spin qubit devices, including high mobility, long spin lifetime, and gate-tunable carrier concentration, in addition to an almost vanishing thickness [7, 152, 153]. However, due to the absence of localized  $d$  or  $f$  electrons, magnetism does not naturally appear in pristine graphene, and its realization usually relies on specific transition-metal adatoms, defects, or specific edge structures [154]. One of the most attractive candidates for graphene-based spintronic device is the mono-hydrogenated zigzag graphene nanoribbons (commonly referred as ZGNRs), in which graphene is terminated by the zigzag edge on both sides with single hydrogen atom occupying each dangling bond. It was proposed by Son et al. in 2006 [155] with *ab initio* DFT calculations that this structure becomes half-metallic under a cross-ribbon electric field. This is because the mono-hydrogenated edge produces a localized edge state [156, 157], which leads to a high electronic density-of-state (DOS) and forms a ferromagnetic (FM) ordering along the edges and an antiferromagnetic ordering at the opposite edges. However, the appearance of this magnetic structure is premised upon precisely realizing the mono-hydrogenated edge. Besides, it was shown that this mono-hydrogenated edge is energetically less stable [158-162] and would give way to other edge structures, such as the mono- and di-hydrogenated armchair (a11 and a22) edges (Figures 6.1 (a) and (b)) and a reconstructed zigzag edge with one di- and two mono-hydrogenated sites (z211, Figure 6.1 (c)), under standard conditions in terms of environment hydrogen concentrations [163].

Unfortunately, GNRs formed by those more stable edges are semiconducting and non-magnetic. This is commonly speculated [164, 165] as the reason why experimental evidence of magnetism in ZGNRs has been scarce and indirect [166, 167] for over a decade since the theoretical prediction.

Recently, a few two-dimensional (2D) semiconductors, including GaSe,  $\alpha$ -SnO, and InP<sub>3</sub>, have been proposed as potential FM or multiferroic materials under free-carrier doping [168-170]. The mechanism behind their magnetic ordering is their unique Mexican-hat-shaped band structure that contributes to a significant peak in DOS. By tuning the Fermi level near this peak via doping, the electron-electron exchange interactions can overcome the kinetic energy cost and allow the doped carriers to form itinerant ferromagnetism and half-metallicity. These studies opened a new path for realizing magnetism in low-dimensional structures without involving localized *d* or *f* electrons. One-dimensional (1D) structures like GNRs have intrinsically more divergent van Hove Singularities (vHSs) in their DOS, which give rise to better chances of realizing magnetism via this mechanism. Particularly, because this is essentially an edge-unrelated quantum confinement effect, it may bypass the stringent requirement for edge structures and offers the potential to realize magnetism and half-metallicity in GNRs.

## 6.2 Magnetism in Doped Graphene Nanoribbons

In this Letter, we consider three types of GNRs as shown in Figure 6.1, which include the two common types of edges, ones along the armchair and zigzag directions, and different types of edge hydrogen passivation as well. These structures are known to be the energetically most stable ones but unfortunately do not exhibit any magnetism intrinsically [163]. Following the convention in Ref. [163], we denote these edge structures as a11, a22 and z211 respectively, where a/z stands for armchair/zigzag edge, and the number denotes how many hydrogen atoms

are bonded with each of the consecutive edge carbon atoms within a unit cell. Additionally, we use a number in front to denote the width by the number of C-C dimers or zigzag chains along GNRs. We do not include the mono-hydrogenated ZGNRs because they are intrinsically antiferromagnetic and doping does not essentially change their edge magnetism [171].

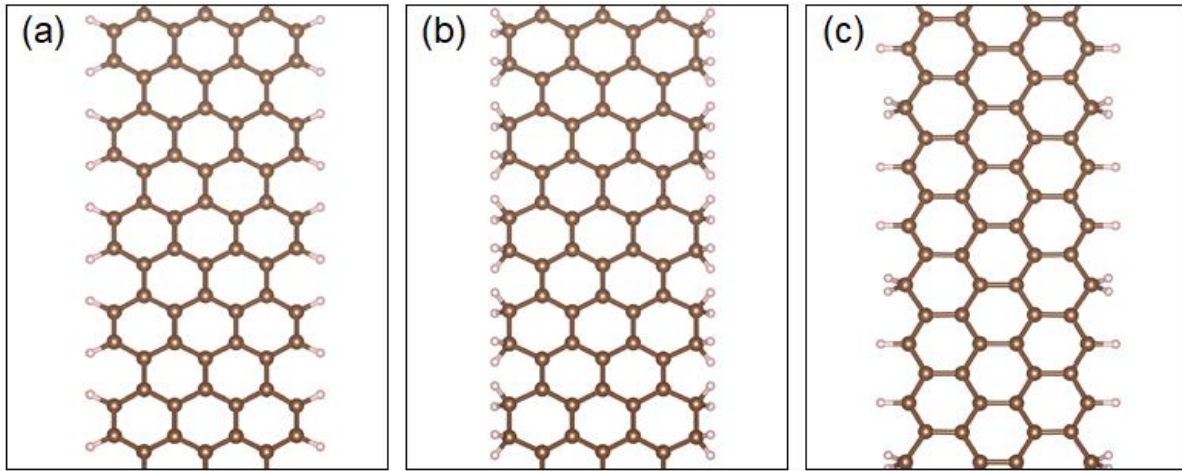


**Figure 6.1** Examples of GNRs with three different type of edges considered in this chapter. From left to right are (a) 7-a11-GNR, (b) 7-a22-GNR and (c) 4-z211-GNR. The edge dangling bonds are passivated by hydrogen atoms.

Our DFT calculation is based on the *ab initio* pseudopotential projector-augmented wave (PAW) method [172] as implemented in the Vienna *ab initio* simulation package (VASP) [40]. The spin-polarized GGA with Perdew–Burke–Ernzerhof parametrization (GGA-PBE) [58] is used for the exchange-correlation functional. A cutoff energy of 800 eV for the plane-wave basis is used.

Structural relaxation is performed with a converge criteria of  $1 \times 10^{-2}$  eV/Å on force and a  $\Gamma$ -centered k-point grid of  $1 \times 1 \times 20$ . Electron self-consistency loop is performed with a converge criteria of  $1 \times 10^{-8}$  eV for total energy and a Gaussian smearing of 0.0001 eV for electron occupation to ensure accurate convergence of the magnetic state. A  $\Gamma$ -centered k-point grid of 1

$\times 1 \times 200$  is used for the armchair (a11 and a22) GNR and  $1 \times 1 \times 100$  is used for the zigzag (z211) GNR. Rigid-band doping, which changes the total number of electrons in the unit cell with a compensating jellium background, is used to mimic the electrostatic doping.

We first focus on the intensively-studied mono-hydrogenated a11-GNRs, which do not exhibit any magnetism before doping. Presented in Figure 6.2 are the electronic band structure, DOS, and magnetization density of a 4-a11-GNR under a hole doping density of 0.35 hole/nm (corresponding to an approximate planar charge density of  $7 \times 10^{13} \text{cm}^{-2}$ ), obtained using a spin-polarized DFT calculation. Upon doping, the carriers spontaneously polarize into one spin population and form a FM ground state. As shown in Figures 6.2 (a) and (b), the bands corresponding to different spins are split, and the Fermi energy only intersects with the band of a single spin, making this system a perfect half metal. The splitting between the opposite-spin bands at the valence band maximum (VBM) is about 85 meV, equivalent to a Zeeman splitting under a huge external magnetic field of 730 T (assuming a spin  $g$  factor of 2 and no orbital contribution). We also plot the real-space magnetization density (difference between the density of opposite-spin electrons) of the spin-polarized states. As shown in Figure 6.2 (c), the magnetization density is distributed around the whole GNR, indicating that it is not originated from the edge. Magnetization density for wider a11-GNRs and other types of GNRs are plotted in the Figure 6.3, which further confirms that the magnetization density does not fall off when moving away from the edge.

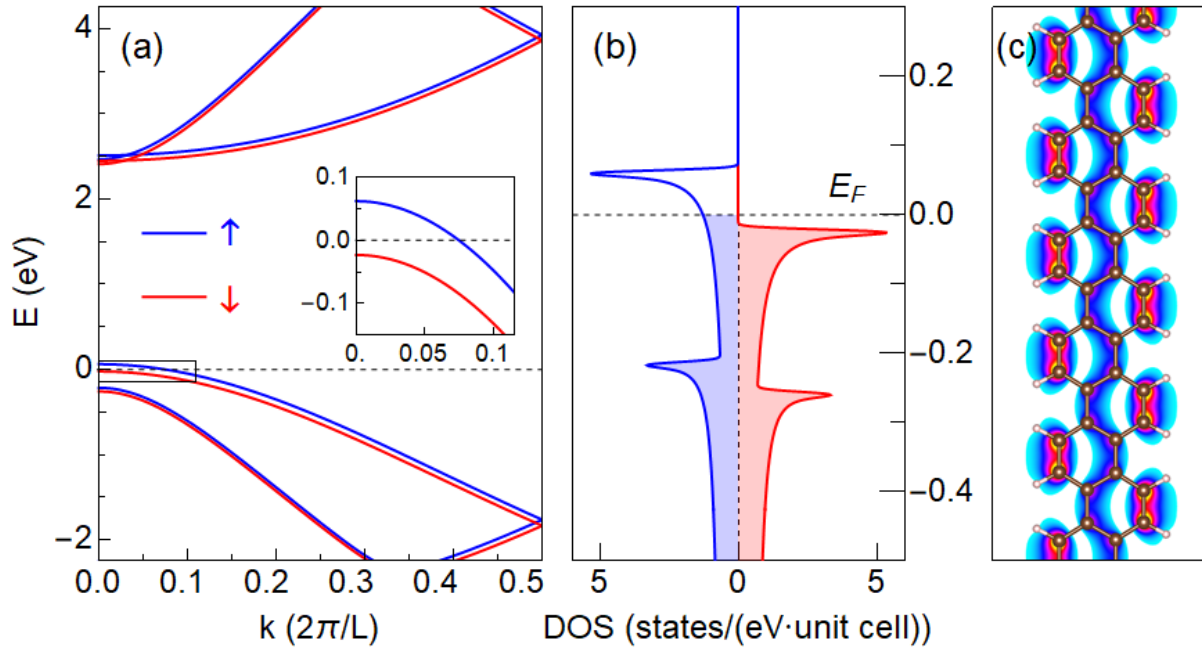


**Figure 6.2** The DFT-calculated (a) band structure, (b) spin-projected DOS, and (c) real-space magnetization density of hole-doped 4-a11-GNR at hole density 0.35/nm. Fermi energy is set to be zero. Inset of (a) shows a zoomed-in view of band structure near the fermi energy, at the region indicated by the black rectangle on the main plot.

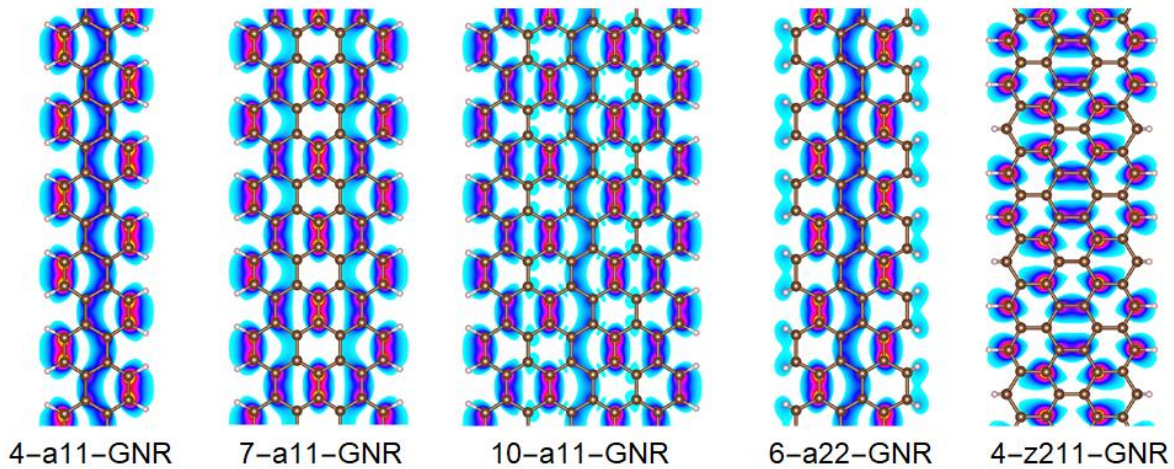


**Figure 6.3** Magnetization density plot for p-doped 4-a11-GNR, 7-a11-GNR, 10-a11-GNR, 6-a22-GNR, and 4-z211-GNR. The magnetization density does not decay when moving away from the edge, which shows the magnetism originate from the bulk state instead of edge state.

This doping-induced magnetism and half metallicity are robust for different doping types and densities, suggesting the possibility of bipolar spintronics applications. Figure 6.4 (a) shows the magnetic moment and spin polarization energy (difference between the FM and paramagnetic ground-state energy) per carrier as a function of the electron or hole doping density for this 4-a11-GNR. As we can see, for both electron and hole doping, the spins of the free carriers are completely polarized with a saturated magnetic moment of  $1 \mu_B/\text{carrier}$ , forming a perfect half-metallic state. The half-metallic FM ground state exists for a wide range of doping density up to 0.1 electron/nm for n-doping and 0.4 hole/nm for p-doping. Beyond this range, the magnetic moment rapidly drops to zero, and a paramagnetic ground state is restored.

Spin polarization energy defines the strength of magnetic orders and determines the spin correlation length in 1D and transition temperature in higher dimensions [173]. Although the magnetic momentum is saturated for nearly the entire FM phase, the spin polarization energy per carrier exhibits an inverted parabola shape with a maximum roughly in the middle. For example, for 4-a11-GNR, as shown in Figure 6.4 (a), the maximum is  $\Delta E_{max} = 7 \text{ meV}$  at a hole density of  $n_{max} = 0.2/\text{nm}$ . For electron doping, the value is comparatively smaller, with  $\Delta E_{max} = 3 \text{ meV}$  at  $n_{max} = 0.07/\text{nm}$ .

This doping-induced magnetism and half metallicity are universal in narrow GNRs and can be observed in different widths. Figure 6.4 (b) shows a wider 7-a11-GNR, which also exhibit the FM ground state under both electron and hole doping. The magnetic moment is fully saturated although the spin polarization energy is reduced to around 3~4 meV per carrier. Generally, magnetism becomes weaker with increasing ribbon width, and for a11-GNRs with a width larger than 1.3 nm, the magnetic order is no longer detectable with a doping density resolution of



0.02/nm. This indicates that quantum confinement is the crucial factor to induce the magnetism and the magnetic order is limited within narrow GNRs. Recent experiments have demonstrated fabrication of high-quality narrow GNRs [153, 174, 175], making our prediction of immediate interests.

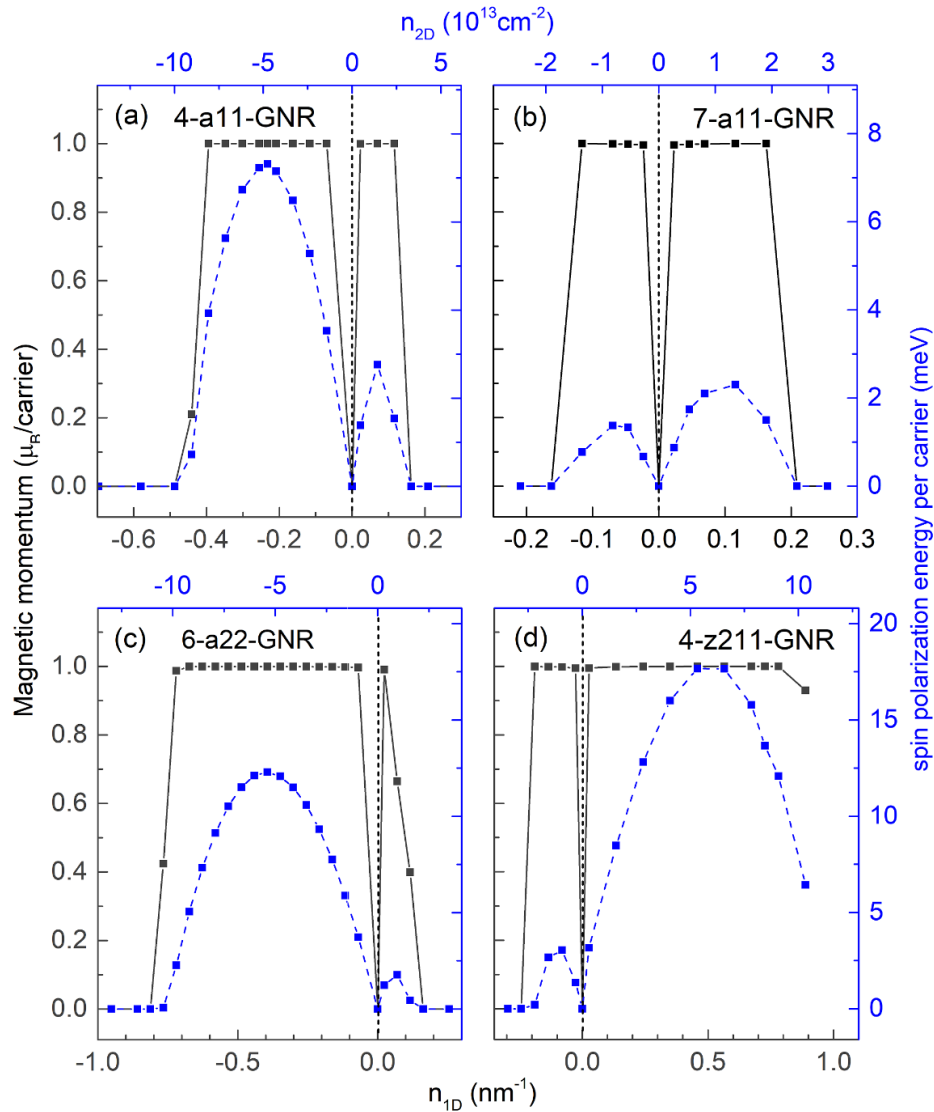


**Figure 6.4** Magnetic momentum (black solid line) and spin polarization energy (blue dashed line) per carrier versus electron doping density for (a) 4-a11-GNR, (b) 7-a11-GNR, (c) 6-a22-GNR, and (d) 4-z211-GNR. The doping density is shown in 1D (number of electron or hole per nm) on the bottom axis and in 2D (number of electron or hole per  $\text{cm}^2$ ) on the top axis. Positive and negative density correspond to electron and hole doping, respectively.

Different edge passivations and edge types are known challenges to realize edge magnetism in GNRs. However, this is no longer a barrier to prevent the quantum-confinement induced magnetism from doped narrow GNRs. As shown in Figure 6.4 (c), the FM ground state is also observed in doped 6-a22-GNR which has a different passivation of the armchair edge. The magnetic moment per carrier is saturated, and the spin polarization energy reaches above 10 meV per carrier for hole doping, even larger than that of narrower 4-a11-GNR. Moreover, Figure 6.4 (d) shows the FM ground state in the doped 4-z211-GNR, whose edge is energetically more stable than the mono-hydrogenated zigzag edge [163]. Interestingly, it has the largest spin polarization energy among all our studied GNRs, which reaches 17 meV per carrier at an electron doping density of 0.35 e/nm, larger than that of the armchair-edge GNRs with similar width.

In these studied GNRs, the corresponding range of planer doping density is within the  $10^{13} \text{ cm}^{-2}$  range, comparable with those predicted for the magnetic 2D monolayer GaSe [168]. This doping density is accessible with the electrostatic gate doping methods without the need for dopant atoms, which has been commonly used for a wide range of monolayer 2D materials that have similar electron affinity and ionization potential [176, 177]. It is also worth noting that optical doping that creates electron and hole simultaneously [56] could also lead to magnetism in the same way. Additionally, the spin polarization energy in these GNRs can reach a few times higher than that of GaSe ( $\sim 3 \text{ meV}$ ) and comes close to that of mono-hydrogenated ZGNR [155]. Finally, we have calculated the magnetic properties of narrow GNRs with defective edges. Magnetism and half-metallicity remain, as shown in Figure 6.5. Given the widely observed doping in nanostructures, this magnetism may be helpful for understanding a broad range of controversial measurements.

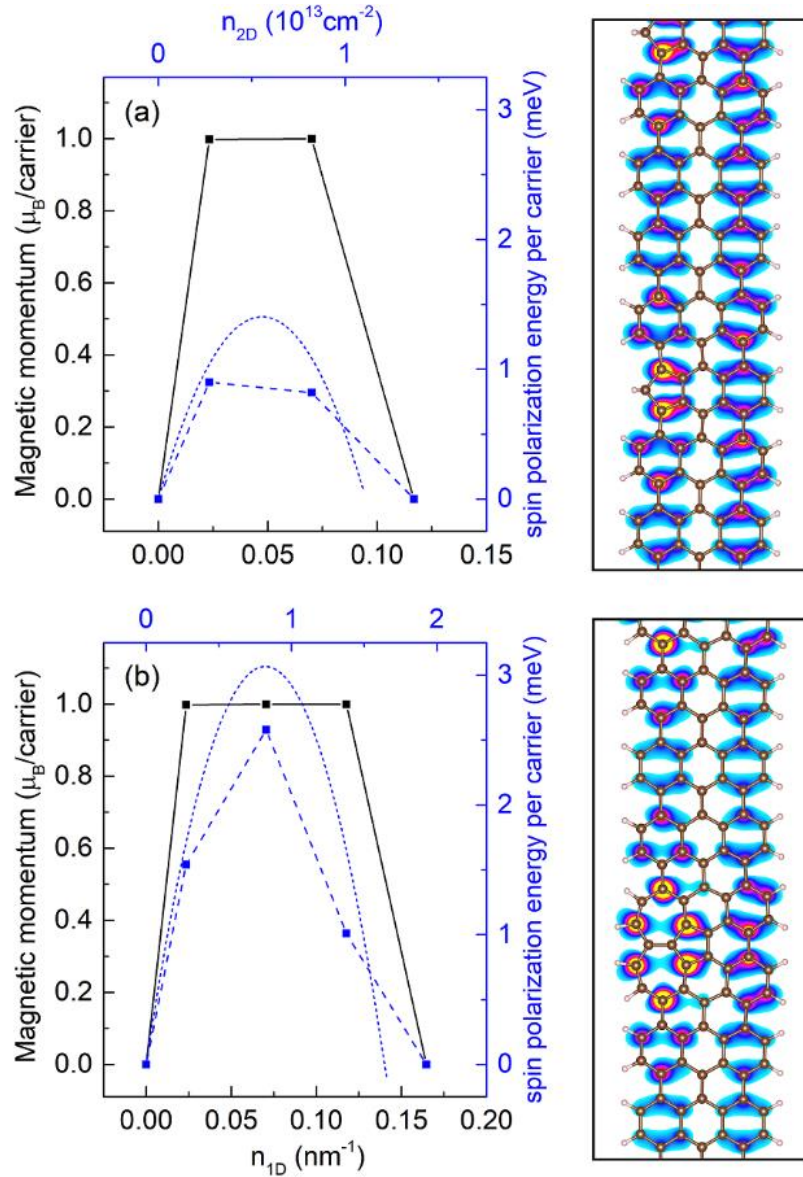


**Figure 6.5** Magnetic momentum and spin polarization energy per carrier versus hole doping density, and real-space magnetization density plot for 7-a11-GNR with two different types of defective edges. The first type (a) is a single pentagon due to the removal of one carbon atom. The second type (b) is a Stone–Wales defect. Both types of imperfections have been widely observed in experiments and can stand for general edge imperfections [178]. The defect density here is one per five unit cells, or 10% of the edge.

The defect does hybridize with the bulk state and leads to different band effective mass and Stoner parameter. However, the doping-induced itinerant ferromagnetism and half-metallicity remains, and the spin-polarization energy is close to that of pristine 7-a11-GNR. The blue dotted line shows the predicted spin-polarization energy from Stoner theory (see Eq. 6.4 below). It agrees with the DFT result, showing that the same mechanism applies to these defective structures.

### 6.3 Stoner Model of Itinerant Magnetism

The magnetism observed in doped GNRs above and its evolution with the ribbon width and doping density can be understood from the Stoner theory of itinerant magnetism. In the Stoner theory [179], the spin susceptibility of the paramagnetic state is given by  $\chi = \frac{N_0}{1-IN_0}$ , where  $N_0$  is the DOS at the Fermi energy and  $I$  is the Stoner parameter, decided by the electron exchange and correlation effects. Because the FM instability occurs when  $IN_0 > 1$ , both an enhanced DOS and a larger  $I$  will increase the likelihood of a FM instability. In a 1D system, because the vHS of DOS diverge as  $E^{-1/2}$  near the band extrema, the FM instability is much easier to be realized, which drives the formation of the FM states in doped GNRs. For example, for a 4-atom GNR, the DOS at the Fermi energy is 2.4/eV per carbon atom at a hole density of 0.1 hole/nm, comparable to the 2-3/(eV·atom) DOS of bulk 3d transition metals like iron, cobalt and nickel [180].

The Stoner theory can be quantitatively justified by first-principles DFT results. For a single band with effective mass  $m$ , the Stoner model correspond to a rigid shift in opposite directions for opposite spins near the band edge:

$$\varepsilon_{k\sigma} = \frac{\hbar^2 k^2}{2m} \pm \frac{I}{2}(n_{\uparrow} - n_{\downarrow}) \quad (6.1)$$

where  $I$  is the Stoner parameter that implicitly includes the exchange and correlation effects at mean-field level and  $n_{\uparrow}$ ,  $n_{\downarrow}$  are the density of spin-up and spin-down carriers. The total energy of the electrons (per unit length) is

$$E_{tot}(n_{\uparrow}, n_{\downarrow}) = \int_0^{\varepsilon_F^{\uparrow}} \varepsilon g(\varepsilon) d\varepsilon + \int_0^{\varepsilon_F^{\downarrow}} \varepsilon g(\varepsilon) d\varepsilon + In_{\uparrow}n_{\downarrow} \quad (6.2)$$

where  $g(\varepsilon)$  is the DOS of a single-spin band [181], which, after integrating, gives

$$E_{tot}(n_{\uparrow}, n_{\downarrow}) = \frac{\hbar^2 \pi^2}{6m} (n_{\uparrow}^3 + n_{\downarrow}^3) + In_{\uparrow}n_{\downarrow} \quad (6.3)$$

Therefore, the spin polarization energy as a function of the doping density is

$$\Delta E(n) = n\left(\frac{l}{4} - \frac{\pi^2 \hbar^2}{8m} n\right) \quad (6.4)$$

which is in close agreement with the DFT results shown in Figure 6.4. It leads to a critical

doping density  $n_c^{Stoner} = \frac{2ml}{\pi^2 \hbar^2}$ , below which the paramagnetic state becomes less favorable. It

also predicts that the spin-polarization energy reaches maximum  $\Delta E_{max}^{Stoner} = \frac{ml^2}{8\pi^2 \hbar^2}$  at the doping

density  $n_{max}^{Stoner} = \frac{nl}{\pi^2 \hbar^2}$ . We have plotted  $\Delta E_{max}$  and  $n_{max}$  extracted from DFT calculation

against the Stoner model predictions in Figures 6.6 (a) and (b), and the theoretical values are in

good agreement with the *ab initio* results.

According to this Stoner model, the FM instability come from the enhanced effective mass and Stoner parameter. Therefore, we can classify the strength of magnetism in GNRs according to these two parameters. As shown in Figures 6.6 (c) and (d), both the effective mass and the Stoner parameter decreases with the width of the nanoribbon. The electronic structures of GNRs falls into different groups depending on their width [182, 183]. Among them, the (3N+1)-a11-GNR, (3N+3)-a22-GNR, and (2N+2)-z211-GNR exhibit higher effective mass among each edge type and are thus more prone to having magnetism. For GNRs within the same family, the effective mass is inversely proportional to the effective width of the ribbon. This is due to the quantum confinement of graphene's Dirac dispersion  $\pi$  band [184, 185]. It follows a fitting formula  $m = a/(w - w_0)$ , as shown by the dashed line in Figure 6.6 (c), where  $w$  is the physical ribbon width and  $w_0$  is a correction that is found to be positive.

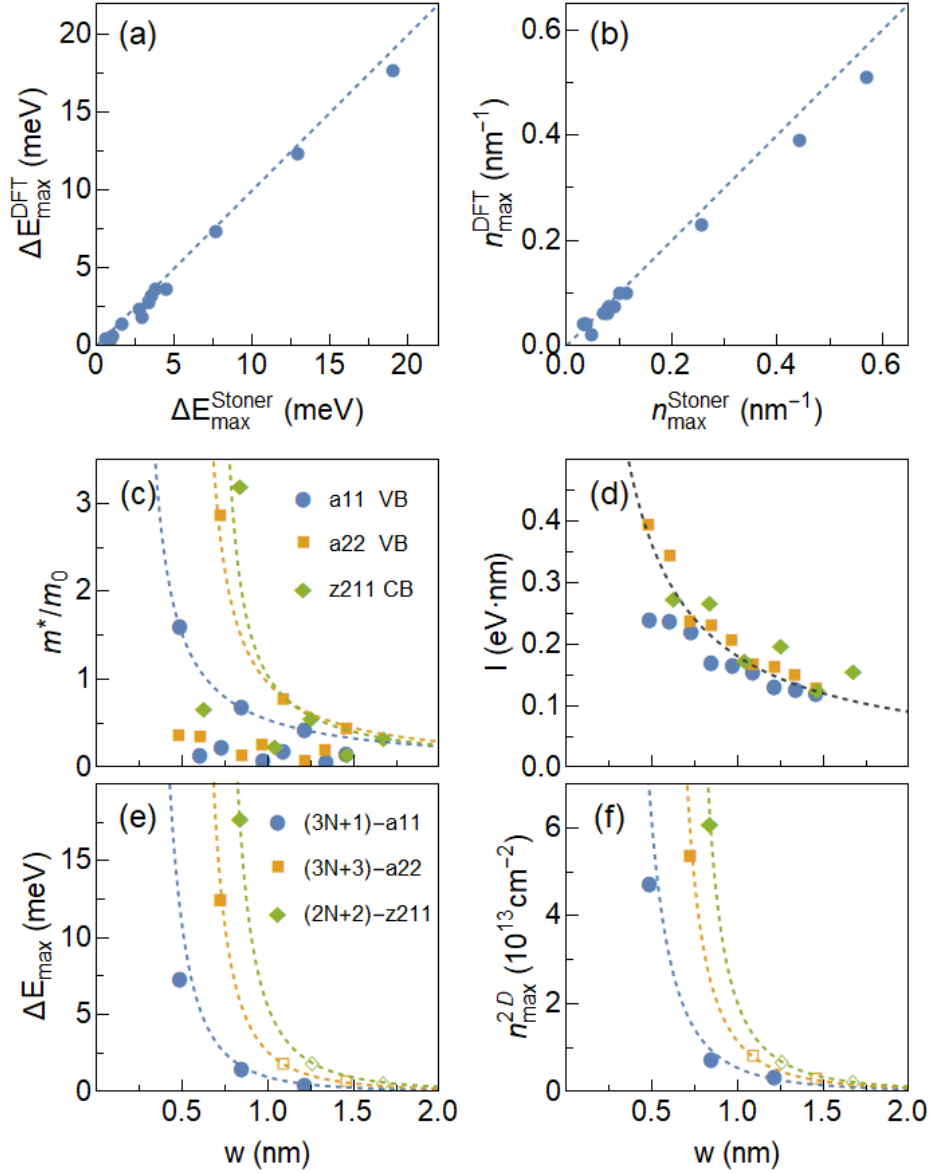


**Figure 6.6** (a, b) Comparison between Stoner model prediction and DFT result for (a) the maximum spin-polarization energy and (b) the doping density corresponding to this maximum. (c, d) Evolution of the (c) effective mass and (d) Stoner parameter of the valence band with respect to the ribbon width, for the top valence band (VB) of a11- and a22-GNR and bottom conduction band of z211-GNR. The dashed lines on (c) are a fitting curve for (3N+1)-a11-GNR, (3N+3)-a22-GNR and (2N+2)-z211-GNR (N=1,2,3) according to the formula  $a/(w - w_0)$ . The dashed line on (d) is a fitting according to the formula  $b/w$ . (e, f) Predicted evolution of (e) the maximum spin-polarization energy and (f) the corresponding planar doping density with respect to the ribbon width, for hole-doped (3N+1)-a11-GNR, (3N+3)-a22-GNR and electron-doped (2N+2)-z211-GNR. The filled marks indicate the DFT results and the hollow marks indicate the predicted values.

Meanwhile, the Stoner parameter is mainly decided by the local DOS at the Fermi energy and inversely proportional to the width  $w$ . The Stoner parameter  $I$  is given by the integral  $I = \int \gamma^2(\mathbf{r})v_{xc}[n(\mathbf{r})]d\mathbf{r}$ , where  $\gamma(\mathbf{r}) = \sum_n \delta(\varepsilon_F - \varepsilon_n)|\psi_n(\mathbf{r})|^2 / N_0$  is the local DOS at the Fermi energy (normalized by the total DOS), and  $v_{xc}[n(\mathbf{r})] = \left[ -\frac{d^2}{dm^2} n(\mathbf{r})\varepsilon_{xc}[n(\mathbf{r}), m] \right] \Big|_{m \rightarrow 0}$  is the second derivative of the exchange-correlation energy with respect to the magnetization [186].

When the same electronic state is confined within a region of width  $w$ , the local DOS will increase as  $\gamma(\mathbf{r}) \propto 1/w$ , which leads to an increase of the Stoner parameter as  $I \propto 1/w$ . This relation agrees well with the DFT calculation, as shown by the dashed line in Figure 6.6 (d). Particularly, we note that when comparing the value per atom,  $I$  is around a constant value 3.4 eV, which agrees with the Hubbard  $U$  term estimated for graphene nanoribbons [187, 188] and is over 6 times larger than that of bulk 3d transition metals like iron [180].

As a result, both the maximum spin-polarization energy  $\Delta E_{max}$  and the corresponding planar doping density is proportional to  $\frac{1}{w^2(w-w_0)}$ . The specific values of  $w_0$  and proportionality constants for different types of GNRs are summarized in the Table 6.1. In Figures 6.6 (e) and (f), we show the scaling of  $\Delta E_{max}$  and  $n_{max}^{2D}$  with the ribbon width for hole-doped (3N+1)-a11-GNR, (3N+3)-a22-GNR, and electron-doped (2N+2)-z211-GNR. It shows the emergence of magnetism in different GNRs as the ribbon width is narrowed down to around 1nm due to the strong cubic scaling. It is worth noting that the quantum confinement enhancement of the Stoner parameter is general and presents in all 1D structures. Therefore, this general mechanism can potentially be used to realize magnetism in other nanostructures as well.

| GNR type                | $w_0$ (nm) | $c$ (nm) | $d$ (meV·nm <sup>3</sup> ) |
|-------------------------|------------|----------|----------------------------|
| n-doped (3N+1)-a11-GNR  | 0.38       | 0.048    | 1.01                       |
| p-doped (3N+1)-a11-GNR  | 0.22       | 0.042    | 0.74                       |
| n-doped (3N+3)-a22-GNR  | 0.62       | 0.059    | 1.54                       |
| p-doped (3N+3)-a22-GNR  | 0.56       | 0.050    | 1.13                       |
| n-doped (2N+2)-z211-GNR | 0.70       | 0.054    | 1.65                       |
| p-doped (2N+2)-z211-GNR | 0.21       | 0.060    | 1.87                       |
| n-doped (2N+1)-z211-GNR | 0.41       | 0.019    | 0.43                       |
| p-doped (2N+1)-z211-GNR | 0.21       | 0.023    | 0.51                       |

**Table 6.1** Fitting Parameters for the maximum spin-polarization energy and corresponding planar doping density according to formula  $n_{max}^{2D} \approx \frac{c}{w^2(w-w_0)}$  and  $\Delta E_{max} \approx \frac{d}{w^2(w-w_0)}$ . The ribbon width  $w$  is counted starting half a C-C bond away from the outermost carbon atom.

In summary, we have predicted the existence of itinerant magnetism and half-metallicity in doped narrow GNRs within first-principle DFT calculation. The magnetism originates from the bulk electronic state of the ribbon and is independent of the specific edge structures. From the Stoner theory, the magnetism comes from the enhanced effective mass and Stoner parameter due to quantum confinement and its strength scales with the ribbon width in an inverse cubic relation. Given the widely observed doping in nanostructures, this magnetism is helpful for understanding a broad range of controversial measurements. Our findings propose a new route for realizing edge-independent magnetism in graphene nanoribbon and show that quantum confinement can be a general mechanism for realizing metal-free magnetism in nanostructures.



# **Chapter 7: Half-Metallicity with Strong Magnetic Anisotropy in Doped One- Dimensional Helical Tellurium Atomic Chain**

## **7.1 Introduction**

The bulk trigonal tellurium is a narrow gap semiconductor [189], which consists of helical chains of tellurium atoms bonded together by weak van der Waals interactions, as shown by Figure 7.1(a). Each chain has a periodicity of three atoms and can have either a left-handed or right-handed helical structure, breaking the inversion symmetry. Recently, this trigonal tellurium (Te) has gained increased attention because of experimental advances for achieving a potential 1D van der Waals material [190-193]. Particularly, large-area solution-grown 2D tellurium (termed by tellurene) with a pronounced air-stability and high carrier mobility has been successfully fabricated by a substrate-free solution phase process and mechanical exfoliation [191].

Moreover, tellurium nanowires have been synthesized by various growth mechanisms down to a few nanometers in diameter [194-197]. More recently, it has also been exfoliated from bulk into nanowires of 1-2 nm thickness and below 100 nm width, approaching the 1D single-atomic chain limit [192]. Thus, when the structure ultimately reaches the limit of a single atomic chain, DOS can be substantially enhanced and magnetism may emerge. Moreover, for heavy Te atoms, the strong spin-orbit-coupling (SOC) could connect spin with helical structures of the Te chains. This may couple the structural chirality with magnetism, enhancing the magnetic order with substantial spatial anisotropy and bring new applications, such as magneto-optical effects.

In this chapter, we study the electronic properties and magnetism of single-atomic Te chain using first-principles DFT calculation. We show that the quantum confinement effect can substantially

increase the electronic band gap and DOS as the material is thinned down to 1D, opening up the possibility of having non-trivial electronic ground state. Interestingly, unlike previous studies [168, 169, 170], in which only one type of doped carriers can induce magnetism, both electron-doping and hole-doping in the 1D Te chain induce a half-metallic ferromagnetic ground state, making it a perfect candidate material to realize 1D gate-tunable, defect-free, and metal-free ferromagnetism. Employing the Stoner theory, we explain why the Te chain shows such a robust ferromagnetic ground state as opposed to other 1D systems. Finally, we show that the helical structure combined with the strong spin-orbit interaction of tellurium pins the electron spin along the chain direction with an enhanced magnetic anisotropy.

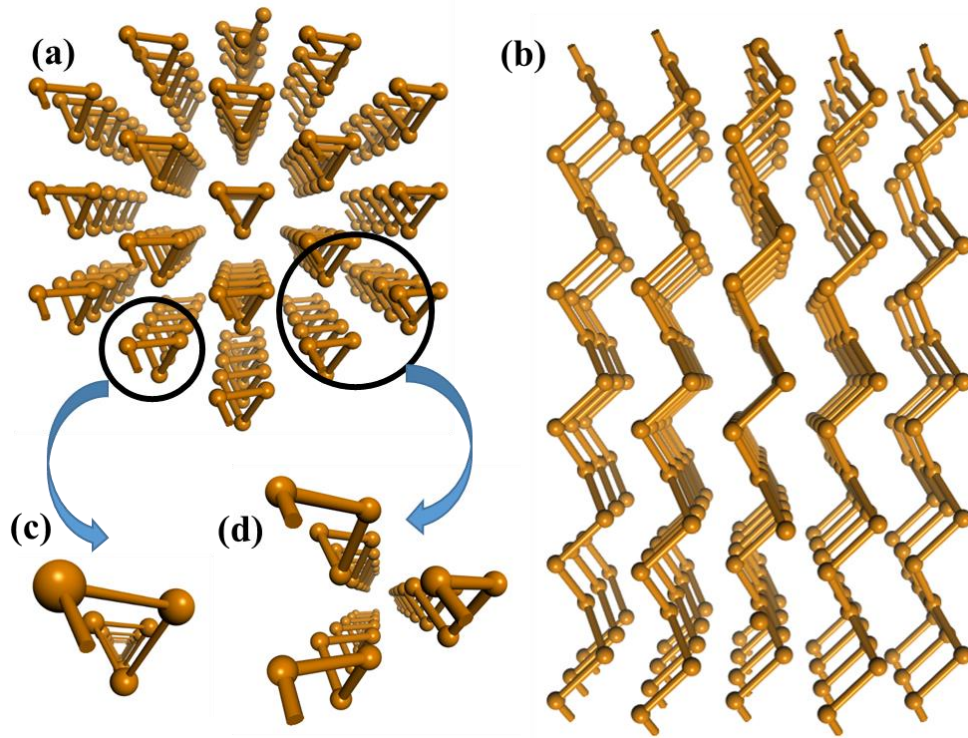


**Figure 7.1** The crystal structure of Te. (a) top and (b) side view of the crystal structure of bulk Te. (c) The structure of single Te chain. (d) The structure of Te three bundles.

## 7.2 Magnetism in Single Tellurium Chain

The DFT calculations are performed using the GGA with the PBE exchange-correlation functional [58] as implemented in the VASP code [40]. The PAW pseudopotential and plane-wave basis set with a cut-off energy of 500 eV is used. The structures are fully relaxed until the maximum residual force was smaller than 0.01 eV/Å and energies are converged to within  $1 \times 10^{-5}$  eV per atom. The Monkhorst-Pack k-point mesh is used with  $1 \times 1 \times 36$  k-points in the Brillouin zone. Because of the high atomic number and large electronic polarizability of tellurium, SOC is included in all calculations unless otherwise specified. The carrier density is regulated by the rigid-band approximations, which varies the total number of electrons in the unit cell, with a compensating jellium background of opposite charge added.

The band structure of the free-standing single tellurium chain is depicted in Fig. 7.2 (a). At the DFT level, the tellurium chain is a semiconductor with an indirect bandgap of 1.40 eV. The conduction band maximum (CBM) is located between the  $\Gamma$  and Z (Z') points, while the valence band minimum (VBM) is located near the zone boundary of the Z (Z') point. Because of the large atomic number of Te, SOC dictates the band structure: the bands including SOC, shown in black solid lines, are significantly splitted comparing with the bands without including SOC, which are shown in the red dashed lines.

Although the intrinsic Te chain is nonmagnetic, while both a small amount of electron and hole doping induce magnetism with a ferromagnetic ground state. Figure 7.3 shows the band structure of the electron-doped and hole-doped Te chain with doping density of 0.1/unit cell in the ferromagnetic state. In the ferromagnetic state, the spin-up and spin-down bands are split due to the exchange interaction, and  $s_z$  remains to be a good quantum number (here we choose the direction along the chain as the z axis). Thus, the electron or hole doped 1D Te chain is a half

metal: the states at the Fermi level are completely from one band of one spin type. In our calculations, within the hole density of 0.2 h/unit cell, the Fermi energy only intersects with a single spin-up/down band, making the doped 1D Te chain a perfect half metal allowing for fully polarized spin transport.

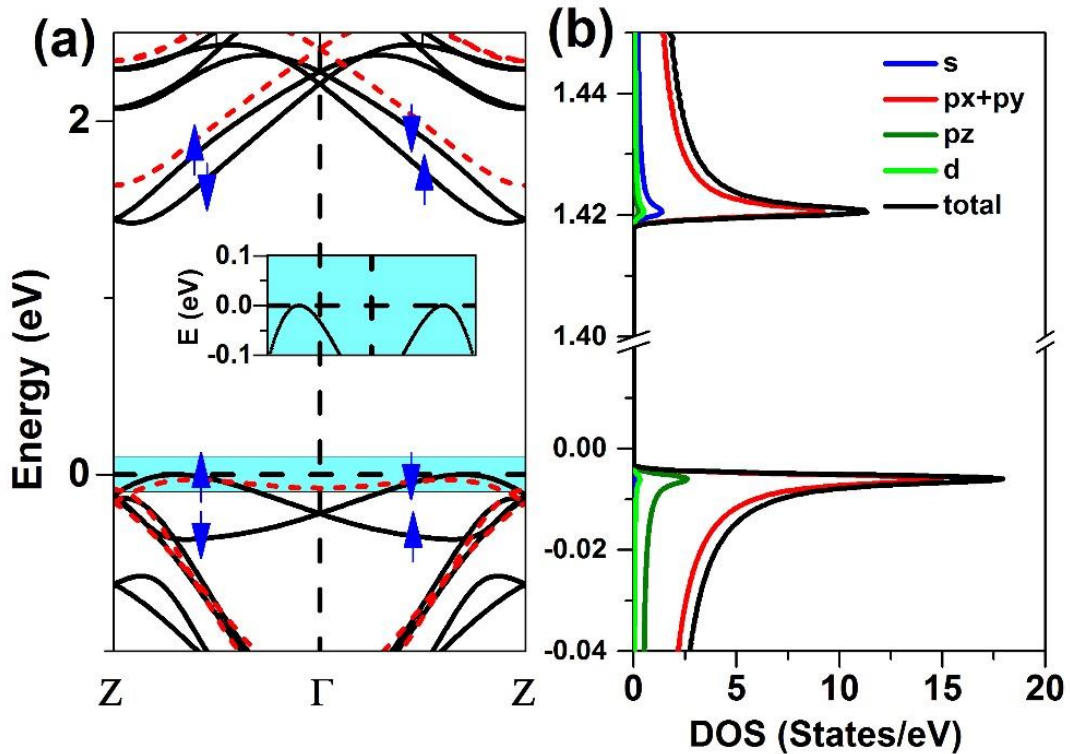


**Figure 7.2** (a) Electronic band structure of the intrinsic Te chain. The black solid and red short dashed line show the band structures with and without including SOC, respectively. The arrows represent the spin directions of the bands for a right-handed Te chain. (b) Total and partial density of states of the intrinsic Te chain near the band edges. A Gaussian broadening of 0.001 eV is used.

The doped induced magnetism is robust for a wide range of doping densities. Figure 7.4 shows the magnetic moment and spin polarization energy per carrier as a function of the electron and hole doping density. A large spin magnetic moment of nearly  $1 \mu_B$ /carrier quickly develops and saturates when the hole/electron doping density is larger than 0.01/unit cell. For hole doping, the

spin magnetic moment remains saturated up to doping density  $p = 0.25$  h/unit cell and then gradually drops to zero, as shown in Fig. 7.4(a), and a nonmagnetic state is restored when the doping density larger than  $p = 0.4$  h/unit cell. This doping density per atom is comparable with those found in 2D magnetic materials, such as GaSe, InP<sub>3</sub> and  $\alpha$ -SnO [168-170]. For electron doping, the range of the doping-induced magnetism is limited by the stability of 1D structures: after the doping density is greater than  $n = 0.1$  e/unit cell, the structure becomes unstable.

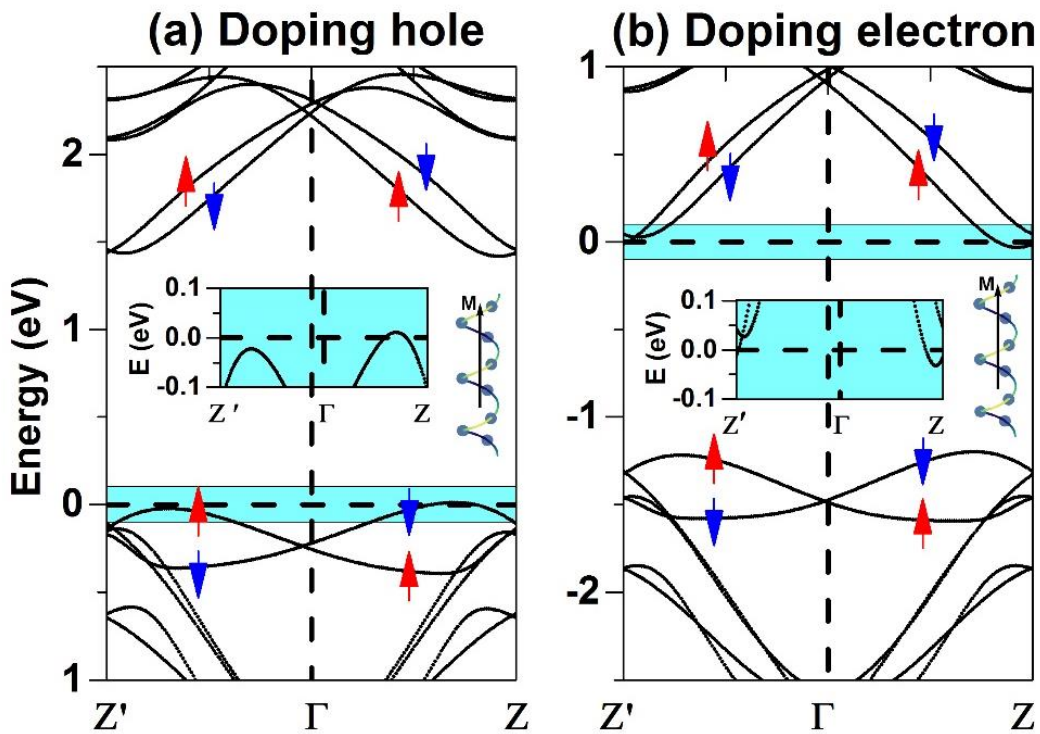


**Figure 7.3** Electronic band structure of Te chain with (a) hole doping of 0.1 h/unit cell and (b) electron doping of 0.1 e/unit cell, respectively. The Fermi level is set at zero. The insets show the band structures zoomed near the fermi level.

To study the stability of the ferromagnetic state, we also show in Figure 7.4 the spin polarization energy per carrier, defined as the energy difference between the ferromagnetic and nonmagnetic state divided by the carrier number. It has a much smaller window of saturation compared with

the magnetic momentum per carrier. For hole doping, the spin polarization energy per carrier gradually increases to 6 meV at  $p = 0.1$  h/unit cell, reaches a plateau, and then starts falling back above  $p = 0.2$  h/unit cell. For electron doping, the spin polarization energy per carrier gradually increases to 6 meV at  $n = 0.05$  e/unit cell, and then stays at the level below  $n = 0.1$  e/unit cell. Compared with 2D materials, these values are larger than that of monolayer GaSe and  $\alpha$ -SnO [168, 169], but smaller than InP<sub>3</sub> [170].

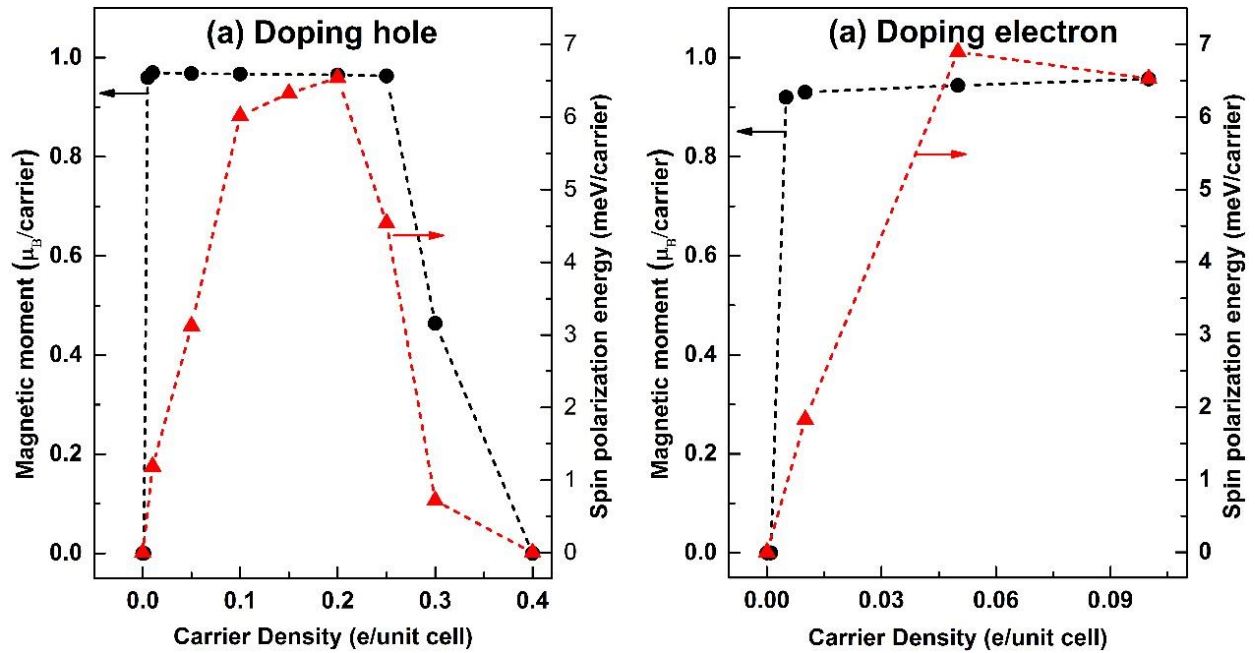


**Figure 7.4** Carrier density dependence of spin magnetic moment per carrier and spin polarization energy per carrier for (a) hole and (b) electron doping. Black circles and red triangles represent magnetic moment per carrier and spin-polarization energy per carrier, respectively. The short dash line is a guide to the eye.

The itinerant magnetism and half-metallicity of Te chain is driven by the exchange splitting between the opposite spin states. The splitting is proportional to the total magnetic momentum. At a carrier density of 0.1/unit cell, it is 34 meV at the VBM for hole-doping and 60 meV at the CBM for electron-doping. This splitting is equivalent to a Zeeman splitting under an external

magnetic field of 290 T for hole-doping and 520 T for electron-doping, assuming a spin  $g$  factor of 2 and no orbital contribution.

The origin of the ferromagnetism in 1D Te chains is the same as that of GNR as we discussed in Section 6.3 due to the following reasons. First, our calculation shows that  $d$  or  $f$  electronic states are not relevant here. As shown in Figure 7.2 (b), the partial DOS (PDOS) analysis represents the DOS near the CBM is mainly made up of  $p_x+p_y$  orbitals and small contribution from  $p_z$  orbitals, while the DOS near the VBM is also mainly composed of  $p_x+p_y$  orbitals, but small contribution from  $s$  and  $d$  orbitals are present as well. Therefore, the magnetism in the doped Te chain has a different origin.

Then, we check the DFT spin polarization energy against the Stoner model prediction. Te chain has an effective mass of 1.8 and a Stoner parameter of 0.2 eV·nm for hole doping, and an effective mass of 0.9 and a Stoner parameter of 0.33 eV·nm for electron doping. According to Eq. (6.4), we expect the spin polarization energy to be a parabolic function of the doping density, with the maximum value  $\Delta E_{max}^{Stoner} = 6$  meV occurring at  $n_{max}^{Stoner} = 0.14$  h/unit cell for hole doping, and  $\Delta E_{max}^{Stoner} = 8$  meV occurring at  $n_{max}^{Stoner} = 0.11$  e/unit cell for electron doping.

Although the electron side is inaccessible due to structural stability, the hole doping case shows an excellent agreement with the DFT results in Figure 7.4(a). This suggests that the magnetism we find in Te chain is due to the same quantum-confined Stoner mechanism as GNR.

This is also consistent with our calculation of multi-chain bundles. For a Te three-chain bundle (structure shown in Fig. 7.1(c)), where the electronic state is less confined, the ground state becomes nonmagnetic. Therefore, we expect to see the emergence of ferromagnetism as a result

of quantum confinement in tellurium as the material is thinned down close to the single-atomic chain.

### 7.3 Strong Magnetic Anisotropy

In addition to the robust ground state ferromagnetism, the heavy Te element grants strong SOC that exceeds most 1D electronic systems, which fixes the spin of the electron or hole along the chain by enhanced anisotropic magnetization energy. The direction of the magnetic momentum in the doped 1D Te chain is decided by the chirality of its helical chain structure. For example, when the doped electrons/holes occupy the positive crystal momentum in a right-handed chain, as shown in Fig. 7.3(a), its corresponding total magnetization direction is along the +z direction.

Within DFT, no (meta)stable ferromagnetic state can be found when we fix the spin magnetic moment perpendicular to the chain. In other words, the magnetic anisotropy energy in this material is even larger than its spin-polarization energy (6 meV), and thus the direction of the magnetic moment cannot freely rotate without breaking the magnetic order. By comparison, in conventional bulk and 2D magnetic materials, the magnetic anisotropic energy is usually no more than a few hundred  $\mu\text{eV}$ . To the best of our knowledge, such strong magnetic anisotropy has never been observed before.

In the following, we demonstrate how this strong magnetic anisotropy arises from the SOC with Stoner theory and tight-binding (TB) model. We assume the single-electron Hamiltonian to be  $\hat{H} = \hat{H}_{int} + \hat{H}_{SO} + \hat{H}_{stoner}$ , where  $\hat{H}_{int}$  is the TB Hamiltonian the intrinsic Te chain,  $\hat{H}_{SO}$  is the atomic spin-orbit term and  $\hat{H}_{stoner}$  is the Stoner term. The  $\hat{H}_{int}$  term is constructed with the nearest-neighbor Slater–Koster interatomic matrix elements [198] for Te p-orbitals that consists



of two parameters describing the  $\sigma$  and  $\pi$  bonding respectively. Additionally, the atomic SOC is included with  $\hat{H}_{SO} = \lambda \sum_i \mathbf{l}_i \cdot \mathbf{s}_i$ , where  $\lambda$  is the SOC parameter and sum goes over atoms  $i$ . The parameters are fitted to the DFT band structure, and the resulting TB band structure as shown in Fig. 7.5(a) captures the essential features from the DFT calculation, where the spin-orbit splitted bands are eigenstates of  $\hat{s}_z$ .

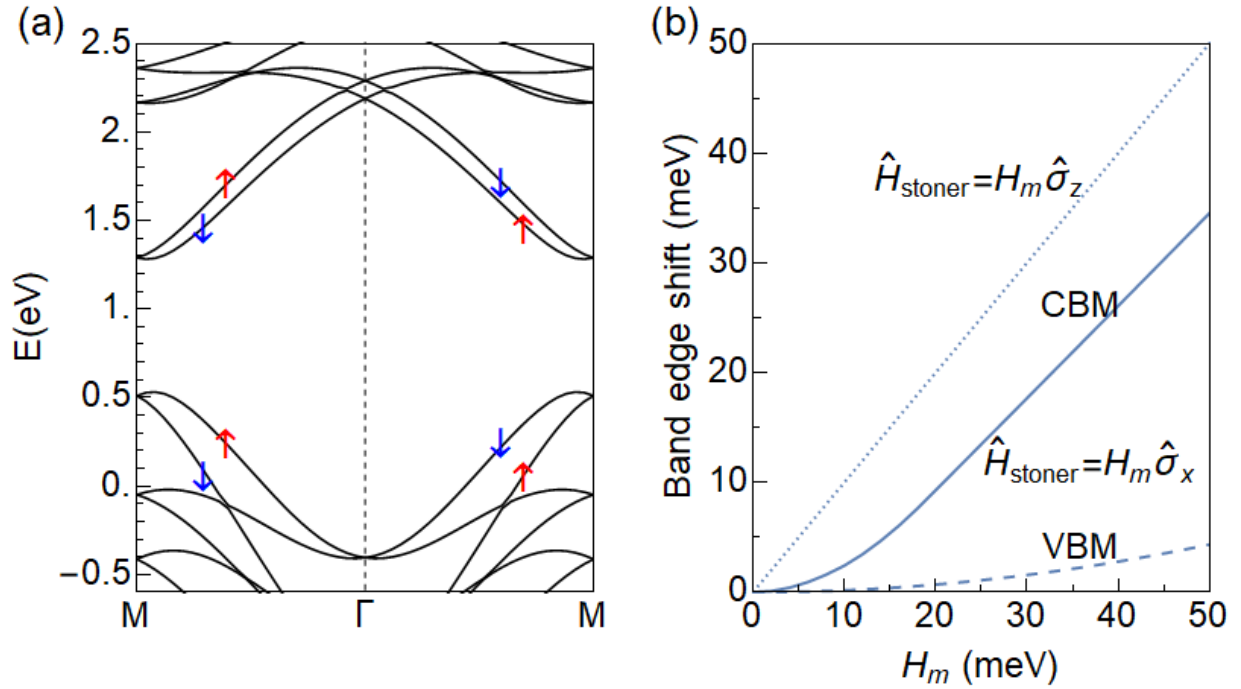


**Figure 7.5** (a) Band structure of Te chain from the tight-binding model described in the main text. (b) Shift in the VBM (dashed line) and CBM (solid line) energy versus the Stoner exchange splitting energy when the spin polarization is in the x-direction. The dotted line shows the linear band shift when the spin polarization is in the z-direction.

In the Stoner model, the magnetic exchange interaction is introduced by an effective magnetic field proportional to the total spin polarization, which leads to an exchange splitting energy of  $H_m = I(n_+ - n_-)$ . The field points toward the direction that lowers the energy of the majority spin, so the Stoner Hamiltonian can be written as  $\hat{H}_{stoner} = H_m \boldsymbol{\sigma} \cdot \hat{\mathbf{m}}$ , where  $\boldsymbol{\sigma}$  is the Pauli

matrices and  $\hat{\mathbf{m}}$  is the direction of the spin polarization. If the spin polarization is along the z-direction, and  $\hat{H}_{\text{Stoner}}$  simply shifts the band edge by  $\pm H_m$ , thus allowing the system to lower its total energy by moving all carriers into the lower band. However, if the spin polarization is in the perpendicular direction, then  $\hat{H}_{\text{Stoner}}$  does not change the energy of the bands under first-order perturbation. By solving the full Hamiltonian, it leads to a quadratic instead of linear shift of the band edge with respect to  $H_m$ , as shown in Fig. 7.5(b). Consequently, the gain in exchange energy is not enough to compensate the cost in kinetic energy. Therefore, there is no Stoner instability in the paramagnetic state towards the perpendicular direction, and the ferromagnetic state can only point along the chain direction.

## 7.4 Discussion

There are several unique advantages of the magnetism in the doped 1D Te chain. First, unlike previously predicted doping induced magnetism in 2D semiconductors, which can only realize magnetism by holes within a specific doping density [168-170], 1D Te chain can be half-metallic by either electron or hole doping in a wide range of doping density. This provides possibility for bipolar spintronics and more tunable degrees of freedom.

Second, the spin correlation at finite temperature can benefit from the strong magnetic anisotropy found in 1D Te chain. In a classical 1D anisotropic Heisenberg model, the spin correlation length grows as  $1/T$  at high temperature and grows exponentially as  $\exp(1/T)$  at low temperature, with the crossover temperature at  $\sqrt{E_{MAE}E_{sp}}/k_B$ , where  $E_{MAE}$  is the magnetic anisotropy energy and  $E_{sp}$  is the spin-polarization energy (or in terms of the Heisenberg model, the anisotropic and isotropic coupling constant) [173]. The huge magnetic anisotropy energy of Te chain will allow

for long-range 1D spin correlation at higher temperature, which is much desired for spintronic applications.

The coexistence of ferromagnetism, strong SOC and chiral chain structure also makes the 1D Te chain a potential candidate for realizing topological phenomena such as the Majorana zero mode [199, 200], where the Te chain has the advantage of having orders of magnitude larger SOC energy than the previously used InSb nanowire system [199]. Additionally, chiral chain structure with SOC, such as CNT and DNA, are also known to have the chiral-induced spin selectivity effect [201-203], where electrons have their spin selected to align or anti-align with their motion when transporting through the structure. With much stronger SOC than CNT and DNA, the 1D Te chain may not only show spin-selective, but also directional-dependent transport where the conductance is different when the current is going in opposite direction, as the signature of its half-metallic ferromagnetic ground state.

In conclusion, within first-principle DFT, we have shown that ferromagnetic ground state exists in both electron-doped and hole-doped 1D single-atomic tellurium chain. The magnetism is robust over a wide density range of over 0.1/unit cell and has spin polarization energy over 6 meV/carrier. Within Stoner theory, the magnetism is attributed to the large density of state and large Stoner parameter originated from the strong quantum confinement of the 1D structure. Furthermore, due to the strong SOC of tellurium and the helical chain structure, the magnetic state is highly anisotropic and only stable when the spin is pointing along the chain direction.



# References

- [1] K. S. Novoselov, A. K. Geim, S. V. Morozov, D. Jiang, Y. Zhang, S. V. Dubonos, I. V. Grigorieva and A. A. Firsov, "Electric Field Effect in Atomically Thin Carbon Films," *Science*, vol. 306, pp. 666-669, 2004.
- [2] C. Jin, F. Lin, K. Suenaga and S. Iijima, "Fabrication of a Freestanding Boron Nitride Single Layer and Its Defect Assignments," *Phys. Rev. Lett.*, vol. 102, p. 195505, 5 2009.
- [3] K. S. Novoselov, D. Jiang, F. Schedin, T. J. Booth, V. V. Khotkevich, S. V. Morozov and A. K. Geim, "Two-dimensional atomic crystals," *Proc Natl Acad Sci U S A*, vol. 102, p. 10451, 7 2005.
- [4] L. K. Li, Y. J. Yu, G. J. Ye, Q. Q. Ge, X. D. Ou, H. Wu, D. L. Feng, X. H. Chen and Y. B. Zhang, "Black phosphorus field-effect transistors," *Nature Nanotechnology*, vol. 9, pp. 372-377, 2014.
- [5] K. S. Novoselov, V. I. Fal'ko, L. Colombo, P. R. Gellert, M. G. Schwab and K. Kim, "A roadmap for graphene," *Nature*, vol. 490, pp. 192-200, 2012.
- [6] Q. H. Wang, K. Kalantar-Zadeh, A. Kis, J. N. Coleman and M. S. Strano, "Electronics and optoelectronics of two-dimensional transition metal dichalcogenides," *Nature Nanotechnology*, vol. 7, pp. 699-712, 2012.
- [7] W. Han, R. K. Kawakami, M. Gmitra and J. Fabian, "Graphene spintronics," *Nature Nanotechnology*, vol. 9, p. 794, 10 2014.
- [8] K. F. Mak and J. Shan, "Photonics and optoelectronics of 2D semiconductor transition metal dichalcogenides," *Nature Photonics*, vol. 10, pp. 216-226, 2016.
- [9] X. Xu, W. Yao, D. Xiao and T. F. Heinz, "Spin and pseudospins in layered transition metal dichalcogenides," *Nature Physics*, vol. 10, pp. 343-350, 2014.
- [10] J. R. Schaibley, H. Y. Yu, G. Clark, P. Rivera, J. S. Ross, K. L. Seyler, W. Yao and X. D. Xu, "Valleytronics in 2D materials," *Nature Reviews Materials*, vol. 1, 2016.
- [11] K. S. Novoselov, A. K. Geim, S. V. Morozov, D. Jiang, M. I. Katsnelson, I. V. Grigorieva, S. V. Dubonos and A. A. Firsov, "Two-dimensional gas of massless Dirac fermions in graphene," *Nature*, vol. 438, pp. 197-200, 2005.

- [12] C. L. Kane and E. J. Mele, "Quantum spin Hall effect in graphene," *Phys. Rev. Lett.*, vol. 95, 2005.
- [13] B. Huang, G. Clark, E. Navarro-Moratalla, D. R. Klein, R. Cheng, K. L. Seyler, D. Zhong, E. Schmidgall, M. A. McGuire, D. H. Cobden, W. Yao, D. Xiao, P. Jarillo-Herrero and X. D. Xu, "Layer-dependent ferromagnetism in a van der Waals crystal down to the monolayer limit," *Nature*, vol. 546, pp. 270-+, 2017.
- [14] C. Gong, L. Li, Z. L. Li, H. W. Ji, A. Stern, Y. Xia, T. Cao, W. Bao, C. Z. Wang, Y. A. Wang, Z. Q. Qiu, R. J. Cava, S. G. Louie, J. Xia and X. Zhang, "Discovery of intrinsic ferromagnetism in two-dimensional van der Waals crystals," *Nature*, vol. 546, pp. 265-+, 2017.
- [15] Z. Y. Fei, B. Huang, P. Malinowski, W. B. Wang, T. C. Song, J. Sanchez, W. Yao, D. Xiao, X. Y. Zhu, A. F. May, W. D. Wu, D. H. Cobden, J. H. Chu and X. D. Xu, "Two-dimensional itinerant ferromagnetism in atomically thin Fe<sub>3</sub>GeTe<sub>2</sub>," *Nature Materials*, vol. 17, pp. 778-+, 2018.
- [16] A. W. Tsen, R. Hovden, D. Wang, Y. D. Kim, J. Okamoto, K. A. Spoth, Y. Liu, W. J. Lu, Y. P. Sun, J. C. Hone, L. F. Kourkoutis, P. Kim and A. N. Pasupathy, "Structure and control of charge density waves in two-dimensional 1T-TaS<sub>2</sub>," *Proc Natl Acad Sci USA*, vol. 112, pp. 15054-15059, 2015.
- [17] X. X. Xi, L. Zhao, Z. F. Wang, H. Berger, L. Forro, J. Shan and K. F. Mak, "Strongly enhanced charge-density-wave order in monolayer NbSe<sub>2</sub>," *Nature Nanotechnology*, vol. 10, pp. 765-+, 2015.
- [18] J. C. W. Song and N. M. Gabor, "Electron quantum metamaterials in van der Waals heterostructures," *Nature Nanotechnology*, vol. 13, pp. 986-993, 11 2018.
- [19] K. S. Novoselov, A. Mishchenko, A. Carvalho and A. H. C. Neto, "2D materials and van der Waals heterostructures," *Science*, vol. 353, 2016.
- [20] M. M. Fogler, L. V. Butov and K. S. Novoselov, "High-temperature superfluidity with indirect excitons in van der Waals heterostructures," *Nature Communications*, vol. 5, 2014.
- [21] F. C. Wu, F. Xue and A. H. MacDonald, "Theory of two-dimensional spatially indirect equilibrium exciton condensates," *Phys. Rev. B*, vol. 92, 2015.
- [22] Y. Cao, V. Fatemi, A. Demir, S. Fang, S. L. Tomarken, J. Y. Luo, J. D. Sanchez-Yamagishi, K. Watanabe, T. Taniguchi, E. Kaxiras, R. C. Ashoori and P. Jarillo-Herrero,

- "Correlated insulator behaviour at half-filling in magic-angle graphene superlattices," *Nature*, vol. 556, pp. 80-+, 2018.
- [23] Y. Cao, V. Fatemi, S. Fang, K. Watanabe, T. Taniguchi, E. Kaxiras and P. Jarillo-Herrero, "Unconventional superconductivity in magic-angle graphene superlattices," *Nature*, vol. 556, pp. 43-+, 2018.
- [24] K. F. Mak, C. Lee, J. Hone, J. Shan and T. F. Heinz, "Atomically Thin MoS<sub>2</sub>: A New Direct-Gap Semiconductor," *Phys. Rev. Lett.*, vol. 105, 2010.
- [25] V. Tran, R. Soklaski, Y. Liang and L. Yang, "Layer-controlled band gap and anisotropic excitons in few-layer black phosphorus," *Phys. Rev. B*, vol. 89, no. 23, p. 235319, 6 2014.
- [26] D. Y. Qiu, F. H. Jornada and S. G. Louie, "Environmental Screening Effects in 2D Materials: Renormalization of the Bandgap, Electronic Structure, and Optical Spectra, of Few-Layer Black Phosphorus," *Nano Letters*, vol. 17, pp. 4706-4712, 2017.
- [27] P. Cudazzo, I. V. Tokatly and A. Rubio, "Dielectric screening in two-dimensional insulators: Implications for excitonic and impurity states in graphene," *Phys. Rev. B*, vol. 84, 2011.
- [28] F. Hüser, T. Olsen and K. S. Thygesen, "How dielectric screening in two-dimensional crystals affects the convergence of excited-state calculations: Monolayer MoS<sub>2</sub>," *Phys. Rev. B*, vol. 88, 2013.
- [29] F. A. Rasmussen, P. S. Schmidt, K. T. Winther and K. S. Thygesen, "Efficient many-body calculations for two-dimensional materials using exact limits for the screened potential: Band gaps of MoS<sub>2</sub>, h-BN, and phosphorene," *Phys. Rev. B*, vol. 94, 2016.
- [30] D. Y. Qiu, F. H. Jornada and S. G. Louie, "Screening and many-body effects in two-dimensional crystals: Monolayer MoS<sub>2</sub>," *Phys. Rev. B*, vol. 93, 2016.
- [31] F. H. Jornada, D. Y. Qiu and S. G. Louie, "Nonuniform sampling schemes of the Brillouin zone for many-electron perturbation-theory calculations in reduced dimensionality," *Phys. Rev. B*, vol. 95, 2017.
- [32] R. M. Martin, L. Reining and D. M. Ceperley, *Interacting Electrons: Theory and Computational Approaches*, Cambridge University Press, 2016.

- [33] G. Onida, L. Reining and A. Rubio, "Electronic excitations: density-functional versus many-body Green's-function approaches," *Rev. Mod. Phys.*, vol. 74, no. 2, pp. 601-659, 6 2002.
- [34] P. Hohenberg and W. Kohn, "Inhomogeneous Electron Gas," *Phys. Rev.*, vol. 136, pp. B864--B871, 11 1964.
- [35] W. Kohn and L. J. Sham, "Self-Consistent Equations Including Exchange and Correlation Effects," *Phys. Rev.*, vol. 140, pp. A1133--A1138, 11 1965.
- [36] R. M. Martin, *Electronic structure: basic theory and practical methods*, Cambridge University Press, 2004.
- [37] N. Schuch and F. Verstraete, "Computational complexity of interacting electrons and fundamental limitations of density functional theory," *Nature Physics*, vol. 5, pp. 732-735, 2009.
- [38] J. P. Perdew and K. Schmidt, "Density Functional Theory and its Application to Materials," in *AIP Conference Proceedings*, 2001.
- [39] P. Giannozzi and others, "QUANTUM ESPRESSO: a modular and open-source software project for quantum simulations of materials," *Journal of Physics: Condensed Matter*, vol. 21, p. 395502 (19pp), 2009.
- [40] H. Jürgen, "Ab-initio simulations of materials using VASP: Density-functional theory and beyond," *J. Comput. Chem.*, vol. 29, pp. 2044-2078, 6 2008.
- [41] W. H. Dickhoff and D. Van Neck, *Many-body theory exposed!: propagator description of quantum mechanics in many-body systems*, World Scientific, 2008.
- [42] L. Hedin, "New Method for Calculating the One-Particle Green's Function with Application to the Electron-Gas Problem," *Phys. Rev.*, vol. 139, no. 3A, pp. A796--A823, 8 1965.
- [43] M. S. Hybertsen and S. G. Louie, "Electron correlation in semiconductors and insulators: Band gaps and quasiparticle energies," *Phys. Rev. B*, vol. 34, no. 8, pp. 5390-5413, 10 1986.
- [44] J. Deslippe, G. Samsonidze, D. A. Strubbe, M. Jain, M. L. Cohen and S. G. Louie, "BerkeleyGW: A massively parallel computer package for the calculation of the



quasiparticle and optical properties of materials and nanostructures," *Computer Physics Communications*, vol. 183, pp. 1269-1289, 2012.

- [45] M. Rohlfing and S. G. Louie, "Electron-hole excitations and optical spectra from first principles," *Phys. Rev. B*, vol. 62, no. 8, pp. 4927-4944, 8 2000.
- [46] C. D. Spataru, S. Ismail-Beigi, L. X. Benedict and S. G. Louie, "Excitonic effects and optical spectra of single-walled carbon nanotubes," *Phys. Rev. Lett.*, vol. 92, 2004.
- [47] K. F. Mak, K. He, C. Lee, G. H. Lee, J. Hone, T. F. Heinz and J. Shan, "Tightly bound trions in monolayer MoS<sub>2</sub>," *Nature Materials*, vol. 12, pp. 207-211, 2013.
- [48] S. Mouri, Y. Miyauchi and K. Matsuda, "Tunable photoluminescence of monolayer MoS<sub>2</sub> via chemical doping," *Nano Letters*, vol. 13, pp. 5944-5948, 2013.
- [49] Y. Zhang, T.-R. Chang, B. Zhou, Y.-T. Cui, H. Yan, Z. Liu, F. Schmitt, J. Lee, R. Moore, Y. Chen and others, "Direct observation of the transition from indirect to direct bandgap in atomically thin epitaxial MoSe<sub>2</sub>," *Nature Nanotechnology*, vol. 9, pp. 111-115, 2014.
- [50] C. D. Spataru and F. Léonard, "Tunable Band Gaps and Excitons in Doped Semiconducting Carbon Nanotubes Made Possible by Acoustic Plasmons," *Phys. Rev. Lett.*, vol. 104, no. 17, p. 177402, 4 2010.
- [51] C. D. Spataru and F. Léonard, "Quasiparticle and exciton renormalization effects in electrostatically doped semiconducting carbon nanotubes," *Chemical Physics*, vol. 413, pp. 81-88, 2013.
- [52] Y. Liang and L. Yang, "Carrier Plasmon Induced Nonlinear Band Gap Renormalization in Two-Dimensional Semiconductors," *Phys. Rev. Lett.*, vol. 114, no. 6, p. 063001, 2 2015.
- [53] S. Larentis, J. R. Tolsma, B. Fallahazad, D. C. Dillen, K. Kim, A. H. MacDonald and E. Tutuc, "Band Offset and Negative Compressibility in Graphene-MoS<sub>2</sub> Heterostructures," *Nano Letters*, vol. 14, pp. 2039-2045, 2014.
- [54] J. M. Riley, W. Meevasana, L. Bawden, M. Asakawa, T. Takayama, T. Eknapakul, T. K. Kim, M. Hoesch, S.-K. Mo, H. Takagi and others, "Negative electronic compressibility and tunable spin splitting in WSe<sub>2</sub>," *Nat Nano*, vol. 10, pp. 1043-1047, 12 2015.
- [55] A. Chernikov, C. Ruppert, H. M. Hill, A. F. Rigosi and T. F. Heinz, "Population inversion and giant bandgap renormalization in atomically thin WS<sub>2</sub> layers," *Nature Photonics*, vol. 9, pp. 466-U69, 2015.

- [56] E. A. A. Pogna, M. Marsili, D. D. Fazio, S. D. Conte, C. Manzoni, D. Sangalli, D. Yoon, A. Lombardo, A. C. Ferrari, A. Marini, G. Cerullo and D. Prezzi, "Photo-Induced Bandgap Renormalization Governs the Ultrafast Response of Single-Layer MoS<sub>2</sub>," *ACS Nano*, vol. 10, pp. 1182-1188, 1 2016.
- [57] K. Yao, A. Yan, S. Kahn, A. Suslu, Y. Liang, E. S. Barnard, S. Tongay, A. Zettl, N. J. Borys and P. J. Schuck, "Optically Discriminating Carrier-Induced Quasiparticle Band Gap and Exciton Energy Renormalization in Monolayer MoS<sub>2</sub>," *Phys. Rev. Lett.*, vol. 119, p. 087401, 8 2017.
- [58] J. P. Perdew, K. Burke and M. Ernzerhof, "Generalized Gradient Approximation Made Simple," *Phys. Rev. Lett.*, vol. 77, no. 18, pp. 3865-3868, 10 1996.
- [59] S. Ismail-Beigi, "Truncation of periodic image interactions for confined systems," *Phys. Rev. B*, vol. 73, no. 23, p. 233103, 6 2006.
- [60] A. K. Geim and I. V. Grigorieva, "Van der Waals heterostructures," *Nature*, vol. 499, pp. 419-425, 2013.
- [61] G. Giuliani and G. Vignale, Quantum theory of the electron liquid, Cambridge university press, 2005.
- [62] A. Czacor, A. Holas, S. R. Sharma and K. S. Singwi, "Dynamical Correlations in a Two-Dimensional Electron-Gas - 1st-Order Perturbation-Theory," *Phys. Rev. B*, vol. 25, pp. 2144-2159, 1982.
- [63] F. N. Xia, H. Wang and Y. C. Jia, "Rediscovering black phosphorus as an anisotropic layered material for optoelectronics and electronics," *Nature Communications*, vol. 5, 2014.
- [64] H. Liu, A. T. Neal, Z. Zhu, Z. Luo, X. F. Xu, D. Tomanek and P. D. Ye, "Phosphorene: An Unexplored 2D Semiconductor with a High Hole Mobility," *ACS Nano*, vol. 8, pp. 4033-4041, 2014.
- [65] J. Kim, S. S. Baik, S. H. Ryu, Y. Sohn, S. Park, B. G. Park, J. Denlinger, Y. Yi, H. J. Choi and K. S. Kim, "Observation of tunable band gap and anisotropic Dirac semimetal state in black phosphorus," *Science*, vol. 349, pp. 723-726, 2015.
- [66] R. X. Fei and L. Yang, "Strain-Engineering the Anisotropic Electrical Conductance of Few-Layer Black Phosphorus," *Nano Letters*, vol. 14, pp. 2884-2889, 2014.

- [67] R. X. Fei, A. Faghaninia, R. Soklaski, J. A. Yan, C. Lo and L. Yang, "Enhanced Thermoelectric Efficiency via Orthogonal Electrical and Thermal Conductances in Phosphorene," *Nano Letters*, vol. 14, pp. 6393-6399, 2014.
- [68] T. Low, R. Roldan, H. Wang, F. N. Xia, P. Avouris, L. M. Moreno and F. Guinea, "Plasmons and Screening in Monolayer and Multilayer Black Phosphorus," *Phys. Rev. B*, vol. 113, 2014.
- [69] S. Yang, S. Tongay, Y. Li, Q. Yue, J.-B. Xia, S.-S. Li, J. Li and S.-H. Wei, "Layer-dependent electrical and optoelectronic responses of ReSe<sub>2</sub> nanosheet transistors," *Nanoscale*, vol. 6, pp. 7226-7231, 2014.
- [70] D. Wolverson, S. Crampin, A. S. Kazemi, A. Ilie and S. J. Bending, "Raman Spectra of Monolayer, Few-Layer, and Bulk ReSe<sub>2</sub>: An Anisotropic Layered Semiconductor," *ACS Nano*, vol. 8, pp. 11154-11164, 11 2014.
- [71] H.-X. Zhong, S. Gao, J.-J. Shi and L. Yang, "Quasiparticle band gaps, excitonic effects, and anisotropic optical properties of the monolayer distorted 1T diamond-chain structures ReS<sub>2</sub> and ReSe<sub>2</sub>," *Phys. Rev. B*, vol. 92, p. 115438, 9 2015.
- [72] Z. Qiu, M. Trushin, H. Fang, I. Verzhbitskiy, S. Gao, E. Laksono, M. Yang, P. Lyu, J. Li, J. Su, M. Telychko, K. Watanabe, T. Taniguchi, J. Wu, A. H. C. Neto, L. Yang, G. Eda, S. Adam and J. Lu, "Giant gate-tunable excitonic effects in a 2D semiconductor," *submitted article*, 2018.
- [73] E. H. Hwang and S. Das Sarma, "Dielectric function, screening, and plasmons in two-dimensional graphene," *Phys. Rev. B*, vol. 75, no. 20, p. 205418, 5 2007.
- [74] L. Yang, J. Deslippe, C.-H. Park, M. L. Cohen and S. G. Louie, "Excitonic Effects on the Optical Response of Graphene and Bilayer Graphene," *Phys. Rev. Lett.*, vol. 103, no. 18, p. 186802, 10 2009.
- [75] L. Yang, "Excitons in intrinsic and bilayer graphene," *Phys. Rev. B*, vol. 83, no. 8, p. 085405, 2 2011.
- [76] M. M. Ugeda, A. J. Bradley, S.-F. Shi, H. Felipe, Y. Zhang, D. Y. Qiu, W. Ruan, S.-K. Mo, Z. Hussain, Z.-X. Shen and others, "Giant bandgap renormalization and excitonic effects in a monolayer transition metal dichalcogenide semiconductor," *Nature Materials*, 2014.
- [77] A. Chernikov, T. C. Berkelbach, H. M. Hill, A. Rigosi, Y. Li, O. B. Aslan, D. R. Reichman, M. S. Hybertsen and T. F. Heinz, "Exciton Binding Energy and

- Nonhydrogenic Rydberg Series in Monolayer WS<sub>2</sub>," *Phys. Rev. Lett.*, vol. 113, no. 7, p. 076802, 8 2014.
- [78] K. He, N. Kumar, L. Zhao, Z. Wang, K. F. Mak, H. Zhao and J. Shan, "Tightly Bound Excitons in Monolayer WSe<sub>2</sub>," *Phys. Rev. Lett.*, vol. 113, no. 2, p. 026803, 7 2014.
- [79] A. Ramasubramaniam, "Large excitonic effects in monolayers of molybdenum and tungsten dichalcogenides," *Phys. Rev. B*, vol. 86, no. 11, p. 115409, 9 2012.
- [80] D. Y. Qiu, F. H. Jornada and S. G. Louie, "Optical Spectrum of MoS<sub>2</sub>: Many-Body Effects and Diversity of Exciton States," *Phys. Rev. Lett.*, vol. 111, no. 21, p. 216805, 11 2013.
- [81] X. Wang, A. M. Jones, K. L. Seyler, V. Tran, Y. Jia, H. Zhao, H. Wang, L. Yang, X. Xu and F. Xia, "Highly anisotropic and robust excitons in monolayer black phosphorus," *Nature Nanotechnology*, vol. 10, pp. 517-521, 2015.
- [82] A. M. Jones, H. Yu, N. J. Ghimire, S. Wu, G. Aivazian, J. S. Ross, B. Zhao, J. Yan, D. G. Mandrus, D. Xiao and others, "Optical generation of excitonic valley coherence in monolayer WSe<sub>2</sub>," *Nature Nanotechnology*, vol. 8, pp. 634-638, 2013.
- [83] J. S. Ross, S. Wu, H. Yu, N. J. Ghimire, A. M. Jones, G. Aivazian, J. Yan, D. G. Mandrus, D. Xiao, W. Yao and others, "Electrical control of neutral and charged excitons in a monolayer semiconductor," *Nature Communications*, vol. 4, p. 1474, 2013.
- [84] G. Plechinger, P. Nagler, J. Kraus, N. Paradiso, C. Strunk, C. Schüller and T. Korn, "Identification of excitons, trions and biexcitons in single-layer WS<sub>2</sub>," *physica status solidi (RRL) - Rapid Research Letters*, vol. 9, pp. 457-461, 2015.
- [85] J. Shang, X. Shen, C. Cong, N. Peimyoo, B. Cao, M. Eginligil and T. Yu, "Observation of Excitonic Fine Structure in a 2D Transition-Metal Dichalcogenide Semiconductor," *ACS Nano*, vol. 9, pp. 647-655, 2015.
- [86] A. Chernikov, A. M. Zande, H. M. Hill, A. F. Rigosi, A. Velauthapillai, J. Hone and T. F. Heinz, "Electrical Tuning of Exciton Binding Energies in Monolayer WS<sub>2</sub>," *Phys. Rev. Lett.*, vol. 115, no. 12, p. 126802, 9 2015.
- [87] T. Eknapakul, P. D. C. King, M. Asakawa, P. Buaphet, R.-H. He, S.-K. Mo, H. Takagi, K. M. Shen, F. Baumberger, T. Sasagawa and others, "Electronic structure of a quasi-freestanding MoS<sub>2</sub> monolayer," *Nano Letters*, vol. 14, pp. 1312-1316, 2014.

- [88] A. E. Ruckenstein and S. Schmitt-Rink, "Many-body aspects of the optical spectra of bulk and low-dimensional doped semiconductors," *Phys. Rev. B*, vol. 35, no. 14, pp. 7551-7557, 5 1987.
- [89] P. Hawrylak, "Optical properties of a two-dimensional electron gas: Evolution of spectra from excitons to Fermi-edge singularities," *Phys. Rev. B*, vol. 44, no. 8, pp. 3821-3828, 8 1991.
- [90] G. E. W. Bauer, "Excitons in the quasi-two-dimensional electron gas," *Phys. Rev. B*, vol. 45, no. 16, pp. 9153-9162, 4 1992.
- [91] T. C. Berkelbach, M. S. Hybertsen and D. R. Reichman, "Theory of neutral and charged excitons in monolayer transition metal dichalcogenides," *Phys. Rev. B*, vol. 88, no. 4, p. 045318, 7 2013.
- [92] M. Z. Mayers, T. C. Berkelbach, M. S. Hybertsen and D. R. Reichman, "Binding energies and spatial structures of small carrier complexes in monolayer transition-metal dichalcogenides via diffusion Monte Carlo," *Phys. Rev. B*, vol. 92, no. 16, p. 161404, 10 2015.
- [93] K. A. Velizhanin and A. Saxena, "Excitonic effects in two-dimensional semiconductors: Path integral Monte Carlo approach," *Phys. Rev. B*, vol. 92, no. 19, p. 195305, 11 2015.
- [94] F. Cadiz, E. Courtade, C. Robert, G. Wang, Y. Shen, H. Cai, T. Taniguchi, K. Watanabe, H. Carrere, D. Lagarde, M. Manca, T. Amand, P. Renucci, S. Tongay, X. Marie and B. Urbaszek, "Excitonic Linewidth Approaching the Homogeneous Limit in MoS<sub>2</sub>-Based van der Waals Heterostructures," *Phys. Rev. X*, vol. 7, p. 021026, 5 2017.
- [95] E. Burstein, "Anomalous Optical Absorption Limit in InSb," *Phys. Rev.*, vol. 93, pp. 632-633, 2 1954.
- [96] T. S. Moss, "The Interpretation of the Properties of Indium Antimonide," *Proceedings of the Physical Society. Section B*, vol. 67, p. 775, 1954.
- [97] J. B. Neaton, M. S. Hybertsen and S. G. Louie, "Renormalization of Molecular Electronic Levels at Metal-Molecule Interfaces," *Phys. Rev. Lett.*, vol. 97, no. 21, p. 216405, 11 2006.
- [98] H.-P. Komsa and A. V. Krasheninnikov, "Effects of confinement and environment on the electronic structure and exciton binding energy of MoS<sub>2</sub> from first principles," *Phys. Rev. B*, vol. 86, no. 24, p. 241201, 12 2012.

- [99] S. Latini, T. Olsen and K. S. Thygesen, "Excitons in van der Waals heterostructures: The important role of dielectric screening," *Phys. Rev. B*, vol. 92, p. 245123, 12 2015.
- [100] J. M. Riley, W. Meevasana, L. Bawden, M. Asakawa, T. Takayama, T. Eknapakul, T. K. Kim, M. Hoesch, S. K. Mo, H. Takagi, T. Sasagawa, M. S. Bahramy and P. D. C. King, "Negative electronic compressibility and tunable spin splitting in WSe<sub>2</sub>," *Nature Nanotechnology*, vol. 10, pp. 1043-+, 2015.
- [101] B. Fallahazad, H. C. P. Movva, K. Kim, S. Larentis, T. Taniguchi, K. Watanabe, S. K. Banerjee and E. Tutuc, "Shubnikov-de Haas Oscillations of High-Mobility Holes in Monolayer and Bilayer WSe<sub>2</sub>: Landau Level Degeneracy, Effective Mass, and Negative Compressibility," *Phys. Rev. Lett.*, vol. 116, no. 8, p. 086601, 2 2016.
- [102] G. Strinati, "Dynamical Shift and Broadening of Core Excitons in Semiconductors," *Phys. Rev. Lett.*, vol. 49, no. 20, pp. 1519-1522, 11 1982.
- [103] G. Strinati, "Effects of dynamical screening on resonances at inner-shell thresholds in semiconductors," *Phys. Rev. B*, vol. 29, no. 10, pp. 5718-5726, 5 1984.
- [104] F. Caruso, H. Lambert and F. Giustino, "Band Structures of Plasmonic Polarons," *Phys. Rev. Lett.*, vol. 114, no. 14, p. 146404, 4 2015.
- [105] J. Lischner, D. Vigil-Fowler and S. G. Louie, "Physical Origin of Satellites in Photoemission of Doped Graphene: An GW Plus Cumulant Study," *Phys. Rev. Lett.*, vol. 110, no. 14, p. 146801, 4 2013.
- [106] J. S. Zhou, J. J. Kas, L. Sponza, I. Reshetnyak, M. Guzzo, C. Giorgetti, M. Gatti, F. Sottile, J. J. Rehr and L. Reining, "Dynamical effects in electron spectroscopy," *The Journal of Chemical Physics*, vol. 143, 2015.
- [107] F. X. Bronold, "Absorption spectrum of a weakly n-doped semiconductor quantum well," *Phys. Rev. B*, vol. 61, no. 19, pp. 12620-12623, 5 2000.
- [108] R. A. Suris, V. P. Kochereshko, G. V. Astakhov, D. R. Yakovlev, W. Ossau, J. Nürnberger, W. Faschinger, G. Landwehr, T. Wojtowicz, G. Karczewski and J. Kossut, "Excitons and Trions Modified by Interaction with a Two-Dimensional Electron Gas," *phys. stat. sol. (b)*, vol. 227, pp. 343-352, 2001.
- [109] A. Marini and R. Del Sole, "Dynamical Excitonic Effects in Metals and Semiconductors," *Phys. Rev. Lett.*, vol. 91, no. 17, p. 176402, 10 2003.

- [110] J. E. Northrup, M. S. Hybertsen and S. G. Louie, "Quasiparticle excitation spectrum for nearly-free-electron metals," *Phys. Rev. B*, vol. 39, no. 12, pp. 8198-8208, 4 1989.
- [111] J. Deslippe, G. Samsonidze, M. Jain, M. L. Cohen and S. G. Louie, "Coulomb-hole summations and energies for GW calculations with limited number of empty orbitals: A modified static remainder approach," *Phys. Rev. B*, vol. 87, no. 16, p. 165124, 4 2013.
- [112] W. Gao, X. Gao, T. A. Abtey, Y.-Y. Sun, S. Zhang and P. Zhang, "Quasiparticle band gap of organic-inorganic hybrid perovskites: Crystal structure, spin-orbit coupling, and self-energy effects," *Phys. Rev. B*, vol. 93, no. 8, p. 085202, 2 2016.
- [113] M. Cardona and M. L. W. Thewalt, "Isotope effects on the optical spectra of semiconductors," *Rev. Mod. Phys.*, vol. 77, pp. 1173-1224, 11 2005.
- [114] B. Chakraborty, A. Bera, D. V. S. Muthu, S. Bhowmick, U. V. Waghmare and A. K. Sood, "Symmetry-dependent phonon renormalization in monolayer MoS<sub>2</sub> transistor," *Phys. Rev. B*, vol. 85, p. 161403, 4 2012.
- [115] A. Miglio, D. Waroquiers, G. Antonius, M. Giantomassi, M. Stankovski, M. Côté, X. Gonze and G. M. Rignanese, "Effects of plasmon pole models on the G0W0 electronic structure of various oxides," *The European Physical Journal B*, vol. 85, p. 322, 9 2012.
- [116] K. Kheng, R. T. Cox, M. Y. Aubigné, F. Bassani, K. Saminadayar and S. Tatarenko, "Observation of negatively charged excitons X<sup>-</sup> in semiconductor quantum wells," *Phys. Rev. Lett.*, vol. 71, no. 11, pp. 1752-1755, 9 1993.
- [117] S. A. Brown, J. F. Young, J. A. Brum, P. Hawrylak and Z. Wasilewski, "Evolution of the interband absorption threshold with the density of a two-dimensional electron gas," *Phys. Rev. B*, vol. 54, no. 16, pp. R11082--R11085, 10 1996.
- [118] V. Huard, R. T. Cox, K. Saminadayar, A. Arnoult and S. Tatarenko, "Bound States in Optical Absorption of Semiconductor Quantum Wells Containing a Two-Dimensional Electron Gas," *Phys. Rev. Lett.*, vol. 84, no. 1, pp. 187-190, 1 2000.
- [119] G. Yusa, H. Shtrikman and I. Bar-Joseph, "Onset of exciton absorption in modulation-doped GaAs quantum wells," *Phys. Rev. B*, vol. 62, no. 23, pp. 15390-15393, 12 2000.
- [120] G. G. Spink, P. López Ríos, N. D. Drummond and R. J. Needs, "Trion formation in a two-dimensional hole-doped electron gas," *Phys. Rev. B*, vol. 94, no. 4, p. 041410, 7 2016.

- [121] F. Bechstedt, K. Tenelsen, B. Adolph and R. Del Sole, "Compensation of Dynamical Quasiparticle and Vertex Corrections in Optical Spectra," *Phys. Rev. Lett.*, vol. 78, no. 8, pp. 1528-1531, 2 1997.
- [122] L. Yang, "Excitonic effects on optical absorption spectra of doped graphene," *Nano Letters*, vol. 11, pp. 3844-3847, 2011.
- [123] K. F. Mak, F. H. Jornada, K. He, J. Deslippe, N. Petrone, J. Hone, J. Shan, S. G. Louie and T. F. Heinz, "Tuning Many-Body Interactions in Graphene: The Effects of Doping on Excitons and Carrier Lifetimes," *Phys. Rev. Lett.*, vol. 112, no. 20, p. 207401, 5 2014.
- [124] X. P. Hong, J. Kim, S. F. Shi, Y. Zhang, C. H. Jin, Y. H. Sun, S. Tongay, J. Q. Wu, Y. F. Zhang and F. Wang, "Ultrafast charge transfer in atomically thin MoS<sub>2</sub>/WS<sub>2</sub> heterostructures," *Nature Nanotechnology*, vol. 9, pp. 682-686, 2014.
- [125] M. Bernardi, M. Palummo and J. C. Grossman, "Extraordinary Sunlight Absorption and One Nanometer Thick Photovoltaics Using Two-Dimensional Monolayer Materials," *Nano Letters*, vol. 13, pp. 3664-3670, 2013.
- [126] P. Rivera, J. R. Schaibley, A. M. Jones, J. S. Ross, S. F. Wu, G. Aivazian, P. Klement, K. Seyler, G. Clark, N. J. Ghimire, J. Q. Yan, D. G. Mandrus, W. Yao and X. D. Xu, "Observation of long-lived interlayer excitons in monolayer MoSe<sub>2</sub>-WSe<sub>2</sub> heterostructures," *Nature Communications*, vol. 6, 2015.
- [127] M. H. Chiu, M. Y. Li, W. J. Zhang, W. T. Hsu, W. H. Chang, M. Terrones, H. Terrones and L. J. Li, "Spectroscopic Signatures for Interlayer Coupling in MoS<sub>2</sub>-WSe<sub>2</sub> van der Waals Stacking," *ACS Nano*, vol. 8, pp. 9649-9656, 2014.
- [128] H. Fang, C. Battaglia, C. Carraro, S. Nemsak, B. Ozdol, J. S. Kang, H. A. Bechtel, S. B. Desai, F. Kronast, A. A. Unal, G. Conti, C. Conlon, G. K. Palsson, M. C. Martin, A. M. Minor, C. S. Fadley, E. Yablonovitch, R. Maboudian and A. Javey, "Strong interlayer coupling in van der Waals heterostructures built from single-layer chalcogenides," *Proc Natl Acad Sci USA*, vol. 111, pp. 6198-6202, 2014.
- [129] A. F. Rigos, H. M. Hill, Y. L. Li, A. Chernikov and T. F. Heinz, "Probing Interlayer Interactions in Transition Metal Dichalcogenide Heterostructures by Optical Spectroscopy: MoS<sub>2</sub>/WS<sub>2</sub> and MoSe<sub>2</sub>/WSe<sub>2</sub>," *Nano Letters*, vol. 15, pp. 5033-5038, 2015.
- [130] Y. Yu, S. Hu, L. Su, L. Huang, Y. Liu, Z. Jin, A. A. Purezky, D. B. Geohegan, K. W. Kim, Y. Zhang and L. Cao, "Equally Efficient Interlayer Exciton Relaxation and



- Improved Absorption in Epitaxial and Nonepitaxial MoS<sub>2</sub>/WS<sub>2</sub> Heterostructures," *Nano Lett.*, vol. 15, pp. 486-491, 1 2015.
- [131] D. A. B. Miller, D. S. Chemla, T. C. Damen, A. C. Gossard, W. Wiegmann, T. H. Wood and C. A. Burrus, "Band-Edge Electroabsorption in Quantum Well Structures - the Quantum-Confined Stark-Effect," *Phys. Rev. Lett.*, vol. 53, pp. 2173-2176, 1984.
- [132] H. P. Komsa and A. V. Krasheninnikov, "Electronic structures and optical properties of realistic transition metal dichalcogenide heterostructures from first principles," *Phys. Rev. B*, vol. 88, 2013.
- [133] M. Palummo, M. Bernardi and J. C. Grossman, "Exciton Radiative Lifetimes in Two-Dimensional Transition Metal Dichalcogenides," *Nano Letters*, vol. 15, pp. 2794-2800, 2015.
- [134] X. Y. Zhu, N. R. Monahan, Z. Z. Gong, H. M. Zhu, K. W. Williams and C. A. Nelson, "Charge Transfer Excitons at van der Waals Interfaces," *Journal of the American Chemical Society*, vol. 137, pp. 8313-8320, 2015.
- [135] S. Grimme, "Semiempirical GGA-type density functional constructed with a long-range dispersion correction," *J. Comput. Chem.*, vol. 27, pp. 1787-1799, 11 2006.
- [136] V. Barone, M. Casarin, D. Forrer, M. Pavone, M. Sami and A. Vittadini, "Role and Effective Treatment of Dispersive Forces in Materials: Polyethylene and Graphite Crystals as Test Cases," *Journal of Computational Chemistry*, vol. 30, pp. 934-939, 2009.
- [137] Y. J. Gong, J. H. Lin, X. L. Wang, G. Shi, S. D. Lei, Z. Lin, X. L. Zou, G. L. Ye, R. Vajtai, B. I. Yakobson, H. Terrones, M. Terrones, B. K. Tay, J. Lou, S. T. Pantelides, Z. Liu, W. Zhou and P. M. Ajayan, "Vertical and in-plane heterostructures from WS<sub>2</sub>/MoS<sub>2</sub> monolayers," *Nature Materials*, vol. 13, pp. 1135-1142, 2014.
- [138] K. H. Liu, L. M. Zhang, T. Cao, C. H. Jin, D. A. Qiu, Q. Zhou, A. Zettl, P. D. Yang, S. G. Louie and F. Wang, "Evolution of interlayer coupling in twisted molybdenum disulfide bilayers," *Nature Communications*, vol. 5, 2014.
- [139] K. Kosmider and J. Fernandez-Rossier, "Electronic properties of the MoS<sub>2</sub>-WS<sub>2</sub> heterojunction," *Phys. Rev. B*, vol. 87, 2013.
- [140] J. G. He, K. Hummer and C. Franchini, "Stacking effects on the electronic and optical properties of bilayer transition metal dichalcogenides MoS<sub>2</sub>, MoSe<sub>2</sub>, WS<sub>2</sub>, and WSe<sub>2</sub>," *Phys. Rev. B*, vol. 89, 2014.

- [141] S. Y. Gan, Y. F. Liang, C. D. Spataru and L. Yang, "Dynamical Excitonic Effects in Doped Two-Dimensional Semiconductors," *Nano Letters*, vol. 16, pp. 5568-5573, 2016.
- [142] J. Koo, S. Y. Gao, H. Lee and L. Yang, "Vertical dielectric screening of few-layer van der Waals semiconductors," *Nanoscale*, vol. 9, pp. 14540-14547, 2017.
- [143] R. Soklaski, Y. F. Liang and L. Yang, "Temperature effect on optical spectra of monolayer molybdenum disulfide," *Applied Physics Letters*, vol. 104, 2014.
- [144] J. S. Ross, P. Rivera, J. Schaibley, E. Lee-Wong, H. Y. Yu, T. Taniguchi, K. Watanabe, J. Q. Yan, D. Mandrus, D. Cobden, W. Yao and X. D. Xu, "Interlayer Exciton Optoelectronics in a 2D Heterostructure p-n Junction," *Nano Letters*, vol. 17, pp. 638-643, 2017.
- [145] D. Xiao, G. B. Liu, W. X. Feng, X. D. Xu and W. Yao, "Coupled Spin and Valley Physics in Monolayers of MoS<sub>2</sub> and Other Group-VI Dichalcogenides," *Phys. Rev. Lett.*, vol. 108, 2012.
- [146] C. D. Spataru, S. Ismail-Beigi, R. B. Capaz and S. G. Louie, "Theory and ab initio calculation of radiative lifetime of excitons in semiconducting carbon nanotubes," *Phys. Rev. Lett.*, vol. 95, 2005.
- [147] P. Rivera, K. L. Seyler, H. Yu, J. R. Schaibley, J. Yan, D. G. Mandrus, W. Yao and X. Xu, "Valley-polarized exciton dynamics in a 2D semiconductor heterostructure," *Science*, vol. 351, pp. 688-691, 2016.
- [148] Z. F. Wang, Y. H. Chiu, K. Honz, K. F. Mak and J. Shan, "Electrical Tuning of Interlayer Exciton Gases in WSe<sub>2</sub> Bilayers," *Nano Letters*, vol. 18, pp. 137-143, 2018.
- [149] E. V. Calman, M. M. Fogler, L. V. Butov, S. Hu, A. Mishchenko and A. K. Geim, "Indirect excitons in van der Waals heterostructures at room temperature," *Nature Communications*, vol. 9, 2018.
- [150] A. H. Castro Neto, F. Guinea, N. M. R. Peres, K. S. Novoselov and A. K. Geim, "The electronic properties of graphene," *Rev. Mod. Phys.*, vol. 81, no. 1, pp. 109-162, 1 2009.
- [151] V. Meunier, A. G. S. Filho, E. B. Barros and M. S. Dresselhaus, "Physical properties of low-dimensional sp<sup>2</sup>-based carbon nanostructures," *Rev. Mod. Phys.*, vol. 88, p. 025005, 5 2016.

- [152] P. Recher and B. Trauzettel, "Quantum dots and spin qubits in graphene," *Nanotechnology*, vol. 21, p. 302001, 2010.
- [153] O. Gröning, S. Wang, X. Yao, C. A. Pignedoli, G. Borin Barin, C. Daniels, A. Cupo, V. Meunier, X. Feng, A. Narita, K. Müllen, P. Ruffieux and R. Fasel, "Engineering of robust topological quantum phases in graphene nanoribbons," *Nature*, vol. 560, pp. 209-213, 8 2018.
- [154] O. V. Yazyev, "Emergence of magnetism in graphene materials and nanostructures," *Reports on Progress in Physics*, vol. 73, p. 056501, 2010.
- [155] Y.-W. Son, M. L. Cohen and S. G. Louie, "Half-metallic graphene nanoribbons," *Nature*, vol. 444, p. 347, 11 2006.
- [156] M. Fujita, K. Wakabayashi, K. Nakada and K. Kusakabe, "Peculiar Localized State at Zigzag Graphite Edge:," *Journal of the Physical Society of Japan*, vol. 65, pp. 1920-1923, 1996.
- [157] K. Nakada, M. Fujita, G. Dresselhaus and M. S. Dresselhaus, "Edge state in graphene ribbons: Nanometer size effect and edge shape dependence," *Phys. Rev. B*, vol. 54, pp. 17954-17961, 12 1996.
- [158] D.-e. Jiang, B. G. Sumpter and S. Dai, "Unique chemical reactivity of a graphene nanoribbon's zigzag edge," *The Journal of Chemical Physics*, vol. 126, p. 134701, 6 2007.
- [159] J. Kunstmann, C. Özdoğan, A. Quandt and H. Fehske, "Stability of edge states and edge magnetism in graphene nanoribbons," *Phys. Rev. B*, vol. 83, p. 045414, 1 2011.
- [160] P. Koskinen, S. Malola and H. Häkkinen, "Self-Passivating Edge Reconstructions of Graphene," *Phys. Rev. Lett.*, vol. 101, p. 115502, 9 2008.
- [161] S. Okada, "Energetics of nanoscale graphene ribbons: Edge geometries and electronic structures," *Phys. Rev. B*, vol. 77, p. 041408, 1 2008.
- [162] B. Huang, M. Liu, N. Su, J. Wu, W. Duan, B.-l. Gu and F. Liu, "Quantum Manifestations of Graphene Edge Stress and Edge Instability: A First-Principles Study," *Phys. Rev. Lett.*, vol. 102, p. 166404, 4 2009.

- [163] T. Wassmann, A. P. Seitsonen, A. M. Saitta, M. Lazzeri and F. Mauri, "Structure, Stability, Edge States, and Aromaticity of Graphene Ribbons," *Phys. Rev. Lett.*, vol. 101, no. 9, p. 096402, 8 2008.
- [164] Y. Li, Z. Zhou, C. R. Cabrera and Z. Chen, "Preserving the Edge Magnetism of Zigzag Graphene Nanoribbons by Ethylene Termination: Insight by Clar's Rule," *Scientific Reports*, vol. 3, p. 2030, 6 2013.
- [165] M. Slota, A. Keerthi, W. K. Myers, E. Tretyakov, M. Baumgarten, A. Ardavan, H. Sadeghi, C. J. Lambert, A. Narita, K. Müllen and L. Bogani, "Magnetic edge states and coherent manipulation of graphene nanoribbons," *Nature*, vol. 557, pp. 691-695, 5 2018.
- [166] V. L. J. Joly, M. Kiguchi, S.-J. Hao, K. Takai, T. Enoki, R. Sumii, K. Amemiya, H. Muramatsu, T. Hayashi, Y. A. Kim, M. Endo, J. Campos-Delgado, F. López-Urías, A. Botello-Méndez, H. Terrones, M. Terrones and M. S. Dresselhaus, "Observation of magnetic edge state in graphene nanoribbons," *Phys. Rev. B*, vol. 81, p. 245428, 6 2010.
- [167] G. Z. Magda, X. Jin, I. Hagymási, P. Vancsó, Z. Osváth, P. Nemes-Incze, C. Hwang, L. P. Biró and L. Tapasztó, "Room-temperature magnetic order on zigzag edges of narrow graphene nanoribbons," *Nature*, vol. 514, p. 608, 10 2014.
- [168] T. Cao, Z. Li and S. G. Louie, "Tunable Magnetism and Half-Metallicity in Hole-Doped Monolayer GaSe," *Phys. Rev. Lett.*, vol. 114, p. 236602, 6 2015.
- [169] L. Seixas, A. S. Rodin, A. Carvalho and A. H. C. Neto, "Multiferroic Two-Dimensional Materials," *Phys. Rev. Lett.*, vol. 116, p. 206803, 5 2016.
- [170] N. Miao, B. Xu, N. C. Bristowe, J. Zhou and Z. Sun, "Tunable Magnetism and Extraordinary Sunlight Absorbance in Indium Triphosphide Monolayer," *J. Am. Chem. Soc.*, vol. 139, pp. 11125-11131, 8 2017.
- [171] J. Jung and A. H. MacDonald, "Carrier density and magnetism in graphene zigzag nanoribbons," *Phys. Rev. B*, vol. 79, p. 235433, 6 2009.
- [172] G. Kresse and D. Joubert, "From ultrasoft pseudopotentials to the projector augmented-wave method," *Phys. Rev. B*, vol. 59, pp. 1758-1775, 1 1999.
- [173] O. V. Yazyev and M. I. Katsnelson, "Magnetic Correlations at Graphene Edges: Basis for Novel Spintronics Devices," *Phys. Rev. Lett.*, vol. 100, p. 047209, 1 2008.
- [174] R. Denk, M. Hohage, P. Zeppenfeld, J. Cai, C. A. Pignedoli, H. Söde, R. Fasel, X. Feng, K. Müllen, S. Wang, D. Prezzi, A. Ferretti, A. Ruini, E. Molinari and P. Ruffieux,

- "Exciton-dominated optical response of ultra-narrow graphene nanoribbons," *Nature Communications*, vol. 5, p. 4253, 7 2014.
- [175] A. Kimouche, M. M. Ervasti, R. Drost, S. Halonen, A. Harju, P. M. Joensuu, J. Sainio and P. Liljeroth, "Ultra-narrow metallic armchair graphene nanoribbons," *Nature Communications*, vol. 6, p. 10177, 12 2015.
- [176] D. K. Efetov and P. Kim, "Controlling Electron-Phonon Interactions in Graphene at Ultrahigh Carrier Densities," *Phys. Rev. Lett.*, vol. 105, p. 256805, 12 2010.
- [177] J. Ye, M. F. Craciun, M. Koshino, S. Russo, S. Inoue, H. Yuan, H. Shimotani, A. F. Morpurgo and Y. Iwasa, "Accessing the transport properties of graphene and its multilayers at high carrier density," *Proc Natl Acad Sci USA*, vol. 108, p. 13002, 8 2011.
- [178] F. Banhart, J. Kotakoski and A. V. Krasheninnikov, "Structural Defects in Graphene," *ACS Nano*, vol. 5, pp. 26-41, 1 2011.
- [179] E. C. Stoner, "Collective electron ferromagnetism," *Proc R Soc Lond A Math Phys Sci*, vol. 165, p. 372, 4 1938.
- [180] J. F. Janak, "Uniform susceptibilities of metallic elements," *Phys. Rev. B*, vol. 16, pp. 255-262, 7 1977.
- [181] C. M. Teodorescu and G. A. Lungu, "Band ferromagnetism in systems of variable dimensionality," *Journal of Optoelectronics and Advanced Materials*, vol. 10, pp. 3058-3068, 2008.
- [182] Y.-W. Son, M. L. Cohen and S. G. Louie, "Energy Gaps in Graphene Nanoribbons," *Phys. Rev. Lett.*, vol. 97, p. 216803, 11 2006.
- [183] L. Yang, C.-H. Park, Y.-W. Son, M. L. Cohen and S. G. Louie, "Quasiparticle Energies and Band Gaps in Graphene Nanoribbons," *Phys. Rev. Lett.*, vol. 99, p. 186801, 11 2007.
- [184] H. Raza and E. C. Kan, "Armchair graphene nanoribbons: Electronic structure and electric-field modulation," *Phys. Rev. B*, vol. 77, p. 245434, 6 2008.
- [185] L. Brey and H. A. Fertig, "Electronic states of graphene nanoribbons studied with the Dirac equation," *Phys. Rev. B*, vol. 73, p. 235411, 6 2006.
- [186] J. Kübler, *Theory of itinerant electron magnetism*, vol. 106, Oxford University Press, 2017.

- [187] H. Thomann, L. K. Dalton, M. Grabowski and T. C. Clarke, "Direct observation of Coulomb correlation effects in polyacetylene," *Phys. Rev. B*, vol. 31, pp. 3141-3143, 3 1985.
- [188] L. Pisani, J. A. Chan, B. Montanari and N. M. Harrison, "Electronic structure and magnetic properties of graphitic ribbons," *Phys. Rev. B*, vol. 75, p. 064418, 2 2007.
- [189] A. Coker, T. Lee and T. P. Das, "Investigation of the electronic properties of tellurium---energy-band structure," *Phys. Rev. B*, vol. 22, pp. 2968-2975, 9 1980.
- [190] Y. Du, G. Qiu, Y. Wang, M. Si, X. Xu, W. Wu and P. D. Ye, "One-Dimensional van der Waals Material Tellurium: Raman Spectroscopy under Strain and Magneto-Transport," *Nano Lett.*, vol. 17, pp. 3965-3973, 6 2017.
- [191] Y. Wang, G. Qiu, R. Wang, S. Huang, Q. Wang, Y. Liu, Y. Du, W. A. Goddard, M. J. Kim, X. Xu, P. D. Ye and W. Wu, "Field-effect transistors made from solution-grown two-dimensional tellurene," *Nature Electronics*, vol. 1, pp. 228-236, 4 2018.
- [192] H. O. H. Churchill, G. J. Salamo, S.-Q. Yu, T. Hironaka, X. Hu, J. Stacy and I. Shih, "Toward Single Atom Chains with Exfoliated Tellurium," *Nanoscale Research Letters*, vol. 12, p. 488, 8 2017.
- [193] Z. Zhu, X. Cai, S. Yi, J. Chen, Y. Dai, C. Niu, Z. Guo, M. Xie, F. Liu, J.-H. Cho, Y. Jia and Z. Zhang, "Multivalency-Driven Formation of Te-Based Monolayer Materials: A Combined First-Principles and Experimental study," *Phys. Rev. Lett.*, vol. 119, p. 106101, 9 2017.
- [194] M. Mo, J. Zeng, X. Liu, W. Yu, S. Zhang and Y. Qian, "Controlled Hydrothermal Synthesis of Thin Single-Crystal Tellurium Nanobelts and Nanotubes," *Adv. Mater.*, vol. 14, pp. 1658-1662, 11 2018.
- [195] B. Mayers and Y. Xia, "One-dimensional nanostructures of trigonal tellurium with various morphologies can be synthesized using a solution-phase approach," *J. Mater. Chem.*, vol. 12, pp. 1875-1881, 2002.
- [196] Y.-J. Zhu, W.-W. Wang, R.-J. Qi and X.-L. Hu, "Microwave-Assisted Synthesis of Single-Crystalline Tellurium Nanorods and Nanowires in Ionic Liquids," *Angewandte Chemie*, vol. 116, pp. 1434-1438, 11 2018.

- [197] C. J. Hawley, B. R. Beatty, G. Chen and J. E. Spanier, "Shape-Controlled Vapor-Transport Growth of Tellurium Nanowires," *Crystal Growth & Design*, vol. 12, pp. 2789-2793, 6 2012.
- [198] J. C. Slater and G. F. Koster, "Simplified LCAO Method for the Periodic Potential Problem," *Phys. Rev.*, vol. 94, pp. 1498-1524, 6 1954.
- [199] S. D. Sarma, M. Freedman and C. Nayak, "Majorana zero modes and topological quantum computation," *Npj Quantum Information*, vol. 1, p. 15001, 10 2015.
- [200] V. Mourik, K. Zuo, S. M. Frolov, S. R. Plissard, E. P. A. M. Bakkers and L. P. Kouwenhoven, "Signatures of Majorana Fermions in Hybrid Superconductor-Semiconductor Nanowire Devices," *Science*, vol. 336, pp. 1003-1007, 2012.
- [201] B. Göhler, V. Hamelbeck, T. Z. Markus, M. Kettner, G. F. Hanne, Z. Vager, R. Naaman and H. Zacharias, "Spin Selectivity in Electron Transmission Through Self-Assembled Monolayers of Double-Stranded DNA," *Science*, vol. 331, p. 894, 2 2011.
- [202] R. Naaman and D. H. Waldeck, "Chiral-Induced Spin Selectivity Effect," *J. Phys. Chem. Lett.*, vol. 3, pp. 2178-2187, 8 2012.
- [203] A.-M. Guo and Q.-f. Sun, "Spin-Selective Transport of Electrons in DNA Double Helix," *Phys. Rev. Lett.*, vol. 108, p. 218102, 5 2012.